

**DEVELOPMENT OF A REDUCED COMPUTATIONAL MODEL TO  
REPLICATE INLET DISTORTION IN AN APU-STYLE INLET OF A  
CENTRIFUGAL COMPRESSOR**

by

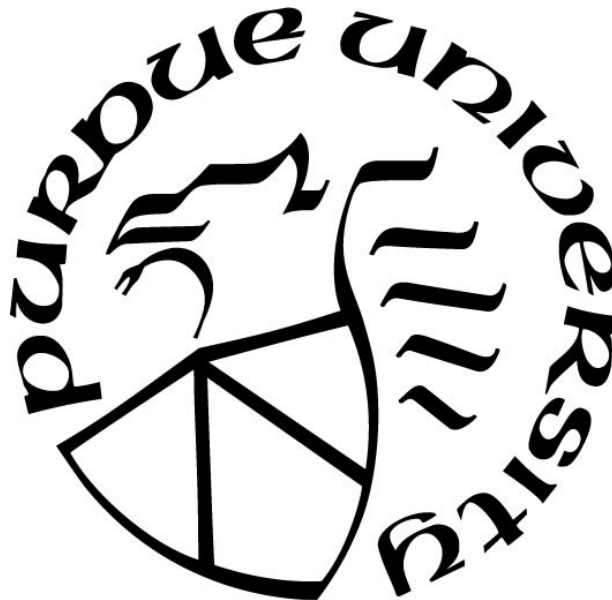
**Evan H. Bond**

**A Thesis**

*Submitted to the Faculty of Purdue University*

*In Partial Fulfillment of the Requirements for the degree of*

**Master of Science in Aeronautics and Astronautics**



School of Aeronautics and Astronautics

West Lafayette, Indiana

May 2022

**THE PURDUE UNIVERSITY GRADUATE SCHOOL**  
**STATEMENT OF COMMITTEE APPROVAL**

**Dr. Nicole Key, Chair**

School of Mechanical Engineering

**Dr. Guillermo Paniagua**

School of Mechanical Engineering

**Dr. Carson Slabaugh**

School of Aeronautics and Astronautics

**Approved by:**

Dr. Gregory Blaisdell

*“Keeping the dream alive 101: Never let anyone tell you that it’s not coming home or that the times are too fast for you” - Campbell Bond*

## ACKNOWLEDGMENTS

I would like to thank Dr. Nicole Key for her guidance and support through the two years of this degree and the writing of this thesis. Your technical advice, openness, and understanding through challenging times during the pandemic have been very much appreciated. I also want to thank Dr. Guillermo Paniagua and Dr. Carson Slabaugh for serving on my committee.

Without sponsorship from Honeywell Aerospace this research would not have been possible. Furthermore, the engineering knowledge and facility support from Darrell James, Andrew Loudonbeck, Glen Nawrocki, and Bruce Bouldin has been invaluable to this effort, thank you. To my fellow graduate research assistants that been a part of the Honeywell project during my time here: Trey Harrison, William Brown, Matthew Fuehne, and Joseph Brown, thank you for your support and friendship throughout my time at Purdue. Fangyuan Lou and Matthew Meier have been a great help in developing my understanding of centrifugal compressors, thank you for the time you invested in my learning. I also want to acknowledge and thank Yuning Dai and Douglas Matthews for their help with the development of my CFD models and their guidance through each step of the way. Also, a big thank you to Mark Shapochka for being my officemate while I worked on this thesis and for being a never-ending source of humor.

To my parents, Craig and Amanda, we have been through a lot in the past two years, and without your love and guidance I would not be in the place I am today. Thank you for your unrelenting support – no matter how many oceans we are separated by. Finally, I cannot thank my wife Mindy enough for moving out to Indiana to pursue this opportunity with me and for loving me through everything the past two years has thrown our way. My name may be on this thesis, but this is something we have achieved together, equally.



# TABLE OF CONTENTS

LIST OF TABLES .....	8
LIST OF FIGURES .....	9
NOMENCLATURE .....	13
ABSTRACT.....	17
1. INTRODUCTION .....	19
1.1 Motivation.....	19
1.2 Inlet Distortion.....	20
1.2.1 Pressure Distortion.....	20
1.2.2 Swirl Distortion .....	21
1.3 APU Inlet Flow Physics.....	22
1.3.1 Radial-to-Axial Inlet Flows .....	24
1.3.2 Rectangular Elbow Duct Flows .....	26
1.3.3 Circular-to-Rectangular Duct Flows.....	28
1.4 Generation of Inlet Distortion Patterns .....	30
1.5 Inlet Distortion Effects on Centrifugal Compressors.....	31
1.5.1 Performance .....	32
Effect of Pressure Distortion on Compressor Performance .....	32
Effects of Swirl Distortion on Compressor Performance.....	33
1.5.2 Stability.....	35
1.5.3 Forced Response.....	37
1.6 Research Objectives.....	40
2. EXPERIMENTAL AND COMPUTATIONAL MODELS .....	41
2.1 Honeywell SSCC at Purdue .....	41
2.1.1 SSCC Facility and Operation.....	41
2.1.2 APU Inlet Configurations .....	45
2.1.3 Inlet Instrumentation.....	47
2.2 Development of Plenum Computational Model .....	49
2.2.1 Plenum Model Domains and Interfaces.....	49
2.2.2 Plenum Model Boundary Conditions and Discretization .....	50

2.2.3	Plenum Model Mesh.....	52
2.2.4	Plenum Model Grid Convergence Study .....	53
2.2.5	Veracity of Plenum Flow Structure .....	56
2.3	Development of Full-Inlet Computational Model .....	59
2.3.1	Full-Inlet Model Domains and Interfaces.....	59
2.3.2	Full-Inlet Model Boundary Conditions and Discretization .....	60
2.3.3	Full-Inlet Model Mesh.....	61
2.3.4	Full-Inlet Model Grid Convergence Study .....	63
2.3.5	Veracity of Circle-to-Square Flow Structure.....	66
2.3.6	Veracity of Elbow Flow Structure.....	67
2.4	Computational Replication of Three-Hole Probe Traverse .....	70
3.	DATA PROCESSING.....	74
3.1	Experiment Three-Hole Probe Rotatable Rake Data Processing.....	74
3.2	Distortion Descriptors.....	77
3.2.1	Pressure Distortion Descriptors .....	78
3.2.2	Swirl Distortion Descriptors .....	80
3.3	Computational Model Data.....	82
3.3.1	Extraction and Processing of CFD Data at AIP.....	82
3.3.2	Computational Three-Hole Probe Model Data Extraction and Processing .....	85
4.	COMPUTATIONAL MODEL RESULTS AND COMPARISON WITH EXPERIMENT.....	87
4.1	Selected Operating Points for Analysis .....	87
4.2	Effects of Individual Inlet Components on Annulus Flow Field.....	88
4.2.1	Struts.....	88
4.2.2	Inlet Rakes .....	90
4.2.3	Shroud Instrumentation Notches .....	91
4.2.4	Sandwich Pack Rakes .....	93
4.2.5	Cumulative Component Effects on Annulus Flow .....	94
4.3	Three-Hole Probe Effectiveness .....	96
4.3.1	Radial Flow Angle Effects.....	96
4.3.2	Shroud-Side End Wall Effects.....	97
4.3.3	Hub-Side End Wall Effects .....	100

4.3.4	Three-Hole Probe Model Results .....	101
4.4	Baffle Cases .....	105
4.4.1	Radial Flow Angle Considerations.....	105
4.4.2	Circumferential Total Pressure Distortion.....	106
4.4.3	Radial Total Pressure Distortion.....	109
4.4.4	Swirl Characteristics .....	111
4.5	Blocker Plate Cases.....	114
4.5.1	Sandwich Pack Flow Conditions .....	114
4.5.2	Radial Flow Angle Considerations.....	117
4.5.3	Circumferential Total Pressure Distortion.....	119
4.5.4	Radial Total Pressure Distortion.....	122
4.5.5	Swirl Characteristics .....	123
5.	CONCLUSIONS .....	129
5.1	Summary of Model Performance Compared to Experiment .....	129
5.2	Efficacy of Plenum Model .....	131
5.3	Future Research Recommendations.....	132
	REFERENCES .....	136

## LIST OF TABLES

Table 2.1. Plenum model mesh statistics .....	53
Table 2.2. Plenum Model GCS Metrics.....	55
Table 2.3. Full-Inlet model mesh statistics .....	64
Table 2.4. Full-Inlet GCS metrics.....	65

## LIST OF FIGURES

Figure 1.1. Graphic representation of total distortion definitions.....	21
Figure 1.2. Graphic representation of swirl pattern definitions .....	22
Figure 1.3. Airbus A300 APU air intake system from Lotter and Jörg (1982) .....	23
Figure 1.4. Diagram of typical flow structure of radial-to-axial inlet (oriented FLA) .....	24
Figure 1.5. Graphic of twin-swirl development through a rectangular elbow duct due to pressure gradients.....	27
Figure 1.6. Illustration of flow momentum structure of circular to rectangular ducts.....	29
Figure 1.7. Typical APU plenum distortion generator geometry .....	31
Figure 1.8. Velocity triangles at the inducer including effect of pressure distortion.....	32
Figure 1.9. Velocity triangles at the inducer including effect of swirl .....	34
Figure 1.10. Speedline representation of stability limit degradation under inlet distortion .....	36
Figure 1.11. Example of a 5 MPR total pressure profile in an inlet annulus.....	38
Figure 1.12. Example Campbell diagram for a compressor with strong 5EO responses .....	39
Figure 2.1. SSCC facility with APU inlet installed .....	42
Figure 2.2. SSCC APU calibrated bellmouth geometry and instrumentation .....	43
Figure 2.3. SSCC APU inlet components.....	45
Figure 2.4. SSCC APU inlet baffle configurations.....	46
Figure 2.5. SSCC APU inlet blocker plate configurations viewed from above .....	46
Figure 2.6. SSCC APU inlet plenum and annulus instrumentation.....	47
Figure 2.7. SSCC rotatable rake instrumentation and survey traverse .....	48
Figure 2.8. Plenum model domains and interfaces .....	50
Figure 2.9. Plenum model mesh, 0° baffle configuration ALF .....	52
Figure 2.10. Plenum model grid convergence study plots of TPR and $\eta$ .....	54
Figure 2.11 Plenum model grid convergence cases normalized total pressure values at AIP .....	56
Figure 2.12 Plenum model inlet rake normalized total pressure data compared with experiment	57
Figure 2.13 Plenum model case 2 simulation Mach number and flow distribution in the mid plane of the plenum, FLA orientation .....	58

Figure 2.14 Plenum model case 2 simulation Mach number and 2D streamlines at the AIP, FLA orientation .....	59
Figure 2.15. Full-Inlet model domains and interfaces .....	60
Figure 2.16. Full-Inlet model opening boundary condition with streamlines colored by axial position.....	61
Figure 2.17. Spreader-elbow domain mesh using H-O-H grid topology FLA .....	62
Figure 2.18. Bellmouth and inlet extension domain mesh using O-grid topology .....	63
Figure 2.19. Full-Inlet model grid convergence study plots.....	64
Figure 2.20. Full-Inlet model grid convergence cases normalized total pressure values at AIP ..	66
Figure 2.21. Full-Inlet model case 2 transition duct axial velocity profile.....	67
Figure 2.22. Sandwich pack total pressure from experiment and full-inlet model case 2, viewed top down.....	68
Figure 2.23. LDV planes replicated in Full-Inlet model for comparison .....	68
Figure 2.24. Comparison of Full-Inlet CFD elbow flow velocity and streamlines with LDV data from Lou et al. (2015).....	69
Figure 2.25. Three-hole probe computation models' rotatable rake traverse location, FLA orientation .....	71
Figure 2.26. Three-hole probe rendering and mesh.....	73
Figure 3.1. Visual of three-hole probe .....	74
Figure 3.2. Example calibration for a three-hole probe used in experiment.....	76
Figure 3.3. Graphic of terms needed to calculate total pressure distortion descriptors .....	78
Figure 3.4. Graphic of terms needed to calculate swirl distortion descriptors .....	81
Figure 3.5. CFX Post rotatable rake polyline at AIP and unit vector directions .....	83
Figure 3.6. AIP coordinate system from CFX Post and r- $\theta$ velocities.....	84
Figure 3.7. Velocity triangles used to calculate swirl and radial flow angle .....	85
Figure 3.8. Averaged calibrations used for CFD three-hole probe data analysis .....	86
Figure 4.1. Operating points for experiment surveys and CFD simulations .....	87
Figure 4.2. Strut wakes visualized by streamlines colored by total pressure for 0° and 70° baffles, and 50% left blockage plate configurations viewed FLA.....	89
Figure 4.3. Inlet rake wakes visualized by streamlines colored by total pressure for 0° and 70° baffles, and 50% left blockage plate configurations viewed FLA.....	90
Figure 4.4. Rendering of shroud notches within plenum viewed top-down.....	92

Figure 4.5. Shroud notch wakes visualized by streamlines colored by total pressure for 0° and 70° baffles, and 50% left blockage plate configurations viewed FLA.....	92
Figure 4.6. Sandwich pack rake wakes visualized by streamlines colored by total pressure for 0° and 70° baffles, and 50% left blockage plate configurations viewed FLA .....	94
Figure 4.7. Experiment and computational model AIP total pressure deficit zones caused by wakes of inlet components.....	95
Figure 4.8. Nominal configuration radial flow angles from CFD simulations for both models at AIP .....	97
Figure 4.9. $C_{p,static}$ values for a multi-hole probe fixed to a wall with varying yaw angles (Treaster and Yocum, 1978).....	98
Figure 4.10. Nominal SSCC Mach data compared to Pazzi and Michelassi (2001) and Michelassi and Giachi (1997) .....	100
Figure 4.11. $C_{p,static}$ values for a multi-hole probe suspended above a wall with varying yaw angles (Treaster and Yocum, 1978) .....	101
Figure 4.12. Plenum model, plenum model with three-hole probes, and experiment contours in nominal configuration.....	102
Figure 4.13. Full-Inlet model, Full-Inlet model with three-hole probes, and experiment contours in nominal configuration.....	104
Figure 4.14. Radial flow angles for positive baffle configurations at 100% $N_c$ from CFD simulations of both models .....	106
Figure 4.15. Circumferential pressure distortion intensities for all off-design baffles.....	108
Figure 4.16. Total pressure variation contours from Kulite data for $\pm 70^\circ$ baffles at 100% $N_c$ in choke.....	109
Figure 4.17. Radial pressure distortion intensities for all off-design baffles.....	111
Figure 4.18. Swirl intensity for all off-design baffles.....	112
Figure 4.19. Swirl directivity for all off-design baffles .....	113
Figure 4.20. Sandwich pack total pressures for 25% blockage plate configurations at 100% $N_c$ .....	115
Figure 4.21. Sandwich pack total pressures for 50% blockage plate configurations at 100% $N_c$ .....	117
Figure 4.22. 0%, 25% and 50% left blockage plate configuration flow angles.....	118
Figure 4.23. Circumferential pressure distortion intensities for all blocker plate configurations .....	120
Figure 4.24. Total pressure variation contours from Kulite data for left blockage plates at 100% $N_c$ in choke.....	121

Figure 4.25. Radial pressure distortion intensities for all blocker plate configurations .....	122
Figure 4.26. Swirl intensity for all blocker plate configurations .....	124
Figure 4.27. Left blockage plate speed-lines colored by normalized shroud temperature upstream of inducer .....	125
Figure 4.28. Swirl directivity for all blocker plate configurations .....	126
Figure 4.29. Circumferential swirl contours for both CFD models and experiment for 25% left blockage configuration at the highest and lowest mass flow rates .....	128
Figure 5.1. Contours of total pressure at the AIP and at the inducer for four traverse locations from plenum model data in the nominal configuration at 100% $N_c$ .....	134
Figure 5.2. Contours of circumferential swirl at the AIP and at the inducer for four traverse locations from plenum model data in the nominal configuration at 100% $N_c$ .....	135



## NOMENCLATURE

<b><u>Acronyms</u></b>	<b><u>Definition</u></b>
2D	Two Dimensional
3D	Three Dimensional
AIP	Aerodynamic Interface Plane
ALF	Aft Looking Forward
APU	Auxiliary Power Unit
BDC	Bottom Dead Center
BSL	Baseline
CFD	Computational Fluid Dynamics
EO	Engine Order
FLA	Forward Looking Aft
FOD	Foreign Object Debris
GGI	General Grid Interface
LDV	Laser Doppler Velocimetry
MPR	Multiple Per Revolution
RPM	Revolutions Per Minute
SPIP	Sandwich-Pack Interface Plane
SSCC	Single Stage Centrifugal Compressor
SST	Shear Stress Transport
TDC	Top Dead Center
THP	Three-Hole Probe
TPR	Total Pressure Ratio
VFD	Variable Frequency Drive

<b><u>Symbols</u></b>	<b><u>Definition</u></b>
$a$	Speed of sound
$C_{null}$	Three-hole probe nulling coefficient
$C_{p,static}$	Static pressure coefficient

$C_{PSY}$	Static pressure coefficient corrected for yaw
$C_{RPY}$	Ram pressure coefficient corrected for yaw
$C_{YPD}$	Coefficient of yaw due to pressure differential
$D$	Diameter
$d$	Probe diameters
$d\theta$	Differential circumferential angle
$e$	Relative error
$GCI$	Grid convergence index
$\dot{m}$	Mass flow rate
$M$	Mach number
$N$	Number of rake elements
$N_c$	Corrected speed
$P$	Pressure
$PAV$	Circumferential ring average total pressure
$PAVLOW$	Average total pressure in an extent
$PFAV$	Area weighted face average total pressure
$PI$	Pressure intensity
$SD$	Swirl directivity
$SM$	Stability margin
$SI$	Swirl intensity
$SP$	Swirl pairs
$SS$	Sector swirl
$U$	Rotational velocity
$V$	Absolute velocity
$W$	Relative velocity
$X$	X location
$Y$	Y location
$Z$	Z location
$z$	Blade count

<b><u>Greek</u></b>	<b><u>Definition</u></b>
$\alpha$	Swirl angle
$\gamma$	Ratio of specific heats
$\zeta$	Radial flow angle
$\eta$	Isentropic inlet efficiency
$\theta$	Circumferential angle or circumferential extent
$\omega$	Angular velocity

<b><u>Subscripts</u></b>	<b><u>Definition</u></b>
0	Stagnation condition
1	Inlet entrance station
2	Aerodynamic interface plane station
<i>a</i>	Approximate
<i>c</i>	Corrected
<i>C</i>	Center
<i>circ</i>	Circumferential
<i>crit</i>	Critical
<i>D</i>	Distorted parameter
<i>ext</i>	Extrapolated
<i>i</i>	Circumferential ring number
<i>f</i>	Frequency
<i>k</i>	Extent occurrence number along a circumferential ring
<i>L</i>	Left
<i>mech</i>	Mechanical
<i>P</i>	Pressure distortion effect
<i>Q</i>	Total number of extents along a circumferential ring
<i>R</i>	Right
<i>rad</i>	Radial
<i>s</i>	Static

$S$	Swirl distortion effect
$\theta$	Tangential direction
$x$	X direction
$y$	Y direction
$z$	Z direction

<b><u>Superscripts</u></b>	<b><u>Definition</u></b>
+	Positive sector
–	Negative sector
21	From case two to case one
32	From case three to case two

## ABSTRACT

The purpose of this research was to determine what components of a complex centrifugal compression system inlet needed to be modelled to accurately predict the swirl and total pressure distortions at the compressor face. Two computational models were developed. A full-fidelity case where all the inlet geometry was modelled and a reduced model where a small portion of the inlet was considered. Both the numerical cases were compared with experimental data from a research compressor rig developed by Honeywell Aerospace. The test apparatus was designed with a modular inlet system to develop swirl distortion patterns. The modular inlet system utilized transposable baffles within the radial-to-axial section of the inlet and blockage plates of varying sizes and geometries at the inlet to this section.

Discerning the dominant inlet component that dictates distortion behavior at the compressor face would allow the reduced modelling of inlet components for compression systems and would allow coupling with more tortuous systems. Furthermore, it would reduce the design iteration and simulation time of the inlet systems. Several investigations utilizing a reduced model only considering a radial-to-axial inlet are available in literature, but no comprehensive justification has been presented as to the impact this has on the distortion behavior.

Experimental surveys of flow conditions just upstream of the inducer of the centrifugal compressor were conducted at several operating conditions. The highest and lowest mass flow rates of these operating points were simulated using ANSYS CFX 2020R1 for both the computational models. Multiple inlet configurations were simulated to test the robustness of the reduced model in comparison to the full fidelity. The numerical simulations highlighted shortcomings of the instrumentation used to characterize the experimental flow field at the inducer, particularly with respect to total pressure distortion. Furthermore, transient pressure data were measured in experiment and indicated unsteady fluctuations in the inlet that would not be captured by steady computational fluid dynamic simulations. These data matched locations of disagreement with swirl distortion behavior at high mass flow rates. This suggested that transient vortex movement occurred at the aerodynamic interface plane in certain configurations.

The total pressure distortion metrics between the two models were remarkably comparable. Furthermore, the simplified model accurately predicted the mixing losses associated with the blockage plates at the inlet to the radial-to-axial inlet using a simple inlet extension. Swirl

distortion was dictated by the radial-to-axial inlet. The reduced model data trends were comparable with experiment for both the baffle and blocker plate configurations. The swirl intensities for all configurations were comparable between the two models. The reduced model swirl directivity trends matched those of experiment. The most notable deviations between the full-fidelity model and the reduced model were observed with swirl directivity numerics.

# **1. INTRODUCTION**

## **1.1 Motivation**

With further development of unmanned aerial vehicles and ever more powerful helicopters, centrifugal compressors are being used in an increasing number of applications due to their compactness and resilience to distortion effects when compared to axial compression systems. Additional complications in designs of compact inlets to meet space requirements have led to air being fed to compression systems through tortuous routing. This ducting inherently develops complex secondary flow structures and total pressure non-uniformities due to the build-up of adverse pressure gradients. The external flow effects such as sidewash, downwash, aircraft angle-of-attack, etc. also further complicate the distortions that progress through the intricate airways. These distortions adversely impact compressor performance and stability, and if the engine is not specified correctly for a mission profile or installation that produces these distortion patterns, it may enter surge or have increased fuel consumption thereby reducing aircraft range. The stability of centrifugal compressors shows a markedly reduced sensitivity to these inlet non-uniformities when compared to axial compressors, as they achieve most of their pressure rise through the centrifugal effect. This allows the compression system to operate with reasonable performance in a stalled condition (Cousins et al., 1994). Consequently, they are more commonly employed in compression systems that experience drastic or unpredictable distortion.

Substantial research is being conducted to understand the development of distortion at the compressor face through these complex inlet systems using CFD during the design phase. However, the question of how much of the inlet needs to be modelled to correctly characterize the flow at the inducer of a centrifugal compression system remains. Understanding which inlet components have dominant effects on the flow field at the AIP is crucial to erode design iteration time and can permit efforts to be directed at reducing the largest inducers of distortion. Moreover, if one component dictates flow field behavior and all upstream components have a negligible impact on distortion, less consideration can be given to the upstream component design and will also allow the downstream design to be more adaptable to further applications. An understanding of these dominant components would also reduce model computation time and hardware

requirements as the mesh can be reduced to only include the components that command distortion behavior.

## **1.2 Inlet Distortion**

Inlet distortion is defined as any non-uniformity of a flow at the face of a compression system. It is quantified at an aerodynamic interface plane (AIP) located upstream of the compressor face. The AIP is the plane perpendicular to the axial inlet flow at the face of the compressor and contains instruments to resolve flow features. During operation, distortions can be encountered in numerous different circumstances, and the response of the compression system must be understood by engine designers to ensure satisfactory performance and stability as well as preventing severe aeromechanic excitation. To determine the type of distortion an engine will encounter, a mission profile is developed, and the engine behavior throughout the predicted modes of operation is estimated. The most common type of distortions experienced by centrifugal compressors that affect stability and performance are pressure and swirl distortions.

### **1.2.1 Pressure Distortion**

Pressure distortion, also interchangeably referred to as total pressure distortion or velocity distortion, is commonly encountered by centrifugal compression systems and was the primary topic of interest for gas turbine engines until the 2000s. Pressure distortion is the most widely investigated cause of gas turbine compression system instability because it is the largest contributor to pitot-like engine distortion losses. Centrifugal compressors for APU applications are not installed in this fashion, but they do experience similar effects of total pressure non-uniformities due to separation induced by inlet geometry. Areas of total pressure deficits compared to the average total pressure at the AIP is indicative of an area of pressure distortion.

Pressure distortions are broken into radial and circumferential phenomena. Circumferential pressure distortions are caused by asymmetric obstacles, such as struts or bends, or fuselage boundary layer ingestion upstream of the AIP (Cousins et al., 1994). Conversely, radial distortions are a result of axisymmetric flow disturbances and are separated into tip and hub phenomena as they have their own impact compressor performance and discrete causations. Hub distortions are typically generated by axisymmetric boundary layer ingestion or blockage at the center of the inlet,



and tip distortions are caused by flow devices such as orifice plates, or boundary layers developed in the compression system inlet (Ariga et al., 1983). Figure 1.1 is a basic representation of these distortion types, with grey representing the location of a total pressure deficit at the AIP.

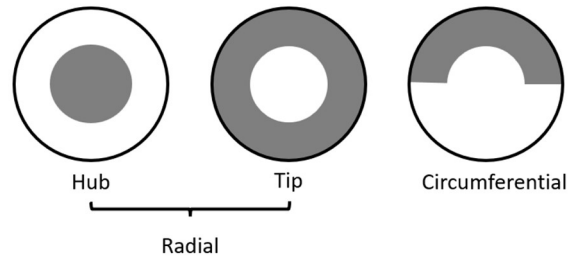


Figure 1.1. Graphic representation of total distortion definitions

### 1.2.2 Swirl Distortion

Swirl is the circumferential tangential motion of the secondary flow. If the tangential component of the secondary flow is in the same direction as the compressor rotation it is known as co-rotating swirl, or ‘co-swirl’. Co-swirl is assigned as a positive value because it increases the absolute flow angle of the fluid at the face of the compression system. Conversely, if the tangential flow velocity is opposite to the rotation of the compressor it is designated as counter rotating swirl, or ‘counter-swirl’ and is assigned a negative swirl value because the absolute flow angle is decreased. There are three main types of swirl structures: tightly wound vortices, bulk swirl, and paired swirl. Tightly wound vortices are often ingested into the engine from the ground or fuselage of an aircraft and are more common in axial systems with pitot installations (Sheoran and Bouldin, 2008). Therefore, centrifugal compressors installed in an APU style configuration mainly encounter bulk and paired swirl.

If all the circumferential flow at the AIP is rotating in one direction, this is known as bulk swirl, and if there is more than one direction of rotation this is known as paired swirl (Bouldin and Sheoran, 2002). If the paired swirl is equal and opposite in motion, it is designated as a twin swirl structure, but if one swirl region is larger than the other it is defined as offset swirl. Figure 1.2 is a summary of these typical swirl structures with their respective directions; the blue arrows represent the direction of compressor rotation and the black arrows the direction of circumferential vortex flow motion.

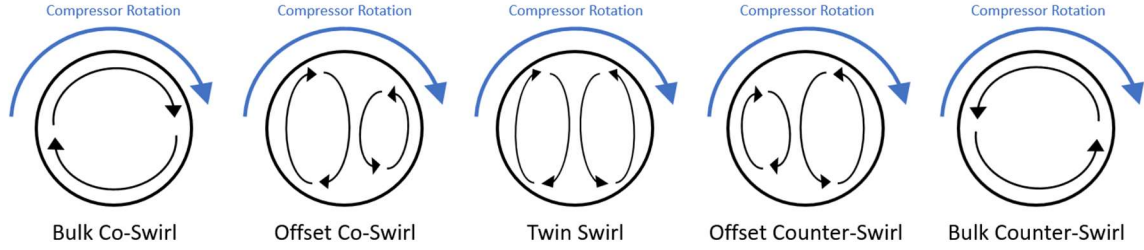


Figure 1.2. Graphic representation of swirl pattern definitions

Bulk swirl is often generated by inlet guide vanes, or an inlet scroll, and paired swirl is often developed in APU inlets because of adverse pressure gradients developed by flow turning within the ducting or due to the splitting of the flow in the radial-to-axial plenum (AIR5686, 2017). Ducting usually creates a twin swirl effect if the flow entering a turning duct is uniform and has equal boundary layers on all sides of the duct (AIR1419C, 2017). If the flow is not uniform at the duct inlet, offset swirl is developed. This is a result of the adverse pressure gradient through the bends causing high- and low-pressure regions to direct the flow, which induces a secondary structure. Offset swirl pairs are also present in APUs or helicopter engines due to sidewash and downwash at the inlet of the airway (AIR1419C, 2017).

### 1.3 APU Inlet Flow Physics

APU inlets are complex in nature and are predominantly located in the aircraft empennage. This location requires duct geometry to be tortuous and leads to complex packaging requirements for the engine. Furthermore, the ingestion of boundary layers from the fuselage, downwash, and crosswinds alters the flow structures that enter the inlet. These factors all negatively impact the performance of the inlet system. The performance of these inlets is characterized using inlet total pressure recovery (TPR) and efficiency ( $\eta$ ). Inlet TPR is defined using equation (1.1) and is a metric to quantify loss the area average loss of total pressure by the inlet system:

$$TPR = \frac{P_{02}}{P_{01}}. \quad (1.1)$$

To quantify the ability of an inlet to propagate flow without incurring losses due to entropy increases,  $\eta$  is used and is calculated using (1.2). This definition of inlet efficiency was introduced by Kim et al. (2001) and is an adaptation of nozzle effectiveness for use with inlet systems:

$$\eta = \frac{1 - T_2/T_{01}}{1 - (P_2/P_{01})^{\frac{\gamma-1}{\gamma}}}. \quad (1.2)$$

The equation quantifies the change of the inlet kinetic energy to the change in internal energy. For a perfect inlet, this should be a one-to-one relationship. However, for a real inlet, the internal energy is increased due to mixing losses in the inlet. Therefore, the  $T_2/T_{01}$  internal energy change term is larger than kinetic energy term  $(P_2/P_{01})^{\frac{\gamma-1}{\gamma}}$  that is the representative the isentropic change of the inlet flow internal energy.

Current industry consensus is that the inlet system is developed by a radial-to-axial flow plenum, a flow routing duct, and a diffusion or transition duct. An example of an installation in this manner is provided in Figure 1.3. For this effort, the flow routing duct that will be considered is a 90° rectangular elbow duct, and the transition duct is of a circular-to-square cross section.

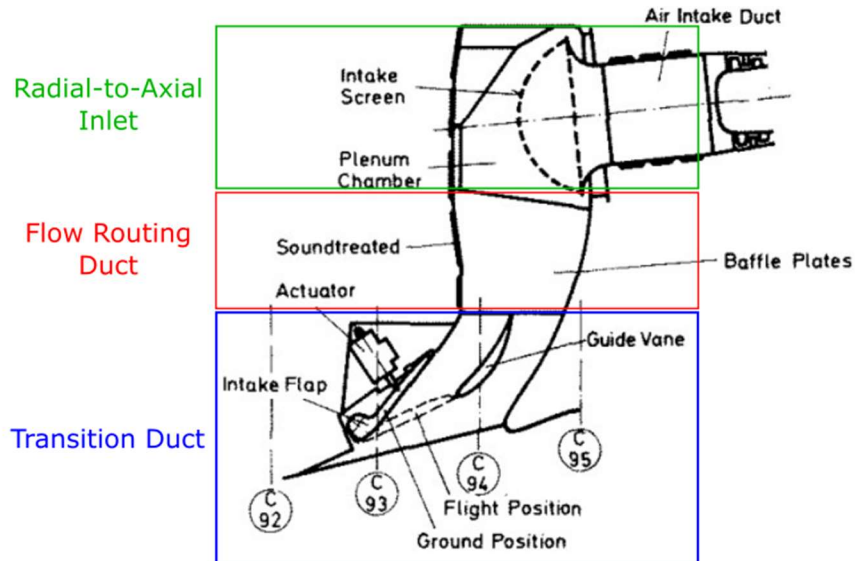


Figure 1.3. Airbus A300 APU air intake system from Lotter and Jörg (1982)

### 1.3.1 Radial-to-Axial Inlet Flows

For engines that are required to comply to strict packaging constraints, radial-to-axial inlets are often employed as they negate the necessity for the compression system to be oriented axially with the incoming flow source. These are a typical component of APU-style inlets and are referred to as an APU plenum. They are characterized by a rectangular inlet cross-section where radial flow enters, curved outer walls to diffuse and redistribute flow, and either an annular or circular cross section axial exit flow-path to the compressor. To prevent mixing losses at bottom dead center (BDC) of the plenum, a baffle is employed to generate a high-pressure zone to turn the flow toward the axial flow section without the added mixing that would occur with improper flow guidance. The utilization of a baffle at BDC also prevents the generation of a bulk swirl pattern that could occur if there is a significant tangential velocity component at the radial inlet plane (AIR 5686, 2017). The primary consequence of this baffle coupled with the increase in cross sectional area leads to the development of a high and low momentum region of flow, as shown in Figure 1.4.

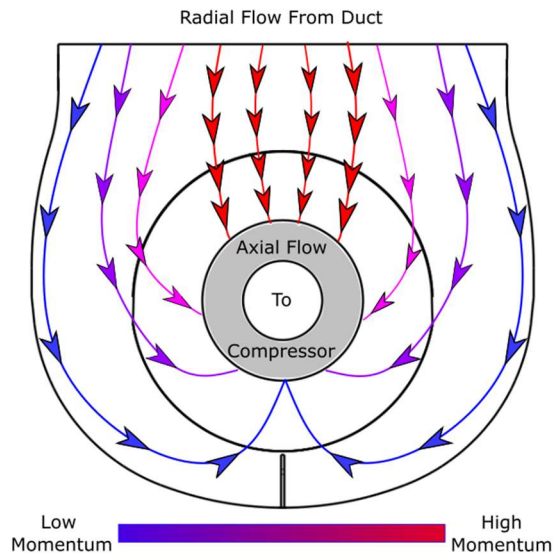


Figure 1.4. Diagram of typical flow structure of radial-to-axial inlet (oriented FLA)

This is the typical flow structure for a radial-to-axial inlet and has been widely documented (Koch et al., 2015; Michelassi and Giachi, 1997; Pazzi and Michelassi, 2001; Han et al., 2015). Koch et al. (1995) performed experiments on a radial compressor inlet with a plenum geometry with varying inlet ducting. They indicated that the total pressure loss through the plenum is a

function of the local Mach number, which is in line with what is expected from Fanno flow. Therefore, the higher momentum flow incurs more loss due to frictional and mixing effects being larger at higher Mach numbers. This creates a total pressure deficit at the top of the axial flow section. Relative to the top of the axial flow region, the lower momentum flow at the bottom has a higher total pressure and static pressure. This pressure differential is the causation of the twin-swirl and offset-swirl patterns typical of APU plenums. Koch et al. (1995) also posited that the radial-to-axial inlet mixes out most other upstream flow effects as the plenum-induced flow structures become dominant due to this induced pressure differential.

Lavan Kumar et al. (2013) noted similar flow development in their investigation of distortion development through an APU inlet plenum using experiment and CFD data. The authors indicated that twin-swirl is induced if the radial flow entering the plenum is symmetric as the higher-pressure fluid at the bottom of the annulus rises to the top and is redistributed along the outer walls of the annulus. If the radial flow profile is asymmetric, offset-swirl would be formed with the larger recirculation zone being located on the side of higher inlet momentum. They also demonstrated that an oversized radial-to-axial inlet increases loss in the lower momentum portion of the plenum. The presence of recirculation zones on either side of the baffle, known as ‘dead zones’, are indicative of an oversized inlet. The recirculation from the dead zone can be ingested and, thus, induce further instabilities at the AIP thereby reducing both the inlet and compressor efficiencies, as indicated by Sheoran et al. (2010) in their study of variable APU plenum performance. Yagi et al. (2010) reinforced that understanding of these flow structures in the plenum before they enter the annulus through their investigation of inlet plenum optimization. Their major finding was that an optimized inlet plenum can increase compression system efficiency by up to 4% and increase operability of the compressor.

Further investigations to characterize the flow structure within a radial-to-axial inlet plenum were conducted both experimentally with three-hole probes and numerically by Michelassi and Giachi (1997) and Pazzi and Michelassi (2001). Both efforts were investigating the effect of the radial-to-axial bend in the inlet plenum and, for all cases, found that the computed Mach numbers from the numerical models were higher at top dead center (TDC) than in the experiment. In both cases, this was attributed to computational fluid dynamics (CFD) overpredicting the axial extent of a separation bubble along the shroud wall of the annulus downstream of the high momentum entering the annulus. Further experimentation using five-hole probes with comparison

to a computational simulation was conducted by Han et al. (2015). A higher Mach number at TDC in the annulus was also predicted by the numerical simulation in this study but to a much lesser extent than that of Michelassi and Giachi (1997) and Pazzi and Michelassi (2001). A significant finding of this effort, however, was that CFD predicted the ingestion of the dead zone recirculation, whereas this was not apparent in the experiment data.

As well as sizing of inlets and an understanding of the flow structure developed through the inlet plenum, the use of guide vanes as a method of reducing the flow non-uniformity at the AIP has also been a subject of interest. These vanes are employed in the bend where flow is turned from radial-to-axial, and the method was confirmed to be a viable method to reduce distortion at the AIP by both Saladino and Bielecki (2002) and Kim and Koch (2004). The orientation of these vanes was also investigated by Xin et al. (2016) whereby a radial-to-axial inlet without guide vanes was compared with one incorporating evenly distributed vanes and another with unevenly distributed vanes that were oriented to be incident to the incoming plenum flow. The unevenly distributed vanes significantly reduced the distortion at the AIP. The designs used in these investigations, however, were conducted at low Mach numbers, which reduced the significance of total pressure loss across the vanes. In plenums that experience high mass flow rates, these designs are untenable due to the mechanical stresses the vanes would be subject to as well as increased total pressure loss incurred across the vanes at higher Mach numbers.

### **1.3.2 Rectangular Elbow Duct Flows**

Flow characteristics through 90° bends have been well understood in the fluids community for some time. When a fluid enters a bend, it is driven downward by an adverse pressure gradient on the top side of the wall. This pressure gradient creates a zone of high static pressure at the top of the bend and a low-pressure zone on the bottom. This develops a twin-swirl secondary flow pattern and reversed flow from the top side of the elbow is not uncommon, depending on the flow regime and if there is a potential generated by downstream components. The development of twin-swirl along with the typical static pressure profile is illustrated in Figure 1.5.

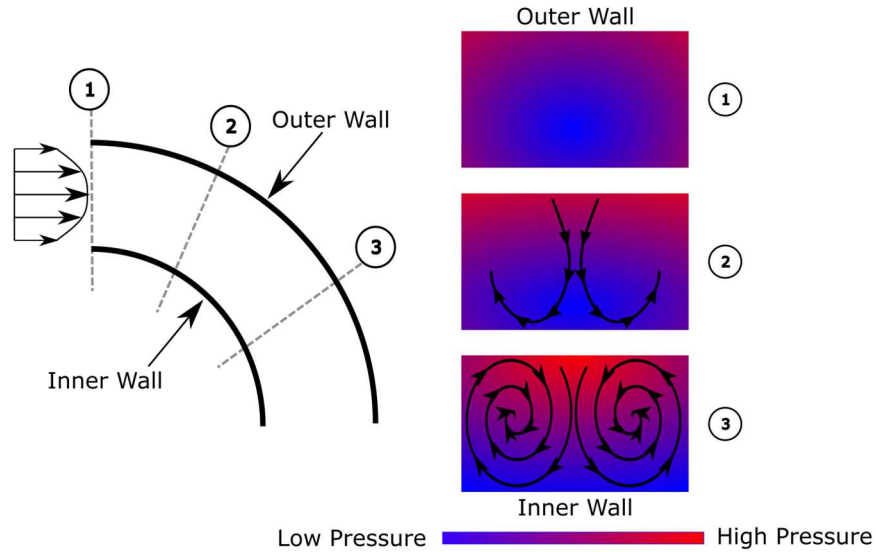


Figure 1.5. Graphic of twin-swirl development through a rectangular elbow duct due to pressure gradients

For APU inlets, ducting is typically of a rectangular cross section, which adds the complication of corner separation and contributes to the regions of high pressure. This is also represented in Figure 1.5 as high-pressure regions in the corners of the top wall of the duct. Many experiments have been conducted using laser doppler velocimetry (LDV) to characterize fluid motion through a 90° bend.

Enayet et al. (1982) performed an LDV investigation of both laminar and turbulent flow through a circular cross sectioned pipe that included a 90° bend with a low radius of curvature. The measurements indicated regions of high velocity on the bottom side of the bend and the development of twin swirl structure. Additionally, turbulence intensity increased along the pipe walls in the streamwise direction and ranged up to 10% on the top wall of the bend at 83% of streamwise length of the passage. The authors noted that this investigation found similar flow structures to Humphreys et al. (1981) where a rectangular cross section duct was used.

Rectangular cross section 90° bends have also been interrogated utilizing LDV by Humphreys et al. (1981), Sudo et al. (2001), and Lou et al. (2015). Humphreys et al. (1981) found that at the entrance to the duct, the pressure gradient emanating from the outer wall produces a potential field that reduces the flow velocity along the outer wall before the entrance plane and causes an acceleration along the inner wall. Furthermore, they indicated that values of turbulence intensity at the exit plane of the bend reached levels of up to 15% along the outer and side walls with values of up to 9% experienced on the inner wall. The flow structures through the bend found

in Humphreys et al. (1981) showed agreeance with the structures outlined in Figure 1.5. Further study by Sudo et al. (2001) indicated that the acceleration of fluid along the inner wall and deceleration of fluid along the outer wall was not apparent after  $30^\circ$  of the bend is traversed. The primary flow stream was then deflected toward the outer wall from the inner. They also indicated that the flow at the exit plane of the bend was greatly distorted and contained large velocity gradients along with high turbulence intensities. The work presented by Lou et al. (2015) scrutinized flow through a rectangular cross section elbow. The exit flow was exhausted from the  $90^\circ$  bend through a tangent duct of same cross-section as the exit plane, and the elbow was fed by a diffusing duct that included splitter vanes to prevent diffusion related mixing loss. This presented a distorted flow structure before the flow entered the bend, however, the same low momentum region along the outer wall at the entrance to the bend existed and even exhibited reverse flow at some spanwise measurement planes. An important finding from this effort, was that the  $90^\circ$  bend provides a medium for the intensity of velocity gradients to be reduced. The authors also note that the vorticity increases from inlet to exit of the bend and LDV streamline contours present similar flow structures to that of Sudo et al. (2001) where the high momentum stream of flow migrates from the inner wall to the outer wall at roughly  $30^\circ$  along the passage.

Investigations have been undertaken to develop turning vanes to prevent the secondary flow structure through an elbow. Kim et al. (2001) conducted a numerical investigation into methodologies to reduce the development of the distortion through a  $90^\circ$  elbow of a circular cross section centrifugal compressor inlet. The effort made use of turning vanes through the  $90^\circ$  bend that were oriented parallel to the outer and bottom walls. Designs including turning vanes did reduce both pressure and swirl distortion at the compressor face significantly, but at the loss of total pressure recovery and efficiency of the inlet. The streamwise length of these vanes directly affected inlet performance.

### **1.3.3 Circular-to-Rectangular Duct Flows**

Circle-to-square or -rectangle ducts are used in experiment setting when it comes to characterizing an APU inlet. Often, mass flow rate in these experiments is measured using a calibrated bellmouth or venturi, which are designed with a circular cross section. The cross-sectional change from a circle to a square produces several secondary flow phenomena that can contribute to reductions in inlet pressure recovery and inlet efficiency.



Davis and Gessner (1992) performed an experimental investigation of the flow structure developed from a circular-to-rectangular duct using a wind tunnel. Total pressure, static pressure, and hot-wire data were acquired to fully define the flow through the duct. The corner separation at the exit of the duct was driving the formation of a vortex pair along the exterior walls of the rectangular section. The blockage due to this flow structure grew as flow moved further downstream and the geometry progressed further to a rectangular cross section creating more diffusion. This induced a low momentum region in the corners as well as on the top and side walls with the region along the shorter side walls being appreciably more affected. A graphic of the momentum change driven by this secondary flow is presented in Figure 1.6.

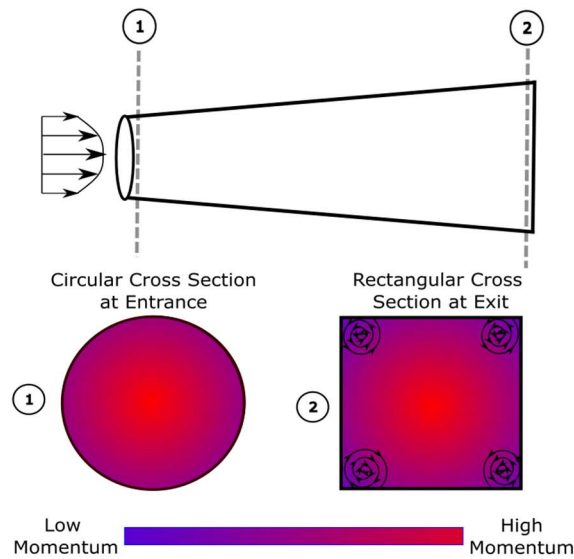


Figure 1.6. Illustration of flow momentum structure of circular to rectangular ducts

Pao et al. (1994) performed a numerical simulation of similar geometry, which used a structured grid and the two-equation k-epsilon turbulence model and compared this to measured data. The computational model agreed well with measured values, and flow separation was captured correctly. Their findings agreed with Davis and Gessner (1992) and indicated that the static pressure increases in the corners duct during the transitional section. The separation zone also increased in size and magnitude further as the cross-sectional geometry grew in area and tended toward the rectangular shape.

## 1.4 Generation of Inlet Distortion Patterns

Several different methods have been developed to generate specific types of distortions and even replicate distortions created during distinct aircraft operation modes. Testing of different distortions can also be conducted simultaneously to determine compressor response to coupled effects (Cousins et al., 1994). Total pressure deficits are often generated using screens for testing and are located axially upstream of the AIP. The finer the mesh of the screen, the larger the total pressure deficit due to increased total pressure loss from added surface friction. These screens may be of a simple geometry to investigate the specific effects of radial or circumferential total pressure deficits on compressor performance.

This method was used by Ariga et al. (1983, 1987) with honeycomb screens located upstream of the AIP. In these experiments, 50% of the inlet area was blocked up to the impeller face. This allowed the investigators to isolate the effects of pure hub, tip, and circumferential distortions on compressor performance. Employing screens such as these is often utilized to characterize compressor stability to purely radial or circumferential pressure distortions (AIR1419C, 2017). Cousins et al. (1994) also used mesh screens that covered the flow path in increments of  $60^\circ$  to vary the extent of the AIP experiencing circumferential pressure distortion to characterize the stability of an engine with a two-stage centrifugal compressor.

With the use of modern CFD modelling techniques, distortion patterns with further complexity have been replicated. Frohnepfel et al. (2016) utilized CFD optimization to generate mesh screens of varying density to replicate complex total pressure patterns encountered by an engine located downstream of a boundary layer ingesting serpentine duct. A set of stream vanes were also developed in this effort to generate the swirl pattern through the complex inlet that was predicted by CFD. These swirl vanes were also installed upstream of the impeller. The use of screens and turning vanes in the narrow axial passage of a radial-to-axial inlet, however, is untenable. Access to the axial section of the inlet is often impossible and, if installed, the mechanical stresses on the distortion generators would be immense due to the high Mach numbers in the axial flow section for high mass flow rate machines.

To generate distortion patterns in an APU plenum a method of moving the baffle in the plenum and blocking sections of the radial flow inlet was developed by Sheoran and Bouldin (2008) and proven using CFD to generate the intended swirl patterns. A graphic of one of these plenums is presented in Figure 1.7.

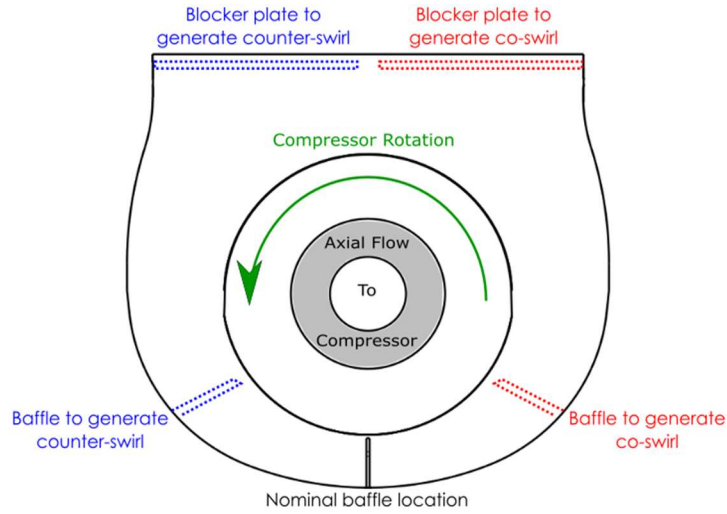


Figure 1.7. Typical APU plenum distortion generator geometry

Sheoran et al. (2010), and Lavan Kumar et al. (2013) have made use of these APU plenum distortion generators in experiments by installing baffles and blocker plates in different locations to replicate specific swirl patterns experimentally and computationally. Sheoran and Bouldin (2008) and Sheoran et al. (2010) proved that offset swirl can be generated by replacing the BDC baffle with one clocked counterclockwise or clockwise depending on the desired dominant swirl behavior. They also demonstrated that the severity of the swirl distortion can be increased by moving the baffle further from BDC. In both cases blocker plates were shown to generate bulk swirl or offset swirl depending on the amount of blockage. Lavan Kumar et al. compared CFD results to flow visualization conducted during experiment within the APU plenum. The surface flow patterns through the plenum showed good agreement with CFD flow structures, indicating that CFD can be used to develop these variable inlet plenums with acceptable results.

### 1.5 Inlet Distortion Effects on Centrifugal Compressors

Different types of inlet distortions have varying impacts on compressor performance, stability, and aeromechanic forced response. Compressors are typically designed for axisymmetric inflow for best performance; thus, significant distortions will alter compressor performance and stability detrimentally. Moreover, aeromechanical excitation can occur due to distortion effects

and lead to fatigue failure of the compression system if not correctly distinguished and considered during the design phase.

### 1.5.1 Performance

Pressure and swirl distortion have discrete influences on the performance of centrifugal compressors. When coupled, the effects can be complex, and it can be difficult to attribute the performance affects to each type of distortion. To this end, the effects of each distortion should be analyzed separately before coupled affects can be separated.

#### *Effect of Pressure Distortion on Compressor Performance*

Regions of lower total pressure represent regions with lower kinetic energy. This implies that the axial velocity into the compressor is reduced, thus, lowering the mass flow rate into the rotor thereby increasing incidence for the same rotational velocity (Ariga et al., 1983). Figure 1.8 is a representation of the velocity triangles at the inducer under pressure distortion with this reduction in axial velocity represented. This change in incidence and mass flow rate has a significant impact on performance.

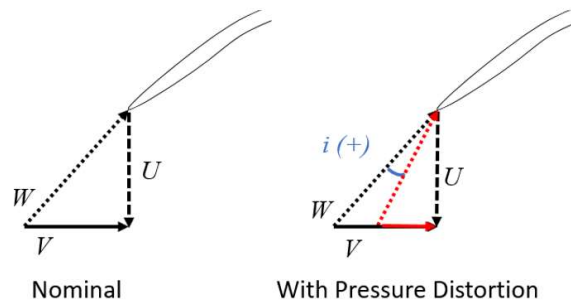


Figure 1.8. Velocity triangles at the inducer including effect of pressure distortion

To quantify the effect of total pressure distortion on the performance of a centrifugal compressor, Ariga et al. (1983) performed experiments with honeycomb screens that covered 50% of the inlet annulus that generated hub, tip, and circumferential pressure distortion. TPR was reduced for all cases but least for circumferential distortions and most for radial hub total pressure deficits. Efficiency was slightly reduced for the circumferential distortion and significantly

reduced for tip distortions. Counterintuitively, compressor efficiency at high loading under hub-side distortion was found to be higher than the nominal case.

The experiments conducted by Kim et al. (2001) compared the effect of different inlet configurations on the performance of a centrifugal compressor. These configurations presented a coupled swirl and total pressure profile. The authors noted that total pressure loss through the inlet system does not have a dominant effect on the efficiency of the compression system. Total pressure ratio was reduced for inlets that included a bend due to the secondary flow pattern generated by the pressure gradients required to turn the flow through the bend. This effect was amplified for bends that contained smaller radii.

The use of multiple geometry screens to investigate the effects on centrifugal compressor performance at off-design conditions was presented by Sitaram et al. (2012). Their findings showed that at off-design conditions, the total pressure ratio of the compression system remained unaffected by the total pressure distortion induced by the installed screens. This agreed with the findings of Kim et al, (2001) that compressor efficiency was reduced as the distortion intensity and extent was increased. Sitaram et al. (2012) also noted that circumferential pressure distortion has a larger impact on compressor loading and flow coefficients than radial distortions.

### ***Effects of Swirl Distortion on Compressor Performance***

Swirl distortion also has a significant impact on compressor inlet velocity triangles. The circumferential swirl angle alters the velocity triangle at the inducer by reducing the absolute velocity flow angle, thereby changing incidence (AIR5686, 2017). For co-swirl, the inlet absolute flow angle is increased, which decreases incidence and loading. The opposite is true for counter-swirl as defined by a negative change in absolute flow angle and increase in incidence and loading. Figure 1.9 shows this effect at the inducer for an impeller designed for purely axial inlet flow.

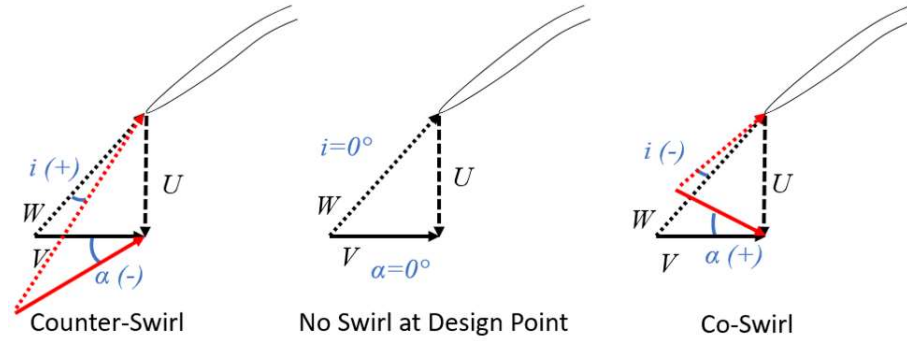


Figure 1.9. Velocity triangles at the inducer including effect of swirl

These incidence changes have numerous impacts on compressor performance. In terms of TPR, increased compressor loading increases TPR. Thus, co-swirl reduces TPR, and it is increased under counter-swirl due to changes in loading influenced by the change in incidence. Mass flow rate is also impacted, as represented in the velocity triangles in Figure 1.9. Counter-swirl increases the mass flow rate, represented by a longer axial velocity in the velocity triangle, and co-swirl reduces the axial velocity and, therefore, the mass flow rate into the compressor. These effects are greater for co- or counter-rotating bulk swirl when compared to offset swirl, where the effects are reduced but still dictated by the predominant swirl value. Compressor efficiency is also reduced by swirl as the change in incidence causes additional separation to be incurred within the impeller passage as well as changes the machine flow acceptance.

To analyze the impact of swirl on compression system performance, Sheoran et al. (2012) presented a numerical simulation of an axial compressor coupled with a variable radial-to-axial inlet to generate distortion. They clearly indicated that the compressor efficiency was reduced under any form of swirl. They also indicated that TPR and mass flow rate is increased with counter-swirl and reduced with co-swirl. Their CFD made use of both frozen rotor and a sliding mesh technique. They concluded that frozen rotor matched the undistorted rig data well and was able to be used for the distortion cases.

Further research into centrifugal compressor performance experiencing swirl distortion was undertaken using a parallel compressor analysis by Bouldin and Sheoran (2007). Their research indicated that the performance effects of swirl on an axial compressor matched those of centrifugal compressors. Co-swirl decreased mass flow rate and TPR, whereas counter-swirl increased both parameters and the extent of these regions dictate the predominant effect on

performance. Offset swirl pairs had a lesser effect on performance than those of bulk-swirl because of the counter-acting effects the two different types of swirl distortion patterns have on performance.

### 1.5.2 Stability

Distortion has a strong relationship with the stability of centrifugal compressors. As shown in both Figure 1.8 and Figure 1.9, the effects of pressure and swirl distortion change the impeller incidence. This leads to premature surge in many cases due to the inducer stall occurring at higher mass flow rates. The separation from the stalled inducer propagates downstream in the impeller channel reducing the amount of relative diffusion that can occur due to the blockage incurred. This effect continues through the machine to the diffuser as the change in impeller flow field leads to a change in diffuser vane incidence. This, in turn, can create more blockage in the diffuser passage due to diffuser vane stall, which is a precursor to surge. These effects reduce the surge margin of the compressor as shown in Figure 1.10. Surge margin is calculated with equation (1.3) and is a quantitative measure of how far the compressor operating point is from the surge point:

$$SM = \frac{TPR_{surge} - TPR_{design}}{TPR_{design}}. \quad (1.3)$$

Understanding the flow that is being ingested by the impeller is crucial to designing the correct incidence for the inducer and increasing surge margin.

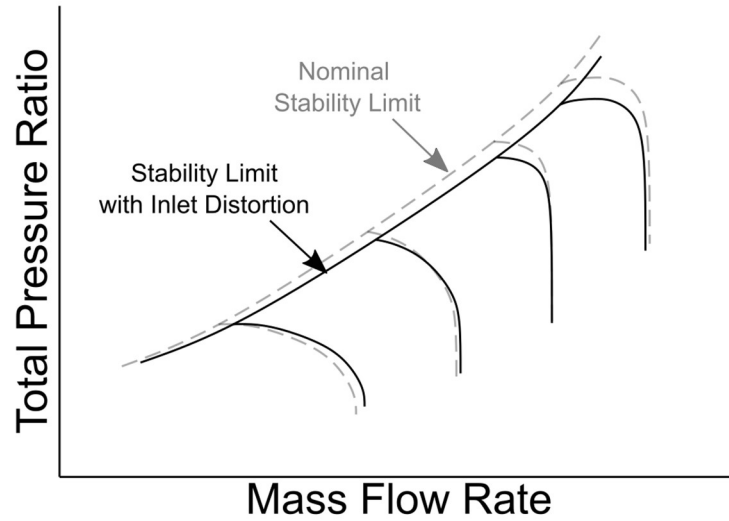


Figure 1.10. Speedline representation of stability limit degradation under inlet distortion

The impact of total pressure non-uniformities on the onset of inducer stall of a centrifugal compressor was a subject of further experimentation conducted by Ariga et al. (1987) with the same honeycomb setup as their effort from 1983. The conclusion was that radial distortions increase the mass flow rate and, therefore, decrease TPR where stall begins, but stall inception under circumferential distortion occurred at a minorly reduced flowrate from the nominal case. This is logical from a fluid mechanics perspective, as areas of lower total pressure are regions of lower velocity if the static pressure at the compressor face is considered constant. This leads to areas of lower velocity at the inducer, causing the onset of stall to be at a higher flowrate.

In the work Bouldin and Sheoran (2007) undertook using parallel compressor analysis on a centrifugal compressor, the effects of surge margin were analyzed along with performance metrics for different swirl distortion patterns. Their findings were that twin swirl is as deleterious to surge margin as bulk co-swirl. However, bulk co-swirl also increased surge margin due to the reduced loading attributed to the lower incidence at the inducer because of the increase in inlet absolute flow angle.

Vagnoli and Verstraete (2014) conducted an unsteady computational study of a transonic centrifugal compressor stall inception due to inlet distortion. The distortion was incurred by a 90° bend upstream of the impeller eye, and this case was compared to a straight pipe configuration. The tip leakage vortex showed a transient behavior and interacted with adjacent blades causing areas of blockage to migrate through different impeller channels in a phenomenon known as mild



impeller rotating stall. The authors indicated that in the bent pipe configuration, the incidence of the tip of the inducer is higher than that of the straight pipe case, leading to rotating stall and an abrupt onset of surge. Furthermore, there was limited difference in compressor performance at the stability limit between the two pipe configurations due to the aerodynamic effects of the system being dominated by those of the centrifugal effect.

### 1.5.3 Forced Response

It is essential to characterize the forced response of a centrifugal compressor and any potential effects from coupling with its inlet components. Aeromechanical excitation is an unsteady phenomenon whereby an impeller resonant frequency crosses with the frequency of wakes shed by upstream inlet components or potential fields generated by the downstream diffuser. The pressure changes from wakes and potential fields cause unsteady loading of the impeller. The Airbus A300 APU suffered from high cycle fatigue caused by aeromechanic forced response due to both strong total pressure and swirl distortions interacting with the compression system (Lotter and Jörg, 1982). To alleviate this, an APU inlet redesign was required to be undertaken at significant cost. Therefore, understanding the flow field at the AIP and its interaction with the compression system is vital to extend the life of rotating components.

To determine the cause of the unsteady loading, the frequency of loading fluctuations within the impeller are taken as relative to the frequency of impeller rotation. This is known as an engine order, EO, and is calculated using equation (1.4), and this number can be used to determine which compressor component the excitation can be contributed to:

$$EO = \frac{f_{fluctuation}}{2\pi\omega_{impeller}} . \quad (1.4)$$

Therefore, characterizing the distortion developed through the inlet is critical to understanding if any major resonant frequencies will be excited during compressor operation. An impeller can have multiple modes that affect different components; for example, main blades have a different resonant frequency than a splitter blade. When modes are excited, the impeller endures high values

of strain, and therefore, high stresses which can lead to fatigue failure or even catastrophic failure depending on the magnitude of the stress encountered.

Both the multiple-pre-rev, MPR, of pressure distortion and swirl pairs, SP, of swirl distortion contribute to the unsteady loading of the impeller blades and can generate a forced response. For example, a pressure distortion profile with an MPR of 5 that can excite a 5 EO is shown in Figure 1.11.

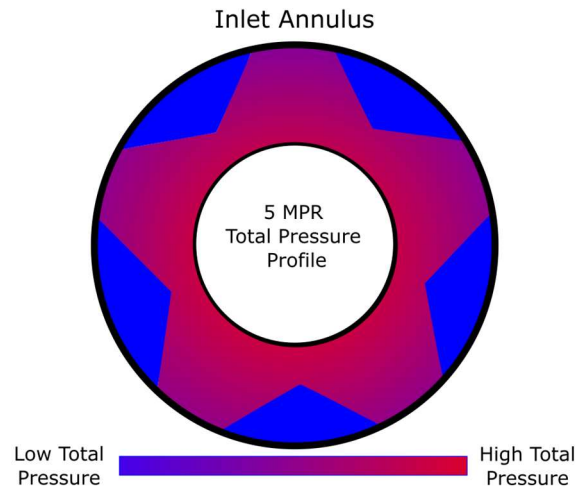


Figure 1.11. Example of a 5 MPR total pressure profile in an inlet annulus

If this total pressure distortion is developed through an inlet that is matched with an impeller that has a strong resonance that is a multiple of 5 of the rotational speed along the operating profile, the impeller is more likely to suffer fatigue failure since it cycles through the strong mode frequently. The relationship between rotational speed and engine orders is characterized using a Campbell diagram. These are graphs with frequency on the abscissa and rotational speed on the ordinate with EO being represented as a line of constant slope equal to the number of the order (Cumpsty, 1989). Along these EOs, the crossings of resonant frequencies are marked and the magnitude of the forced response, usually as strain, are identified. Figure 1.12 is an example Campbell diagram that has a strong 5 EO response that if coupled with the total pressure profile from Figure 1.11 would experience severe mechanical excitations at rotational speeds of 3000 and 4000 RPM. This would be an undesirable pairing of an inlet and compressor due to the severity of the modes that would be excited.

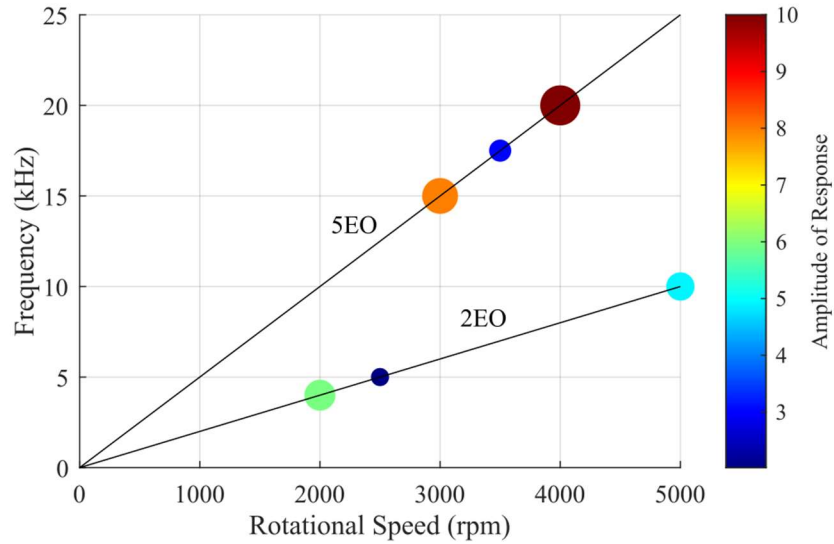


Figure 1.12. Example Campbell diagram for a compressor with strong 5EO responses

A similar situation to that described above was investigated by Zemp et al. (2008) where an inlet with a 5 MPD distortion pattern was paired with an impeller with a strong resonant frequency that crossed a 5EO in the operating profile. An unsteady CFD simulation was conducted to investigate the forcing function due to inlet distortion of the impeller. The model utilized steady CFD to match compressor performance parameters as a verification of fidelity before being used for unsteady simulations. The authors found that unsteady CFD matched experimental pressure fluctuations with a maximum difference of 10% along the shroud. Their simulations also indicated that the largest magnitude of pressure variations within the impeller were located at the inducer and was, thus, the most affected by forcing functions.

Further studies on forced response in a centrifugal compressor were conducted experimentally by Kammerer and Abhari (2010) using 5 and 6 MPD pressure distortion screens. The inlet and paired compressor used in the investigation showed 2 and 3EO pressure fluctuations due to struts in the annulus that generated 2 and 3 MPD pressure distortion patterns. The pressure variations within the impeller increased in magnitude at higher rotational speeds. With the distortion screens, they were able to induce 5 EO and 6 EO modes along the operating profile of the centrifugal compressor that were not excited by the nominal inlet configuration. Their data indicate that the introduction of these screens did not reduce the magnitude of the 2 and 3EO responses, but the 5 MPD screen increased the magnitude of pressure fluctuations along the

impeller blade surface, and therefore, the strain that the impeller would experience. This suggests that when intentionally perturbing the flow to generate a forced response, the effect of inlet components, such as struts, are not washed out and will still influence the flow profile experienced by the impeller.

The study presented by Xin et al. (2016) on radial-to-axial inlet flows was accompanied with an analysis into the effect of the different inlet plenum configurations on the unsteady pressure loading along the impeller blade. They indicated that APU plenums without guide vanes have higher pressure fluctuation amplitudes for lower harmonics. The authors also noted a strong 18 EO response due to their installation of 18 guide vanes upstream of the AIP.

## **1.6 Research Objectives**

Research in the open literature currently has no specific guidelines as to what is required for accurate modelling of an APU inlet to achieve an adequate understanding of distortion behavior. Computational efforts have used models that only consider sections of inlet geometries, without comparison to a full fidelity model. As previously mentioned, the radial-to-axial inlet is considered the dominant factor on flow structure at the AIP, and some researchers have only modelled this component, but support for this in literature to validate this methodology is sparse. Therefore, the effect of this reduced modelling is not well understood and could lead to significant AIP flow differences that would propagate to erroneous design choices.

The objective of this effort is to determine how much of an inlet needs to be modelled to correctly characterize the flow structure at the AIP and to develop a reduced model that performs satisfactorily. Two CFD models, one modelling the full APU inlet, and one modeling only the APU plenum, each with seven baffle configurations and four blocker plate configurations were developed to replicate inlet distortion data from the Honeywell SSCC at Purdue University in the APU-inlet configuration. The numerical results are compared to experiment to demonstrate model veracity. Data from the models are used to determine causes of flow disturbances and resolve the impact of individual inlet component geometries on distortion development at the AIP. Furthermore, an analysis of the effectiveness of experiment practices for collection of AIP data is presented and sources of uncertainty identified.

## **2. EXPERIMENTAL AND COMPUTATIONAL MODELS**

Two computational models were generated to replicate the APU inlet geometry used in experiment of a centrifugal compressor. A reduced model that only considered the radial-to-axial inlet of the APU and a more complete model that utilized the entire inlet geometry were generated. The results from these computational models are compared to experiment in this thesis.

### **2.1 Honeywell SSCC at Purdue**

The Honeywell Single Stage Centrifugal Compressor (SSCC) at Purdue University's Zucrow Laboratories was utilized for this inlet distortion investigation. An APU inlet configuration was used along with a variable APU plenum to induce distortion. A comprehensive facility paper was published by Lou et al. (2016) and contains details on the operation and development of the SSCC facility.

#### **2.1.1 SSCC Facility and Operation**

The SSCC is a high-speed centrifugal compressor with a design speed of about 45,000 RPM and TPR of approximately 6.5. A rendering of the facility with the compressor in the APU inlet configuration is presented in Figure 2.1. The impeller is designed for counterclockwise rotation and is comprised of 17 main and 17 splitter blades. Paired to the impeller is a vaned diffuser with 25 aerodynamically shaped vanes. The vaneless radius ratio for this compressor is 5%. The impeller is driven by a 1400 horsepower AC motor that is linked to a 30.46:1 ratio gear box to increase the rotational speed of the compressor shaft. Control of the motor is handled by a variable frequency drive that can maintain motor mechanical speed within 0.1 RPM of the input value. A monopole sensor is used to determine mechanical speed of the compressor. The gearbox shaft is coupled to a crowned spline shaft, which increases the tolerance for misalignment between the gearbox and exhaust plenum. A torque tube, containing squeeze film dampers and an axial spring, is situated between the crown shaft and compressor drive shaft to reduce system vibration. The mechanical stress on the impeller is monitored using strain gauges that are wired to a slip ring located at the forward end of the compressor drive shaft. Slip ring coolant is supplied by an external cart with a coolant reservoir and pump. Gearbox and compressor vibrations are measured using

accelerometers and monitored in real time. Shaft orbits were also monitored using Bently probes. The constant-speed operating point of the impeller is manipulated by altering the throttle setting. The throttle is a rotating cuff that limits the mass flow rate through the machine and is located within the exhaust plenum.

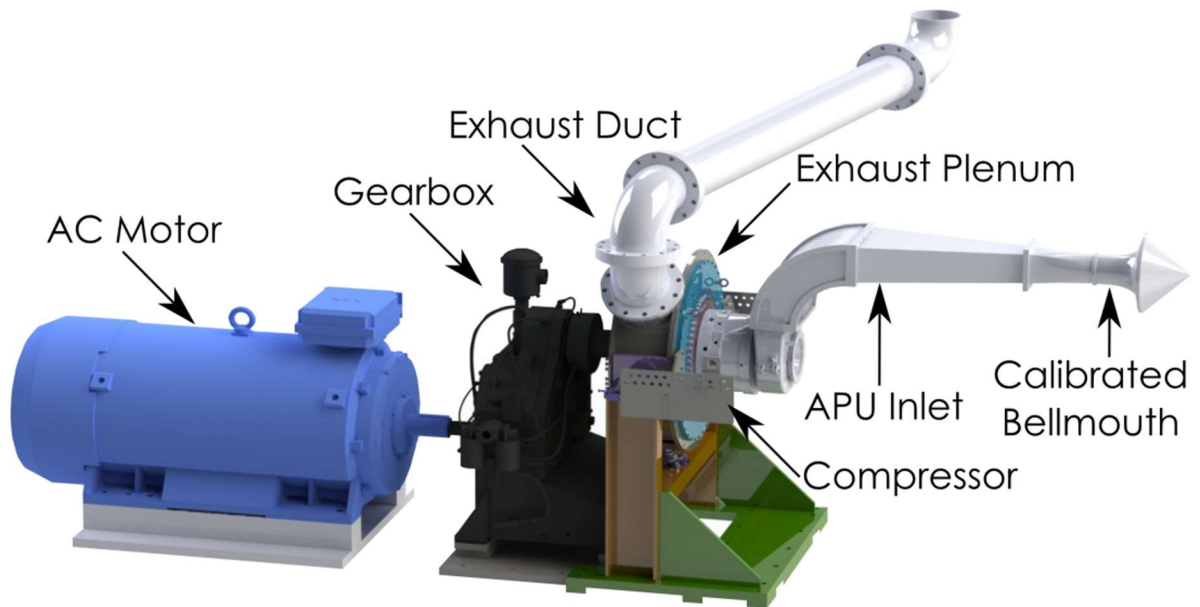


Figure 2.1. SSCC facility with APU inlet installed

Air is drawn into the compressor through an ASME calibrated bellmouth, with a beta ratio of 0.387, to measure the mass flow rate entering the machine. The bellmouth is covered by a cone shaped low-density FOD screen, as depicted in Figure 2.2. Ambient temperature and pressure conditions are measured in front of the FOD screen. A hygrometer is also located upstream of the bellmouth to measure relative humidity. The humidity measurement is used in conjunction with ambient temperature and pressure readings to calculate fluid stagnation speed of sound, stagnation density, and ratio of specific heats using REFPROP. This information allows for the correction of speed and mass flow rate to reference conditions of 59°F and 14.696 psi using equations (2.1) and (2.2), as well as the calculation of Mach number using isentropic relations (Berdanier et al., 2015):

$$N_c = \frac{N_{mech} a_{ref}}{a_{01}} \text{ and} \quad (2.1)$$

$$\dot{m}_c = \frac{\dot{m} \rho_{ref} a_{ref}}{\rho_{01} a_{01}} . \quad (2.2)$$

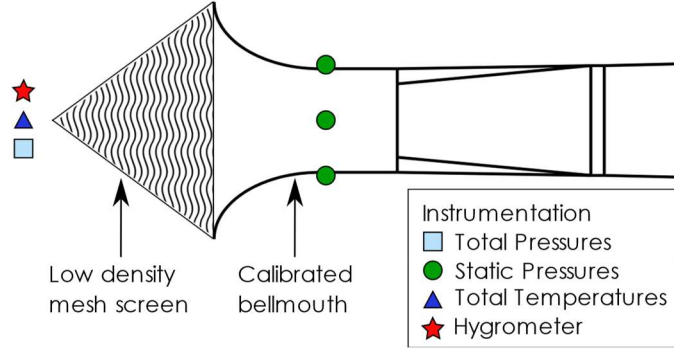


Figure 2.2. SSCC APU calibrated bellmouth geometry and instrumentation

Compressor performance is determined using a LabView code in conjunction with numerous steady temperature and pressure measurements. Steady static and stagnation differential pressure measurements were acquired using two Scanivalve DSA 4000 enclosures each comprising of 16 DSA 3016 modules. These modules have an indicated uncertainty of 0.06% of the module full-scale pressure reading, which are 2.5, 5, or 100 psi depending on the module. The reference pressure for the DSA modules, along with the back-face bleed venturi total pressure, was collected using a Rosemount absolute pressure transducer with ranges of 13 to 15 psi with an uncertainty of 0.05% of the total measurable range. Calibrated bellmouth static pressure, ambient total pressure, and back-face bleed venturi pressure drop were acquired using 13 to 15 psi Mensor pressure transducers with an associated full scale uncertainty of 0.01%. The mass flow rate was calculated from the bellmouth static pressure and ambient total pressure utilizing a calibration curve. Static and total temperatures were obtained using a mix of K- and T-type thermocouples that were read using two 40-channel Agilent 34980 enclosures.

The SSCC bleeds air flow through a port located behind the back-face of the impeller. The mass flow rate through this port is measured by a venturi flow meter, and the quantity of flow extraction is controlled by a pneumatically actuated globe valve. For this test campaign, the back-face bleed flow was maintained at 1% of the mass flow rate into the compressor. A globe valve

was used to regulate the flow rate leaving the thrust piston to change the amount of thrust removal from the compressor shaft.

The lubrication system for the SSCC is monitored in real time using LabView and was assessed using temperature, pressure, and flow rate measurements of the compressor and gearbox oil systems. The forward, aft, torque tube, and slip ring bearings are lubricated by the compressor oil supply. Flow pressure to each location is set by upstream regulators. Flow rates to each of these bearings are monitored and can be manipulated during testing by altering the supply pump RPM using a VFD. Heat rejection of the oil from the compressor supply is conducted by a single heat exchanger that is controlled automatically by a VFD to maintain the oil temperature below a specified value. Gearbox lubrication is achieved separately from the compressor system. This system uses two heat exchangers, plumbed in parallel for heat rejection. These heat exchangers are manually operated, and the amount of heat rejection is changed by manipulating the heat exchanger fan speed using a VFD.

A total of five air load regulators are used, in conjunction with electropneumatic controllers, to supply buffer air to manage carbon seals, thrust, and air ejection. The first air load regulator is used upstream of the other four plumbed in parallel and is used to step down 2000 psi air to approximately 100 psi, as commanded by an ER5000 controller. The 100-psi air is passed through four different air load regulators, all utilizing ER3000 controllers. Two of these regulators are utilized to maintain pressure across carbon seals in the forward and aft cavities to prevent oil leakage into the compression system. A further pneumatically actuated regulator is used to control flow injection into a thrust piston that is used to remove thrust from the compressor shaft that is generated by the impeller. The final regulator coupled with an electropneumatic controller is used to control the motive air supply to an ejector that provides suction upstream of the impeller within the flow path.

Tip clearance can be manipulated and is monitored using a total of 12 capacitance probes; with 4 each located at the inducer, impeller knee, and the exducer at different circumferential locations. The compressor shaft can be actuated to move axially within the torque tube assembly during testing using a precise stepper motor. This motor allowed axial displacement changes in increments of 0.0001 inches. This allowed tip clearance to be accurately maintained at all operating points.



### 2.1.2 APU Inlet Configurations

The APU-style inlet of the SSCC was used for this campaign and is comprised of a calibrated bellmouth, circle-to-square transition duct, flow spreader duct, rectangular 90° elbow, and a radial-to-axial inlet. Figure 2.3 is an exploded view rendering of these components. The circle-to-square transition duct allowed for the cross section change between the calibrated bellmouth and the flow spreader duct. The ratio of the exit area to inlet area for the transition section was 1.429, and the transition from circular to square cross section occurs within 1.875 pipe diameters. A flow spreader duct is mated to the transition duct exit and consists of a diffusing duct with 5 spreader vanes located symmetrically about its center axis. The area ratio of the spreader duct is 3.373, and the exit flow enters a 90° elbow with the same cross section as the spreader duct exit. The elbow duct has a curvature ratio of 1.873 and maintains the same cross section profile through the bend. The bellmouth, transition duct, and elbow were the subject of LDV studies conducted by Lou et al. (2015). In the LDV investigation, the flow exited the elbow into a tangent duct, whereas in the APU inlet configuration, flow enters an APU plenum. Flow is turned from radial-to-axial within the plenum and is directed to the impeller through a converging annulus.

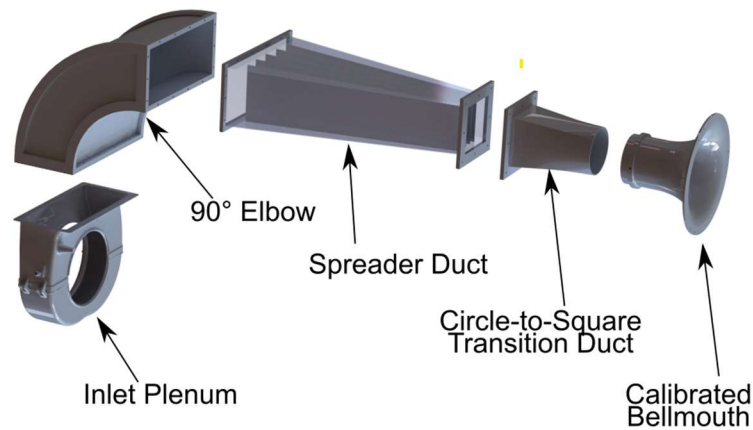


Figure 2.3. SSCC APU inlet components

To generate distortion patterns, a variable APU plenum was utilized. Geometry of the plenum is akin to the variable plenum geometry presented by Sheoran et al. (2010). Different removable baffle configurations were installed in the bottom half of the inlet plenum to generate discrete swirl distortion patterns. The baffles were located at 25°, 45°, or 70° on either side of BDC,

as shown in Figure 2.4. Baffle locations are defined as positive clockwise from BDC. The SSCC impeller rotates counterclockwise and, therefore, a positive baffle location will generate counter-swirl with flow biased toward a clockwise rotation in this configuration.

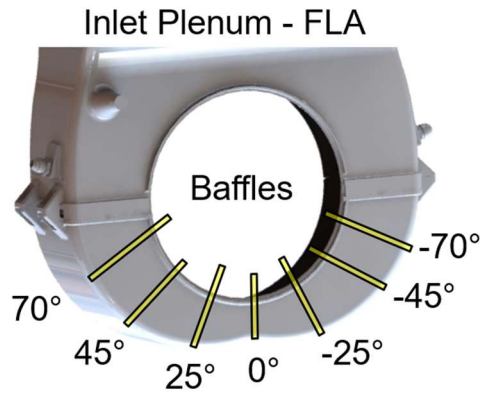


Figure 2.4. SSCC APU inlet baffle configurations

The variable plenum of the SSCC was also able to include blocker plates. These plates were installed at the exit of the 90° elbow at the inlet to the APU plenum. For this effort, 25% and 50% blockage plates were used with flow obstructions being located on the left and right side of the plenum depending on configuration, as depicted in Figure 2.5. Left blockage develops counter-swirl for this compressor, as flow would be biased toward rotating clockwise, which opposes compressor rotation.

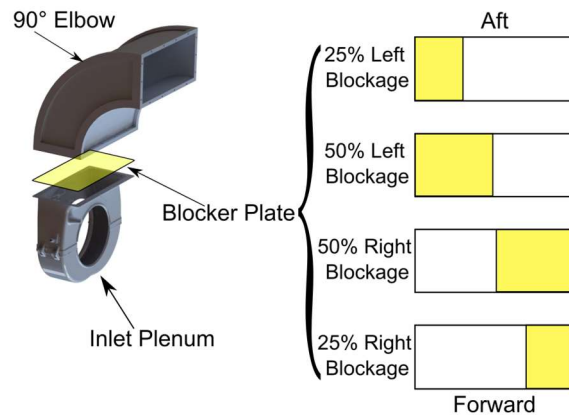


Figure 2.5. SSCC APU inlet blocker plate configurations viewed from above

### 2.1.3 Inlet Instrumentation

In the APU configuration, the flow path is instrumented at the exit of the 90° bend, within the plenum, and at the inlet annulus to characterize flow features as shown in Figure 2.6. A total of 6 rakes, located in a ‘sandwich pack’ between the entrance to the APU plenum and the elbow, characterize the flow exiting the duct. Each rake consists of three Kiel probes to measure total pressure and temperature. These rakes are located at 9%, 25%, 42%, 58%, 75%, and 91% of the passage span with the elements being spaced at 21%, 50%, and 79% of the width of the flow path. Inlet plenum rakes are distributed circumferentially at  $\theta = 45^\circ$ ,  $135^\circ$ ,  $225^\circ$ , and  $315^\circ$ . Each rake contains five Kiel heads, four to measure total pressure and one to measure both total pressure and temperature located at the rake midspan. Four shroud static pressure taps are located at the same radial location as the inlet rakes along the shroud. Two static pressure taps are located along the shroud, progressing into the inlet annulus.

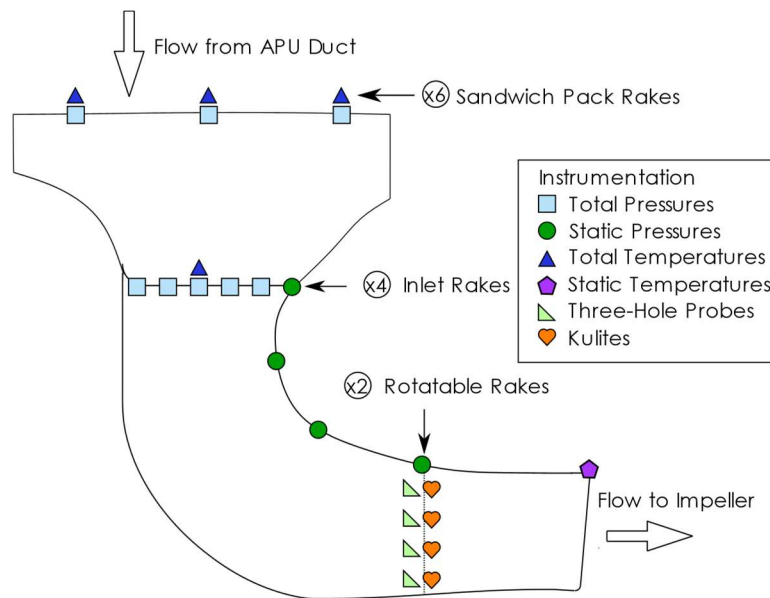


Figure 2.6. SSCC APU inlet plenum and annulus instrumentation

Four rotatable rakes are used to capture flow characteristics at the AIP and are located within the annulus 2.83 probe diameters axially upstream of the inducer. Figure 2.7 is a graphic representation of these rakes and the traverse for a survey of the annulus flow. Each rake has four

elements located at 26%, 48%, 67%, and 84% of the annulus span. An additional static pressure tap is included on each rake along the shroud surface. Two rakes are outfitted with three-hole probes with a trapezoidal head geometry to determine static pressure, total pressure, Mach number, and circumferential swirl angle of the flow at the AIP. Kulites are outfitted to the four element locations of the two remaining rakes to capture unsteady pressure fluctuations. The three-hole probe rakes traversed the top and the bottom half of the annulus, and the Kulites surveyed the left and right halves. The traverse angle between each data point was maintained at  $2.5^\circ$  for this investigation. At the start of a traverse, data are taken at  $0^\circ$ ,  $2^\circ$ , and  $2.5^\circ$ , before the set traverse angle takes effect. Once a survey concludes, an additional two data points are acquired at  $180^\circ$  and  $182^\circ$  from the origin to compare the offset of the opposing rake elements. The total number of data points for each radial ring of rake elements is 153. Therefore, the AIP total pressure, Mach number, and swirl profiles are defined by a total of 612 data points and the static pressure profile by a total of 765 points, due to the added shroud static pressure tap.

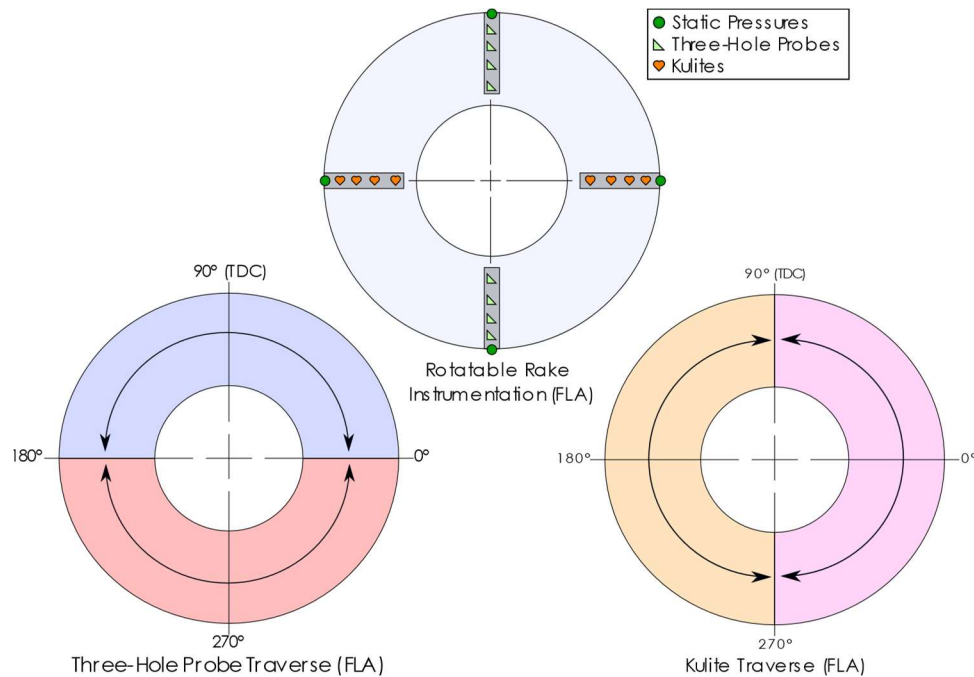


Figure 2.7. SSCC rotatable rake instrumentation and survey traverse

Steady pressure measurements from the three-hole probe and shroud pressure taps were sampled using DSA 3016 modules. Unsteady pressure readings from the Kulites were acquired at

a rate of 100,000 samples per second. The Kulite signals were conditioned by a Precision Filter PF28118 card, and the output was registered by an NI DAQ 6358 module.

## **2.2 Development of Plenum Computational Model**

The reduced inlet model to be investigated in this effort only considers APU plenum components. The findings of Koch et al. (1995) that radial-to-axial inlets mix out the upstream flows that enter through the radial section provided justification for this geometry selection. Thus, the flow from the APU duct should not have a dominant effect on flow features, and this reduced model should provide comparable inlet distortion behavior as that measured in the experiment. This model is presented first, as the method used for the grid convergence of the full-inlet model is dependent on the convergence of the reduced model.

### **2.2.1 Plenum Model Domains and Interfaces**

The reduced model only contained inlet components downstream of the sandwich-pack interface plane (SPIP). For simulations with no blocker plate installed, the model consisted of three domains: the plenum top half, plenum bottom half, and an outlet extension. If the simulation case had a blocker plate installed, an inlet extension domain was included to allow flow to adjust to the blocker plate located just downstream of the SPIP. For the baffle cases, the inlet was defined as the SPIP. A GGI interface was included for the blocker plate simulations at the SPIP between the inlet extension and the inlet to the plenum top half domain. A rendering of the plenum models in these two configurations is presented in Figure 2.8 for clarification. The only other disparity between the models with and without a blocker plate was the installation of the blocker plate itself. Blockage plates were included in the plenum top-half domain immediately downstream of the SPIP, hence the need for of an inlet extension for flow adjustment.

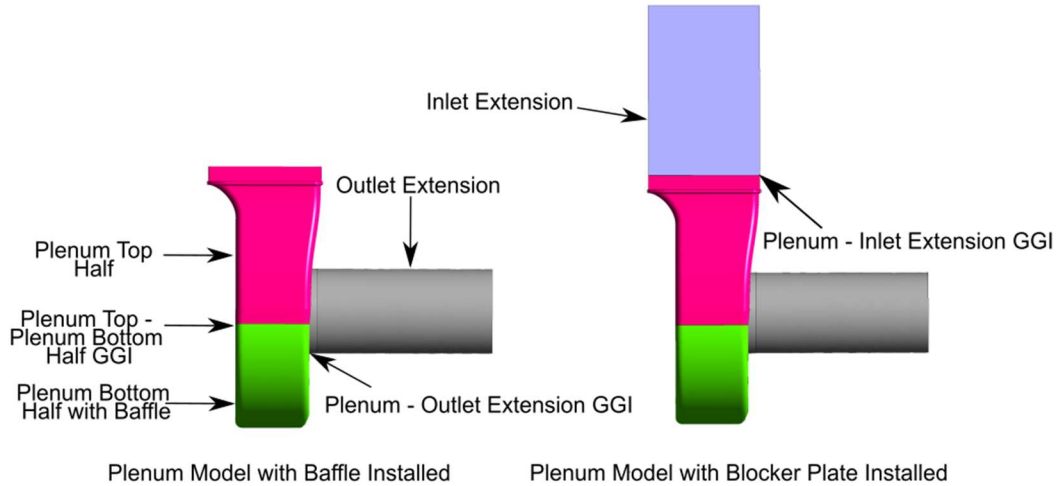


Figure 2.8. Plenum model domains and interfaces

The remaining two domains were common between the baffle and blocker plate cases. The plenum bottom half was mated with the top half with a GGI interface for modularity, as to change the baffle for the simulation only the bottom half mesh had to be substituted. This permitted use of the identical top-half mesh for all baffle simulations. Finally, the outlet extension was connected to the inlet plenum top half at the AIP. This extension included the continuation of the physical annulus geometry. Downstream of the AIP, the shroud continues to converge, which influences the flow field at the AIP and, thus, it should be modelled. At the location of the inducer, an artificial extension section with constant cross section is used. This extension is two annulus diameters in length. The extension is included to facilitate numerical diffusion at the exit of the model.

## 2.2.2 Plenum Model Boundary Conditions and Discretization

Past computational research using ANSYS CFX on the SSCC was conducted by Fuehne (2020) and Brown (2020). Both efforts showed agreement with experiment results. In these efforts, the two-equation BSL turbulence model, which marries the use of the  $k-\epsilon$  model in the freestream and the  $k-\omega$  model along the walls using a blending function, was utilized for all domains. Their justification for using this turbulence model was that it yielded results that matched the experiment closest. Future use of the inlet distortion research presented in this effort is aimed at combining the efforts of Fuehne (2020) and Brown (2020) with APU inlet distortion patterns. This would mean the use of an interface between the impeller domain and the inlet domain. The uses of GGI

interface require that all turbulence numerics are transferable across the interface. Therefore, a two-equation turbulence model that uses a wall scale must be utilized to match with these past models. The options are then limited to using the BSL or SST turbulence models that each make use of the  $k$ - $\epsilon$  model in the freestream and the  $k$ - $\omega$  model along the walls. For this effort, the SST turbulence model was prescribed to all domains. This turbulence model was selected because according to section 4.1.5 of the CFX Solver Modelling Guide (2020), the SST model is the recommended two-equation model as it was developed to overcome deficiencies in the BSL model.

A uniform total pressure deficit was assigned at the inlet plane to mimic the loss of total pressure through the duct. The total pressure loss through the inlet is a function of mass flow rate, and this was established from experiment data. A turbulence intensity value of 10% was assigned to the inlet flow. This approximates the intensity values found at the exit of a 90° elbow from LDV investigations by Humphreys et al. (1981) and Enayet et al. (1982). For the outlet boundary condition, mass flow rate was assigned. The mass flow rate values were taken from experiment because the compression system dictates the amount of mass flow that is being pulled through the inlet. The compression system's ability to accept the mass flow rate is influenced by distortion. Therefore, to correctly model the inlet under operating conditions, corrected mass flow from experiment had to be used. The reference pressure and temperature were assigned as sea level standard values of 14.696 psia and 59°F, respectively. Therefore, the value of mass flow rate that was prescribed at the outlet was the corrected mass flow rate value measured in experiment, as this value of mass flow is corrected to sea level reference conditions.

Surface roughness for the inlet hub and shroud were determined using the method presented by Fuehne (2020). Sand grain roughness values for the inlet rakes, struts, sandwich pack and sandwich pack rakes were developed from drawings provided by Honeywell. To determine the surface roughness of the remaining inlet components that are included in the plenum model (the plenum top half, bottom half, and baffle), a profilometer was employed. A total of five surface roughness measurements were conducted in different locations on the surface of each component. The average of these indicated roughness values were specified on the respective surfaces within CFX Pre. The walls of inlet and outlet extension domains were assigned as smooth walls. For the section of the outlet extension that contained flow path geometry downstream of the AIP, the hub and shroud roughnesses were applied. All walls were assumed to be adiabatic.

### 2.2.3 Plenum Model Mesh

All domains of the plenum model were meshed using ANSYS Meshing and a 3D tetrahedral mesh structure. Prismatic inflation layers were applied on all surfaces except for interfaces, inlets, and outlets to capture boundary layer behavior. This type of mesh has been used in investigations of APU inlets by Bouldin et al. (2011) and Lavan Kumar et al. (2013) with both models delivering accurate results with respect to experiment. The maximum element size of the trailing edges of the sandwich pack rakes, inlet rakes, and struts were reduced from the universal mesh maxima by a factor of 3.33. Furthermore, the largest allowable element size of all edges was refined by a factor of 5 from the maximum. This was to reduce the expansion ratio from the inflation layer to the mean flow path and to refine areas that may induce separation within the plenum. The defeature size was assigned as 500 times smaller than the maximum element size. The curvature normal angle for all domains was assigned as  $10^\circ$ , and the minimum local curvature value was a factor of 50 times less compared to the universal maximum. The resulting mesh for the plenum top half, bottom half with the  $0^\circ$  baffle installed, and outlet extension is shown in Figure 2.9.

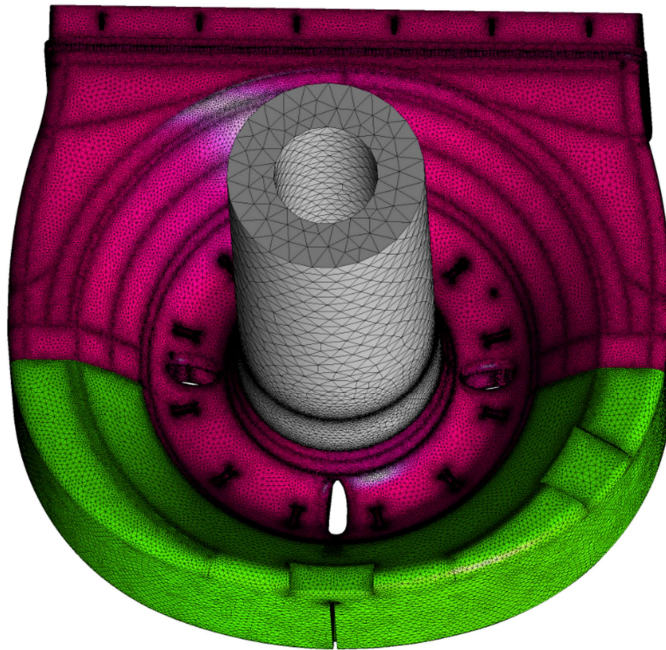


Figure 2.9. Plenum model mesh,  $0^\circ$  baffle configuration ALF



## 2.2.4 Plenum Model Grid Convergence Study

A grid convergence study was conducted to verify the veracity of the mesh generated for analysis. The case used for validation was the nominal 0° baffle, no blocker plate case at 100%  $N_c$  in choke. This is the maximum mass flow rate for the inlet system in the nominal configuration. Two further models were created according to the method described in section 2.2.3. One was a finer mesh and is designated case 1, and the other a coarser mesh labelled case 3, with the original mesh being case 2. To refine or coarsen the number of elements of the mesh, the value of the universal element size was increased by a factor of 2 for case 3 and decreased by the same factor for case 1. The number of prismatic inflation layers was increased for case 1 by 50% and decreased by 50% for case 3. The first layer height was also changed for the grid convergence analysis such that the first layer height of the case 3 mesh was twice that of case 2 and the value being halved for case 1. A summary of the generated mesh and the element count of each domain is provided in Table 2.1.

Table 2.1. Plenum model mesh statistics

	Case 1	Case 2	Case 3
<b>Plenum Top Half Elements</b>	32,714,578	17,765,619	11,703,614
<b>0° Baffle Bottom Half Elements</b>	3,615,782	1,158,208	642,316
<b>Outlet Extension Elements</b>	1,005,229	436,793	192,224
<b>Plenum Model Elements</b>	<b>37,335,589</b>	<b>19,360,620</b>	<b>12,266,705</b>
<b>Normalized Grid Spacing</b>	<b>1</b>	<b>1.93</b>	<b>2.98</b>

With the grid convergence cases established, the method to determine convergence presented by Celik et al. (2008) was used. The parameters chosen for analysis were the inlet performance parameters of TPR and  $\eta$ . Cases 1 through 3 were simulated in CFX using the same operating point, and the data were extracted using CFX Post once the solution achieved convergence. These points are plotted in Figure 2.10 along with the Richardson extrapolation that was calculated according to Celik et al. (2008). The value established from the Richardson extrapolation is the estimated final value of the studied parameter if the element size was refined to an infinitesimal value.

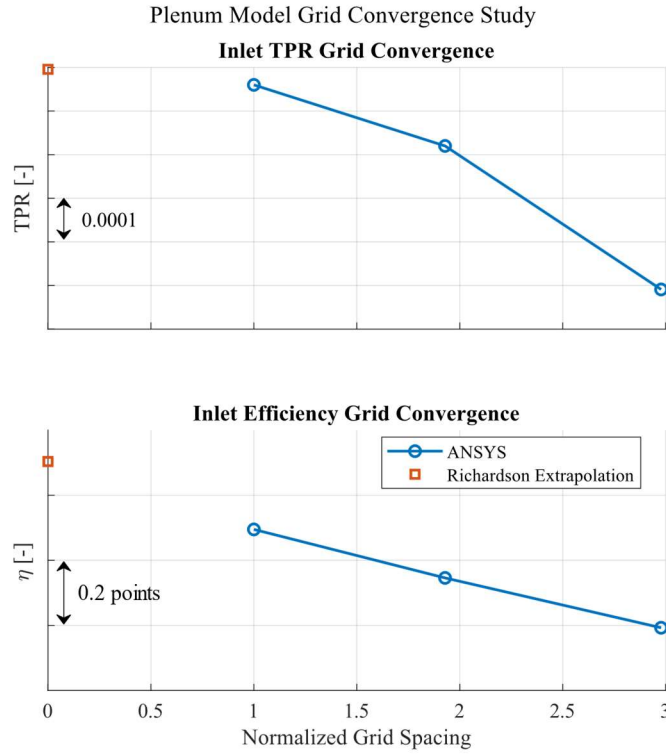


Figure 2.10. Plenum model grid convergence study plots of TPR and  $\eta$

The TPR deviation between the Richardson extrapolation and case 2 was less than 0.0002 and less than 0.35 points in  $\eta$ . This indicates that the mesh from case 2 presents more than sufficient accuracy for the purposes of this effort. Furthermore, the use of case 2 was justified comparing the error between case 2 and the extrapolated value and the error between cases 2 and 1. These values are calculated using the algorithm outlined in Celik et al. (2008) and are provided in Table 2.2. Along with the error calculations, the grid convergence index (GCI) values between cases 3 and 2 ( $GCI^{32}$ ), and cases 2 and 1 ( $GCI^{21}$ ) are provided. The error in TPR is less than two hundredths of a percent for case two with respect to both case 1 and the extrapolated value. This is a miniscule difference and  $GCI^{32}$  is also minute. Hence for the plenum model case, the driving parameter for consideration of mesh size is  $\eta$ . For  $\eta$   $GCI^{32}$  is approximately double the value of  $GCI^{21}$ , indicating that the grid considered in case 3 is too coarse to yield accurate efficiency values. Furthermore, the difference between case 3 and the extrapolated  $\eta$  is more than 0.5 points and, thus, case 3 was not considered for further study. The reduction in error of about 0.15 points between cases 1 and 2 did not outweigh the increase in computation time between case 1 and case 2. Moreover, the

difference in error between 0.37% and 0.22% is not large. Therefore, for this effort, an error of less than 0.4% in  $\eta$  was considered acceptable, and case 2 was selected.

Table 2.2. Plenum model GCS metrics

<b>Metric</b>	<b>Inlet TPR</b>	<b>Inlet Efficiency</b>
$e_a^{21}$	0.014%	0.155%
$e_{ext}^{21}$	0.018%	0.372%
$GCI^{21}$	0.005%	0.272%
$GCI^{32}$	0.022%	0.467%

Local grid convergence was also indicated by Celik et al. (2008) as important for consideration when there is not oscillatory convergence at the location being considered. Oscillatory convergence is observed when the value of a parameter from case 2 does not reside in between the values from cases 1 and 3. This is not an uncommon phenomenon, particularly for an unstructured mesh. For this model, local convergence was assessed at the AIP. Data along the same traverse path, as conducted during a rotatable rake survey, were extracted from the different results files from the cases for consideration. Oscillatory convergence was observed at the AIP for all four parameters of interest: total pressure, static pressure, Mach number and swirl. A plot of total pressure profiles at the AIP for the different GCS cases is provided in Figure 2.11 showing oscillatory convergence at numerous circumferential locations along each of the radial element locations. Therefore, local grid convergence was not considered a reliable metric for the plenum model.

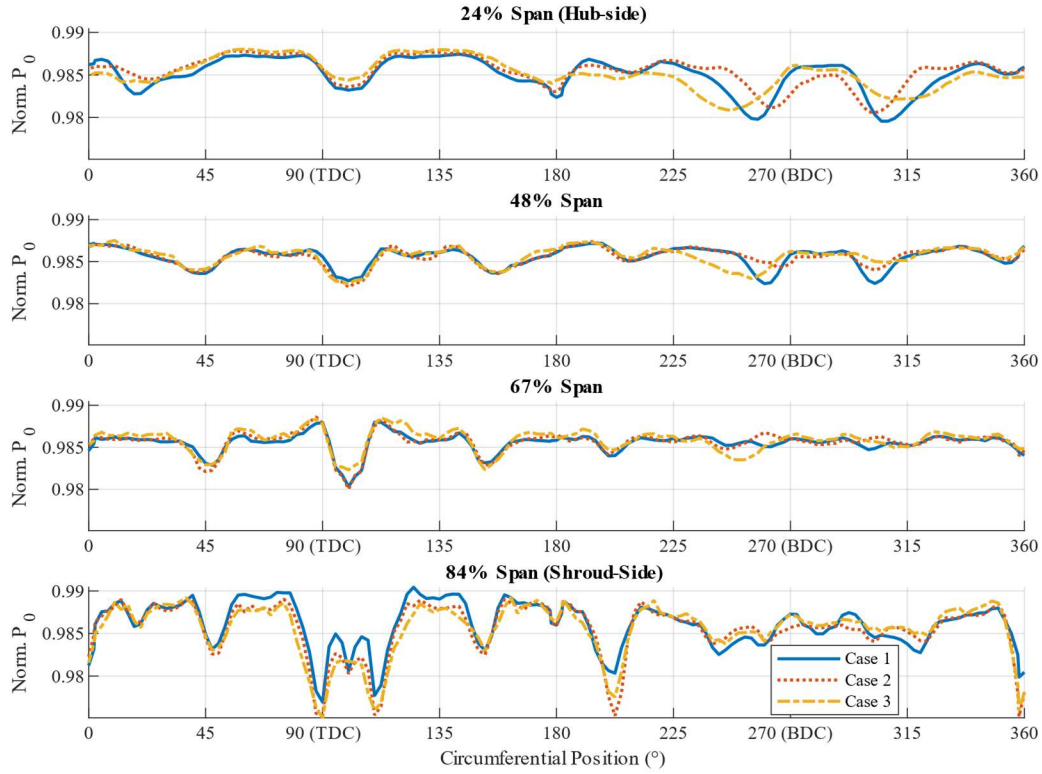


Figure 2.11. Plenum model grid convergence cases normalized total pressure values at AIP

### 2.2.5 Veracity of Plenum Flow Structure

A qualitative and quantitative analysis of the flow structures in the plenum and the annulus is necessary to ensure model fidelity. APU plenum flow structures were thoroughly reviewed in section 1.3.1, and the summary of literature from that section should be compared to the results from case 2 for fidelity. Both the flow within the plenum and at the AIP must match the experimental data and literature review cases previously discussed for this model to be considered accurate.

To analyze the quantitative accuracy of the model, total pressure data were extracted at the four circumferential inlet rakes and compared to experiment. This comparison is provided in Figure 2.12. The 45° and 135° inlet rakes are in the top half of the annulus, and the 255° and 315° rakes reside in the bottom half. The plenum model shows a near uniform total pressure profile in the top half of the annulus. This is attributable to the uniform total pressure profile boundary condition at the SPIP, as flow has not been greatly perturbed upstream of these two rakes. The

total pressure behavior at the upper half rakes is comparable to the experimental values, with the largest deviation being less than 0.5 points of normalized total pressure. The largest deviation of the bottom half rakes is 0.5 points of normalized total pressure. However, the mean value for each rake is within 0.22 points. Considering there is no mixing upstream of the plenum in this CFD model to cause pressure non-uniformities, the quantitative total pressure behavior is remarkably comparable to experiment.

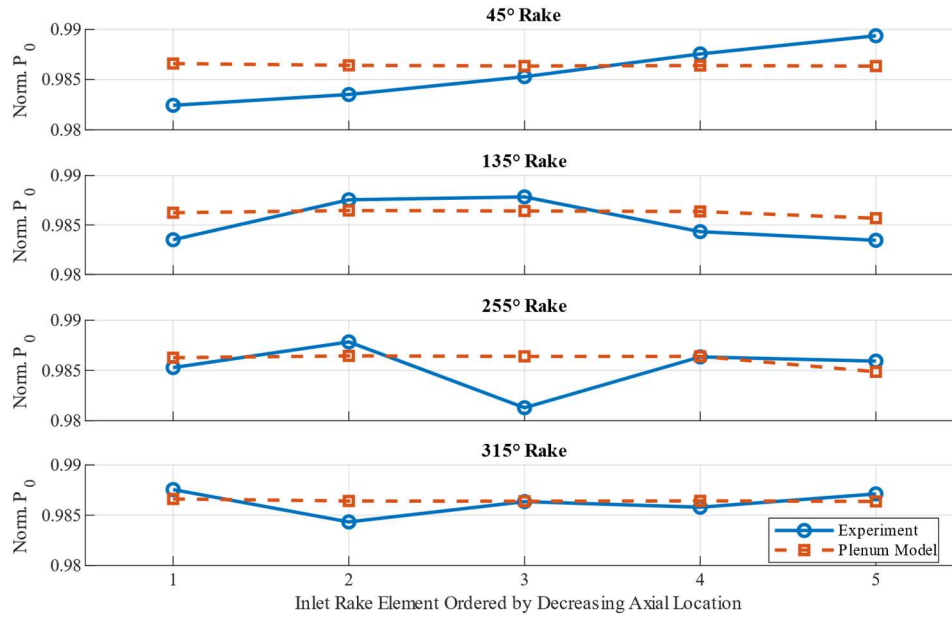


Figure 2.12. Plenum model inlet rake normalized total pressure data compared with experiment

For a qualitative analysis of the flow structures of the plenum model, the flow within the plenum itself and at the AIP is interrogated. Figure 2.13 shows the Mach number of the flow with surface streamlines at the mid span of the plenum from the computational simulation. The flow structure matches those previously documented in literature. The high momentum region of flow is located at TDC and the lower momentum region along the outer walls of the plenum and at BDC. Furthermore, this indicates that the plenum used in this effort is oversized, as marked by the trapped recirculation zone on either side of the baffle at BDC. This behavior should be expected for all other data points that are being replicated in this investigation, as this simulation was conducted at the highest mass flow rate achieved in the nominal configuration. The flow field is

also perturbed significantly by the presence of struts and inlet rakes. This is a topic that will be discussed in detail in chapter 4.

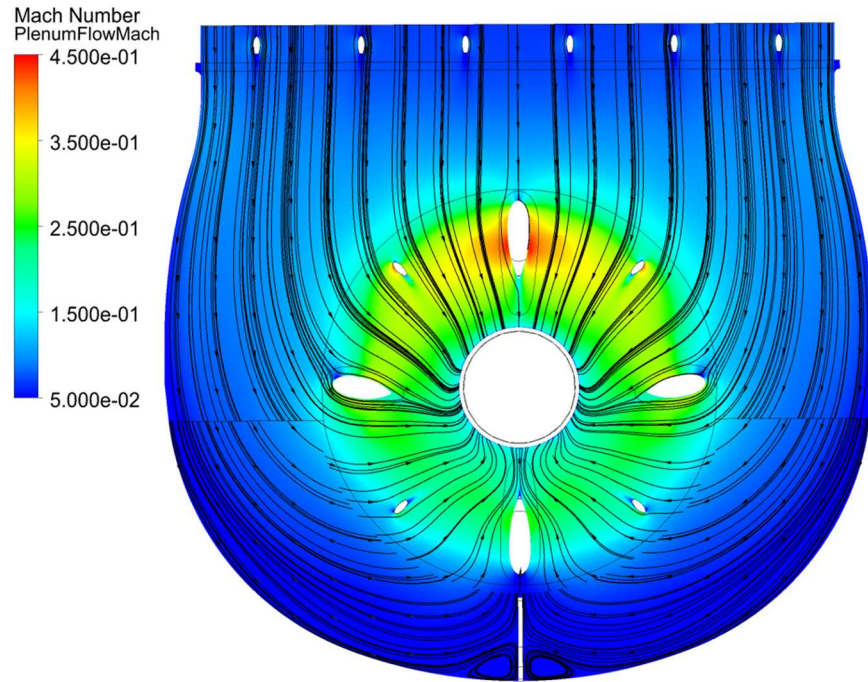


Figure 2.13. Plenum model case 2 simulation Mach number and flow distribution in the mid plane of the plenum, FLA orientation

The expected flow at the AIP for the inlet configuration analyzed for the GCS is a twin swirl pattern due to the  $0^\circ$  baffle being installed. Figure 2.14 shows the flow structure predicted by CFD at the AIP. The twin swirl pattern is evident in the behavior of the surface streamlines in the figure as the streamlines show symmetry. Furthermore, the Mach number contour displayed behind the streamlines also agrees with literature. The high momentum region is located around TDC but has spread circumferentially, and the lowest momentum flow is directly downstream of the baffle. The plenum model predicts the ingestion of the recirculation zones about the  $0^\circ$  baffle creating a dead zone located  $\pm 20^\circ$  circumferentially about BDC, as indicated by the surface streamlines.

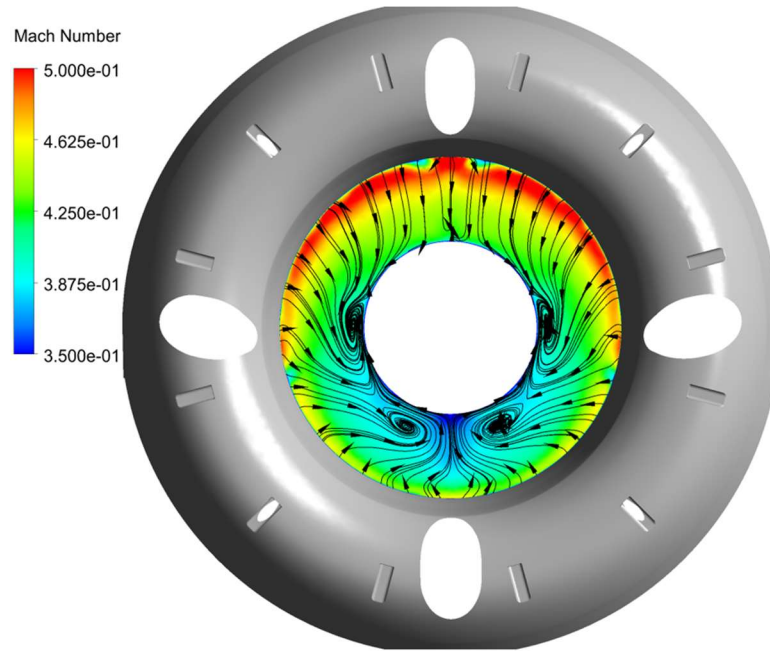


Figure 2.14. Plenum model case 2 simulation Mach number and 2D streamlines at the AIP, FLA orientation

## 2.3 Development of Full-Inlet Computational Model

For the purposes of validating the reduced model, a full-inlet model was generated and analyzed. This model encompasses the full geometry of the SSCC APU inlet as outlined in section 2.1.2 APU Inlet Configurations.

### 2.3.1 Full-Inlet Model Domains and Interfaces

The full-inlet model mated the plenum model with two additional domains: a spreader-elbow duct, and the bellmouth as illustrated in Figure 2.15. The bellmouth incorporated an extension to allow flow to be drawn into the APU inlet. Thirty percent of the axial length of the transition duct was also included in this domain. The rest of the transition duct geometry was incorporated in the spreader-elbow duct and was meshed as one domain to reduce the number of interfaces used in this model. These domains were split to the bellmouth and spreader-elbow duct topologies. A GGI interface was placed between the exit of the bellmouth domain and the inlet of the spreader-elbow duct domain. A further GGI interface combined the exit of the spreader-elbow with the inlet of the plenum model at the SPIP. To reduce the uncertainty of a GGI interface at this

location due to the inherent difference in node densities between a structured and an unstructured mesh, the element size of the plenum side of this interface was refined by a factor of 2. The significant regions of reverse flow from the elbow into the spreader, as noted by Lou et al. (2015), render the use of a GGI interface between these two geometries untenable due to increased uncertainties from high secondary flow magnitudes. Therefore, to avoid this generation of uncertainty, the spreader and elbow ducts were meshed as one domain.

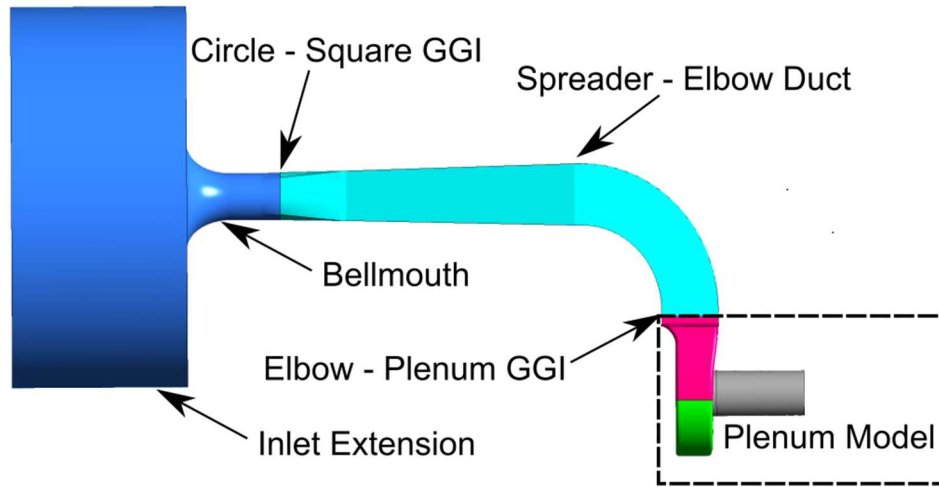


Figure 2.15. Full-Inlet model domains and interfaces

### 2.3.2 Full-Inlet Model Boundary Conditions and Discretization

The common domains between the plenum and full-inlet models were discretized identically. For comparison purposes, the same outlet boundary condition as the plenum model (corrected mass flow rate from experiment) was prescribed at the extension outlet. Furthermore, the same reference conditions of 14.696 psia and 59°F were maintained and the same SST turbulence model was utilized for analysis. The boundary condition at the extension of the bellmouth was assigned as an opening. This allowed flow to be drawn into the bellmouth from all sides as shown in Figure 2.16. The flow distribution into the bellmouth, under this boundary condition, was more physically representative than that of oncoming normal flow, as the wall-side lower momentum flow within the bellmouth is drawn from behind the opening. The total pressure loss due to the inlet FOD screen was calculated using the method outlined by Ishak (2009) and was on the order of 0.003 psia at the highest encountered mass flow rate. This is lower than the



uncertainty value measurable by the DSA 3016 modules and was therefore considered negligible. A turbulence intensity value of 3.29% was assigned to the opening as this was the measured value behind the FOD screen from Lou et al. (2015).

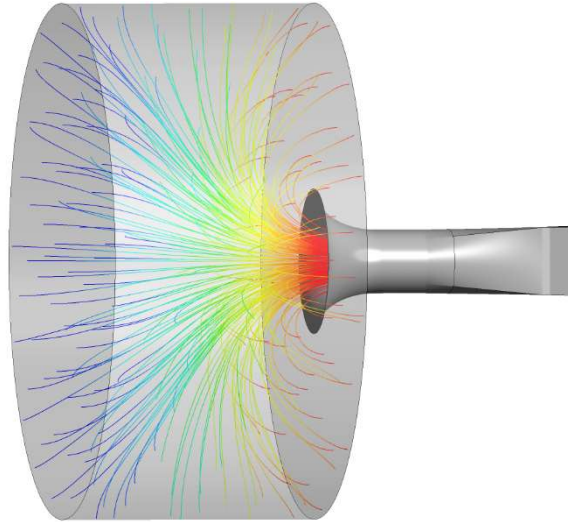


Figure 2.16. Full-Inlet model opening boundary condition with streamlines colored by axial position

Surface roughness values of the spreader-elbow duct, spreader vanes, and bellmouth-transition were determined with a profilometer, and the mean of five roughness indications were assigned to each face. All walls were modelled using an adiabatic assumption.

### 2.3.3 Full-Inlet Model Mesh

The simple circular and rectangular cross sections of the inlet duct geometries are ideal for use of a structured mesh. GridPro was employed to define the topology and to generate the mesh for the two additional full-inlet domains. The geometry was imported into ANSYS SpaceClaim and was meshed as a refined unstructured surface mesh using ANSYS Meshing. It was then exported in the form of an .stl file to be imported into GridPro. The interface location between the two sides of the transition duct was located such that the H-grid geometry began where the square cross section became dominant. This prevented low mesh density in the corners of the transition where separation is anticipated. Inflation layers were applied to surfaces of the duct domains to

match the values used in the GCS of the plenum models to prevent cell density mismatch at the SPIP interface. GridPro does not allow a maximum layer count to be set, but rather a multiple of the number of layers is prescribed. For this reason, the inlet duct layer count multiple was set as the maximum layer count that was assigned to the unstructured meshes. The grid generation routine was conducted until there was no longer a reduction in element skew, warpage, and aspect ratio between iterative loops.

An H-O-H topology was utilized for the spreader-elbow duct. This topology scheme uses a standard H-grid geometry either side of a channel that uses an O-grid structure. The channels were required to use an O-grid to wrap the five spreader vanes, and the leading and trailing edges were constrained to an internal cylindrical surface to define the sharp corners of the vanes. The consequence of this was that the mesh density within the channel was lower than the H-gridded areas of the transition and elbow sections. However, this was considered acceptable for this analysis as the inflation layers applied along the walls and spreader vanes increased the local mesh density along the surfaces where flow separation would occur. The generated mesh for this domain is shown in Figure 2.17.

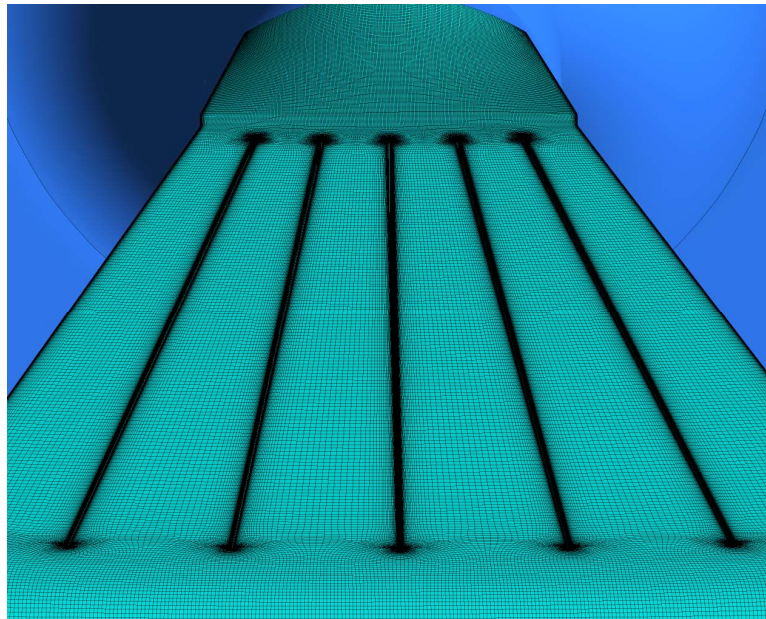


Figure 2.17. Spreader-elbow domain mesh using H-O-H grid topology FLA

The circular bellmouth cross section dictated the use of the O-grid topology. The exterior surface topology was internally wrapped to generate this structure. Mesh density of the inlet extension section was decreased to reduce the node count of the mesh. Exterior surfaces of the transition were split into four to allow for the corners that begin to develop from the circular cross section to be captured. The mesh density at the interface was selected to be comparative to that of the spreader-elbow side to prevent numerical error propagation due to interpolation. Figure 2.18 presents a rendering of the investigated mesh.

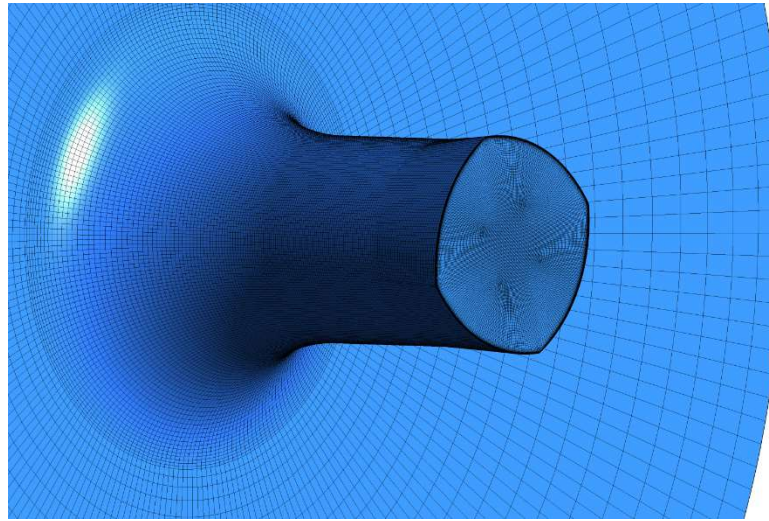


Figure 2.18. Bellmouth and inlet extension domain mesh using O-grid topology

#### **2.3.4 Full-Inlet Model Grid Convergence Study**

As with the plenum model, a grid convergence study was conducted to verify the validity of the full-inlet model. This analysis utilized the mesh from the plenum GCS cases 1,2, and 3 with the SPIP interface element size being refined by a factor of two. These meshes were matched with inlet duct components of comparable density and yielded element counts represented in Table 2.3.

Table 2.3. Full-Inlet model mesh statistics

	Case 1	Case 2	Case 3
<b>Refined Plenum Model Elements</b>	39,062,493	19,761,807	12,600,994
<b>Spreader-Elbow Elements</b>	45,599,232	24,470,784	7,426,560
<b>Bellmouth Elements</b>	5,808,128	3,832,192	1,448,000
<b>Full-Inlet Model Elements</b>	<b>90,469,853</b>	<b>48,064,783</b>	<b>21,475,554</b>
<b>Normalized Grid Spacing</b>	<b>1</b>	<b>1.88</b>	<b>4.21</b>

Using these GCS cases, a further grid convergence study was conducted per the outline provided by Celik et al. (2008). Once again, TPR and  $\eta$  were considered as the metrics to analyze grid convergence. Each of the cases were run to convergence, and these performance metrics were extracted using CFX Post. The simulations dispensed the values of TPR and  $\eta$  as shown below in Figure 2.19.

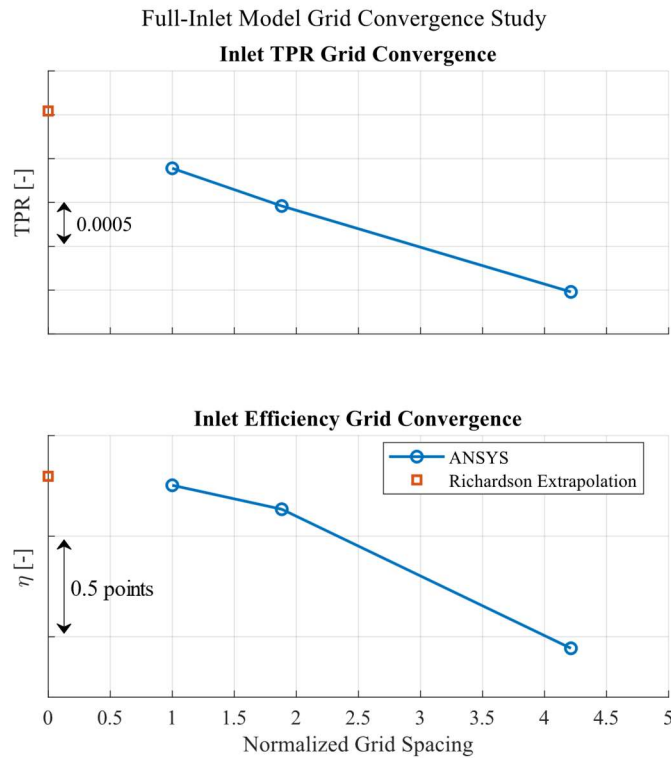


Figure 2.19. Full-Inlet model grid convergence study plots

In contrast to the plenum model, the trend of full-inlet model shows that  $\eta$  converged towards the Richardson extrapolation value at a higher order than TPR. However, both TPR and  $\eta$  showed more uncertainty in the full-inlet models than the plenum models, as represented by the scales being significantly larger in this case. Both performance metrics indicated that case 3 suffered from significant error with respect to cases 2 and 1, rendering it unsuitable for use. Further analysis of the GCS metrics was employed to justify use of case 2 for analysis. Table 2.4 includes the error and grid convergence indices that were calculated according to Celik et al. (2008).

Table 2.4. Full-Inlet GCS metrics

<b>Metric</b>	<b>Inlet TPR</b>	<b>Inlet Efficiency</b>
$e_a^{21}$	0.044%	0.135%
$e_{ext}^{21}$	0.110%	0.185%
$GCI^{21}$	0.083%	0.063%
$GCI^{32}$	0.138%	0.232%

The reduction of  $GCI^{21}$  from  $GCI^{32}$  is a further indication that grid 3 is unsuitable for use, as case 2 is almost two times closer to converging to the extrapolation value in TPR and almost 4 times in  $\eta$ . The results with respect to  $\eta$  clearly indicate that case 1 provides a minuscule reduction in the error of the solution with respect to the extrapolated value. Furthermore, the difference in error of TPR from the extrapolation and cases 1 and 2 is less than 0.07 points. Thus, case 2 was deemed to provide sufficient accuracy for the purposes of this investigation.

Local grid convergence was analyzed at the AIP for this model. As in the case with the plenum model, the grid showed oscillatory convergence at this location as shown in Figure 2.20. Therefore, local convergence was not considered a valuable metric for this model.

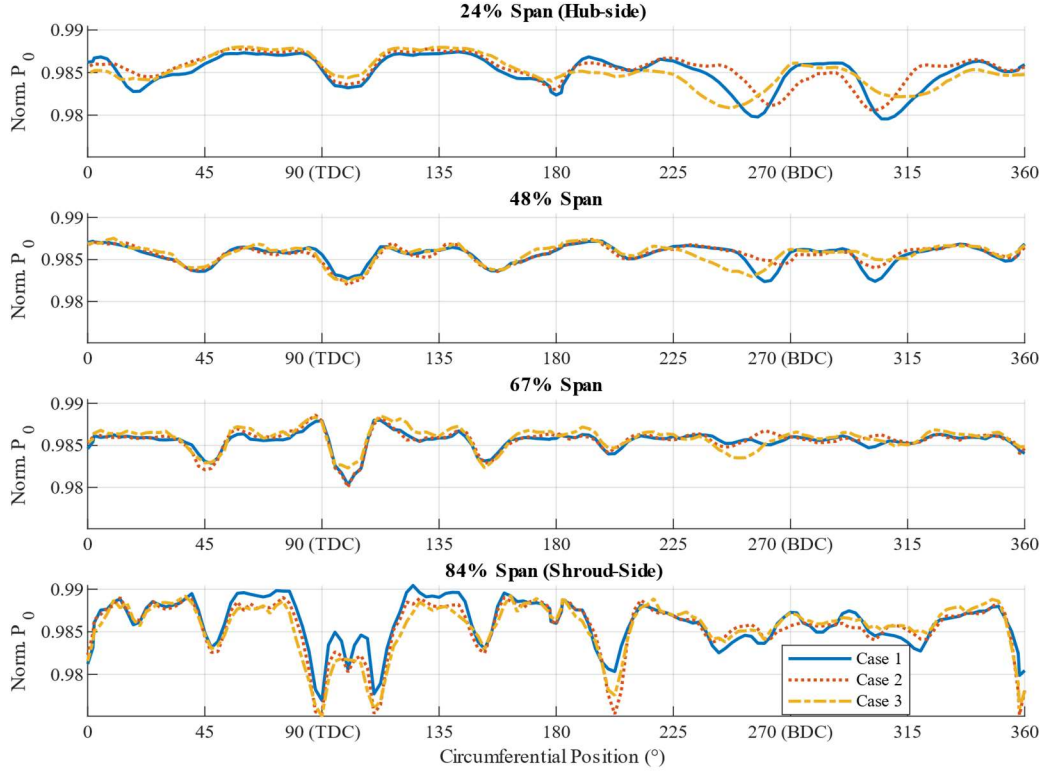


Figure 2.20. Full-Inlet model grid convergence cases normalized total pressure values at AIP

### 2.3.5 Veracity of Circle-to-Square Flow Structure

As discussed in chapter 1, the flow through a circular-to-rectangle cross section duct is expected to have low momentum zones develop in the corners. This region grows in both magnitude and size generating a low axial velocity region at the exit of the duct with respect to the bulk flow. A total of three contours of normalized axial velocity at the entrance, mid-passage, and exit of the transition duct from the simulation using the case 2 grid are provided in Figure 2.21. The SSCC APU inlet does not have instrumentation embedded within the transition duct and, therefore, expected flow structures from literature must be used to verify the veracity of flow structures indicated by the model. The indication from these planes is that the model exhibits comparable axial velocity behavior as the experiments conducted by Davis and Gessner (1992) and Pao et al. (1994) on similar duct geometries. The significant disparity between literature and the model is that the low momentum corner regions do not merge to form larger regions along the outer walls. The most probable cause for this is that the transition ducts examined by both Davis



and Gessner (1992) and Pao et al. (1994) were of a rectangular cross section instead of a square, as used in the SSCC inlet assembly. The shorter side of the rectangular section tended towards a merging of these lower mass flow regions whereas the longer sides did not. Therefore, the difference can most likely be contributed to minor discrepancies in the exit cross sections.

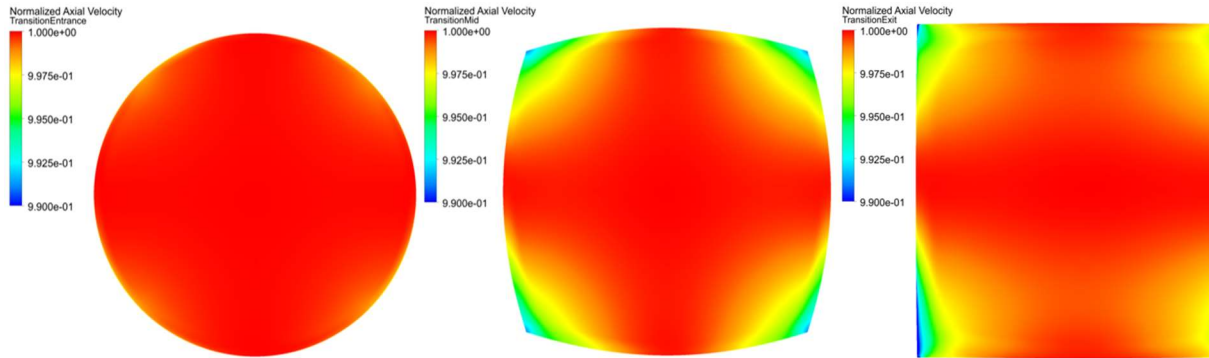


Figure 2.21. Full-Inlet model case 2 transition duct axial velocity profile

### 2.3.6 Veracity of Elbow Flow Structure

Though there is also no instrumentation within the APU inlet elbow of the SSCC, the sandwich pack rakes are located at the exit of the duct, which provide 18 total pressure readings. The total pressures at the locations of the sandwich pack rakes were extracted from the CFD model using CFX Post and are presented as a contour alongside the experiment data in Figure 2.22. The full-inlet model contour shows maximum deviation from experiment on the order of 0.04 points of normalized total pressure. This indicates that the model captures momentum losses through the elbow accurately. One notable difference is that the CFD data are predominantly symmetric about the centerline, whereas the experiment is not. This is most likely due to a slight installation misalignment of the elbow duct or asymmetries of the components from manufacturing.

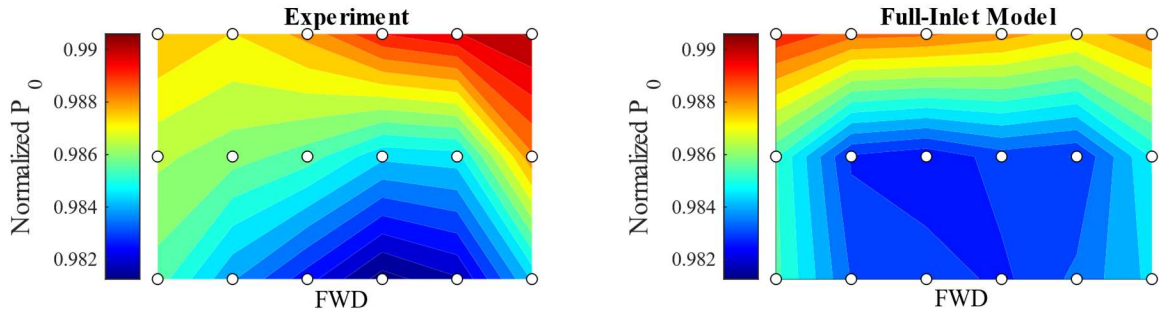


Figure 2.22. Sandwich pack total pressure from experiment and full-inlet model case 2, viewed top down

In addition to the sandwich pack total pressures, a comprehensive LDV study of the flow through this elbow, when used in conjunction with the upstream spreader and transition ducts, was conducted by Lou et al. (2015). In this effort, multiple spanwise planes were sampled and the velocity profiles as well as streamlines were extracted. For the purposes of verifying the flow structure within the elbow produced by the computational model, three of these planes were utilized for comparison. The planes were located at 5%, 21.5% and 42% of the passage span, as depicted in Figure 2.23.

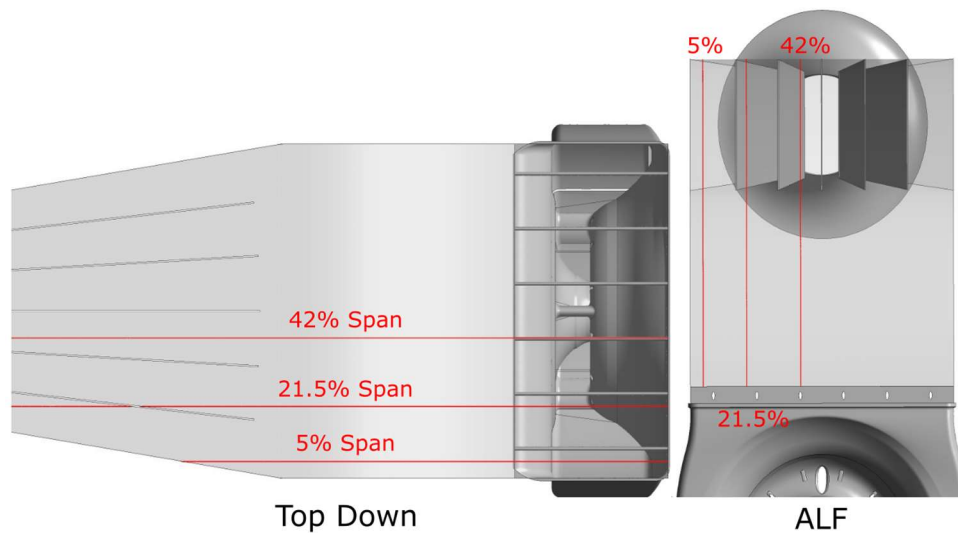


Figure 2.23. LDV planes replicated in Full-Inlet model for comparison

One notable distinction between this investigation and past LDV work, however, is that the elbow in the LDV investigation exhausted into a tangential duct. The SSCC APU inlet is



connected to a radial-to-axial inlet, which includes flow contraction downstream of the SPIP. The severity of the geometric area reduction is represented in Figure 2.23. At 5% span, the flow area is not affected by a downstream contraction. However, both the 21.5% and 42% plane are affected by flow area reductions due to the radial bend of the plenum. This causes a distinction between the LDV and CFD results, as shown in the comparison in Figure 2.24.

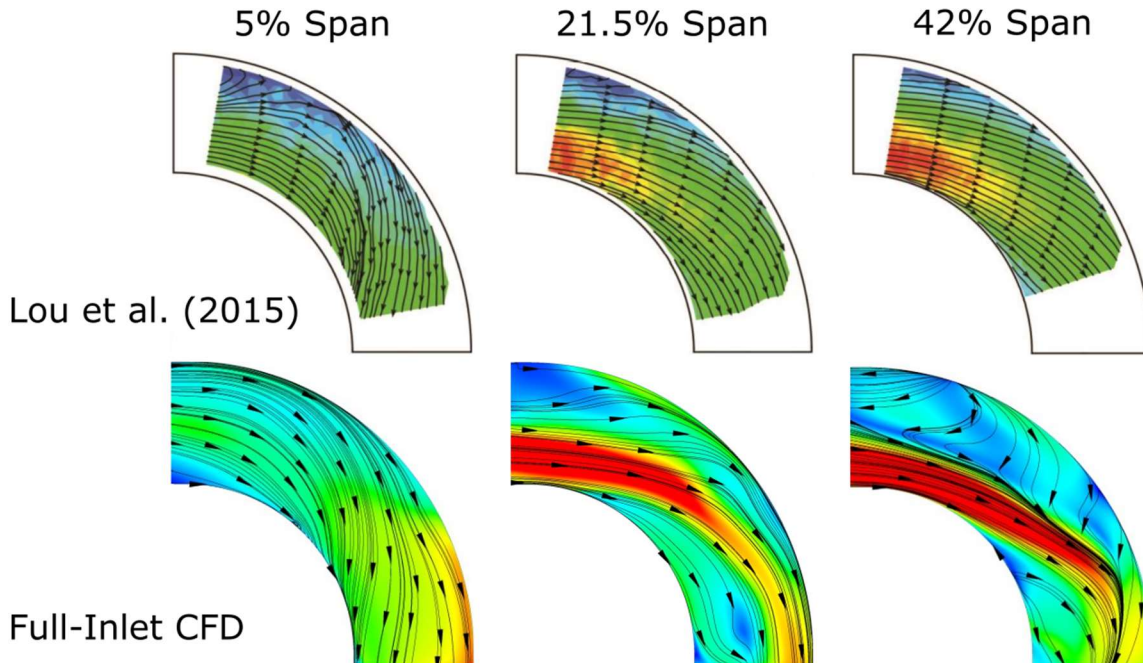


Figure 2.24. Comparison of Full-Inlet CFD elbow flow velocity and streamlines with LDV data from Lou et al. (2015)

For all the spanwise planes, the CFD and LDV show similar streamline behavior and velocity magnitudes along the inner wall of the bend. The small region of low momentum at 42% span about  $60^\circ$  through the bend is represented in both LDV and CFD, despite the different downstream geometries between the two cases. In the 5% plane, halfway through the bend, the flow begins to bias towards the inner wall for both CFD and LDV, which is in agreeance with Sudo et al. (2001). The presence of the high momentum jet is represented in both experiment and CFD sandwich pack total pressures.

The major disparities between the two are identified along the outer wall. LDV showed that the recirculation zone at the top of the passage at the entrance to the bend has its highest

magnitude at the 5% span plane and diminishes in both size and magnitude further into the passage. However, CFD indicates the opposite behavior, which is indicative of the effects of the downstream plenum. The flow contraction downstream of the bend is strongest at the mid passage of the elbow. This leads to jet formation, which increases in magnitude towards the center of the passage. This is observable in both the 21.5% and 42% planes. LDV data indicate that the jet flow leaving the spreader is diffused before exiting the bend. However, the CFD cases with the plenum installed indicate that this structure does not begin to break down until about 80° through the bend. The high total pressure zone on the outer wall at the exit of the bend is further evidence that this structure progresses into the plenum. For the CFD cases, the jet is what generates the flow recirculation zone as the adverse pressure gradient along the outer wall redirects the incoming flow back towards the spreader vanes, generating a region of blockage. This upper wall region of separated flow dictates the location of the jet until about 45° through the passage where the jet is then deflected from the inner wall to the outer wall by a low momentum region along the inner wall at approximately 60°. Both LDV and CFD indicate the same location and magnitude of the inner wall separation in the mid span planes.

These major discrepancies are fundamentally caused by a difference in configuration, which is supported by the agreement between sandwich pack total pressure from experiment and CFD. The CFD plane that has the closest resemblance to the LDV data is the 5% plane, which experiences the least downstream contraction and therefore is the least perturbed by this effect. This plane is the most representative of a similar flow situation as investigated by Lou et al. (2015). The lack of the recirculation zone in the CFD simulation results at this location, is attributed to flow redistribution due to the mid-passage jet structure. Considering this is the only discrepancy between LDV and CFD at the 5% span plane, and the sandwich pack total pressure data are remarkably similar, the model provides accurate flow structures within the 90° bend.

## **2.4 Computational Replication of Three-Hole Probe Traverse**

Another set of models were developed that included three-hole probes at the AIP in multiple locations to simulate a rotatable rake traverse. The purpose of this model was to validate experimental three-hole probe results within CFD simulations. For these models, the outlet extension domain was merged with the plenum top half domain to avoid uncertainty induced by the pressure gradient transmitted by the rotatable rakes. Moreover, the density of the mesh around the

rakes is greater than that of the mean flow path, which would further add to the uncertainty generated by the GGI due to interpolation onto a higher density mesh. The same rake geometry setup as outlined in section 2.1.3 was utilized. However, both Kulite rakes were replaced with three-hole probe rakes for each configuration to reduce the quantity of simulations. A total of five cases were simulated accounting for a total of 20 circumferential data locations. The rakes are shown at the circumferential locations within the annulus in Figure 2.25.

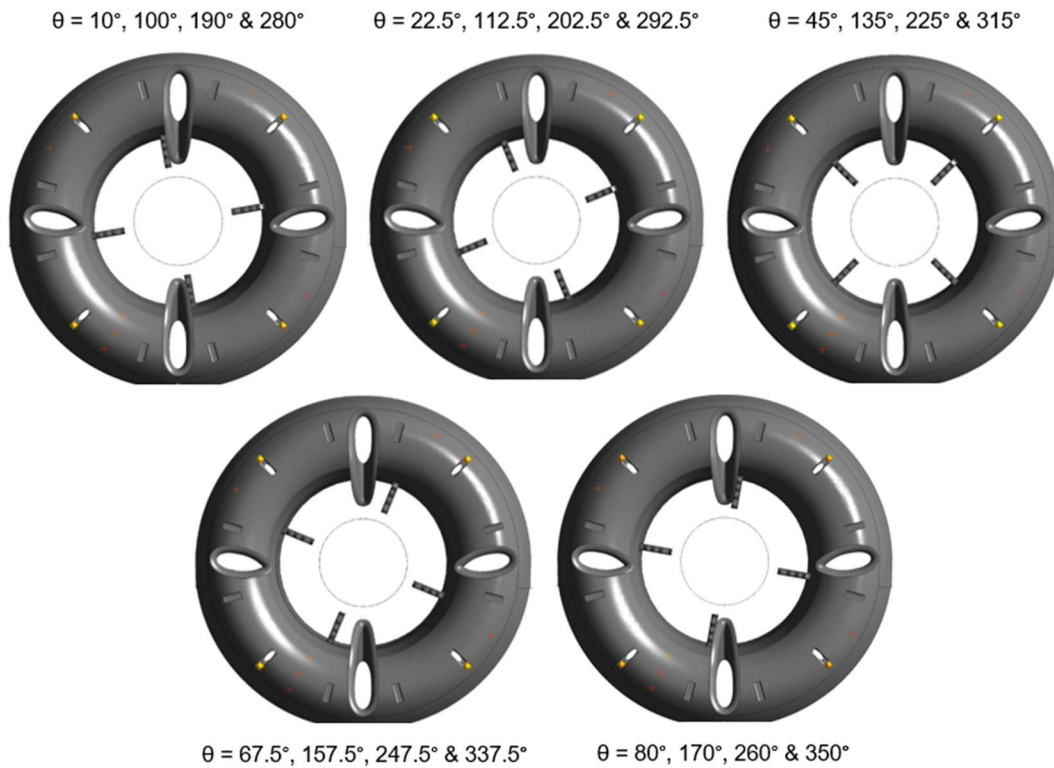


Figure 2.25. Three-hole probe computation models' rotatable rake traverse location, FLA orientation

The circumferential values of 22.5° and 67.5° and the traverse points associated with these locations were selected to capture regions of flow that are unperturbed by struts and rakes. The  $\theta = 45^\circ$  case was selected to capture the inlet rake wakes, and the 10° and 80° circumferential locations were specified to resolve the total pressure deficit within the wakes of the struts around the annulus.

Simulations of multi-hole probes in CFD have been conducted in the literature. De Guzman et al. (1994) used a structured mesh to determine the flow features across a four-hole probe. In this investigation, yaw angle and pitch angle were varied, and the performance of the probe from CFD was compared to experiment. The pressure values indicated by the CFD model were comparable to those from experiment. Furthermore, they conducted oil film surface flow visualization on the probe, which matched streamline trajectories from their CFD simulations. Argüelles Díaz et al. (2011) conducted a similar investigation on a trapezoidal three-hole probe in incompressible flow with head geometry very similar to probes used within the SSCC rotatable rake. They used an unstructured mesh and considered multiple two equation turbulence models as well as the Spalart-Allmaras one equation model and compared their results to experiment. They concluded that the lower fidelity turbulence models produced the same probe calibration data as the experiment and that the only disparities between the simulation and experiment came in regions of high flow separation. It was suggested that refinement of the mesh along the regions of separation would reduce these disparities. The authors indicated that the method of using a one or two equation turbulence model along with an unstructured mesh for a three-hole trapezoidal probe is effective, and therefore, this method was included in the CFD modelling of the SSCC rotatable rake three-hole probes.

Considering the findings of Argüelles Díaz et al. (2011), an unstructured mesh was generated for each of the rotatable rake traverse locations indicated in Figure 2.25 to analyze three-hole probe efficacy. The mesh utilized increased density at the edges of the probe faces to better capture flow separation. The probe faces themselves were also refined. The element size for both the indicated edges and faces was reduced by a factor of 5 from case 2 of the plenum model. The pressure taps, where flow stagnates, were also included in the mesh. This was to allow numerical diffusion within the probe to be able to take a static pressure reading from the back face of the tap. The same inflation layers, as applied in the previous inlet plenum top half mesh, were applied to all faces of the rake and instrumentation. The mesh that was generated for a rake is shown in Figure 2.26 alongside a rendering of the rake.

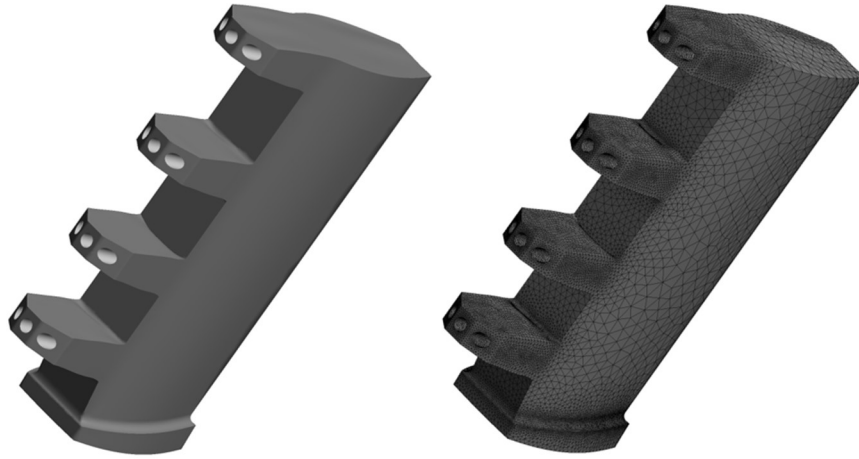


Figure 2.26. Three-hole probe rendering and mesh

These meshes were utilized in both the plenum and full-inlet models to compare three-hole probes performance in different APU inlet configurations. The SST turbulence model was also used for these simulations as this model incorporates two different two equation turbulence models with a blending factor. The work conducted by Argüelles Díaz et al. (2011) indicated that two equation models should provide sufficient accuracy for the simulations being conducted in this effort.

### 3. DATA PROCESSING

The purpose of this chapter is to provide insight as to how the experimental three-hole probe data were processed, how expressions to determine distortion descriptors were developed, and how the computational model data were extracted from ANSYS CFX Post and post-processed.

#### 3.1 Experiment Three-Hole Probe Rotatable Rake Data Processing

The versatility of three-hole probes is their ability to generate multiple parameters from three pressure readings. Static pressure readings from three-hole probes, obtained as outlined previously, are used to create static pressure, Mach number, total pressure, and swirl values at each point in a traverse. This allows the production of a high-density mesh of data to define the flow characteristics at the AIP. The pressure measurements are taken from the probe's left, center, and right pressure taps, as depicted in Figure 3.1.

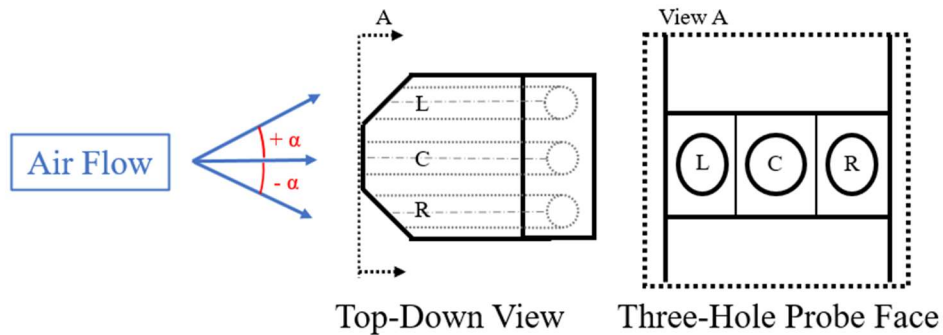


Figure 3.1. Visual of three-hole probe

Three-hole probes that are used for turbomachinery applications generally require that the probes be used in a non-nulling mode as the direction of the flow is not always known. To operate in a nulling mode, the center hole must first be oriented normal to the flow to obtain a null point before sampling. This operation of the probe is untenable for testing of compression systems. Non-nulling operation of multi-hole probes is outlined by Treaster and Yocum (1978). Their methodology produces Mach number, total pressure, static pressure, and yaw values from the differential pressures of multi-hole probes. This method has been adapted for the purposes of this

effort. To operate in non-nulling mode, the probes being used must be calibrated by varying Mach number and yaw angle and taking pressure measurements from the three taps and a pitot static reading away from the probe itself. These five pressure readings allow the coefficients of: yaw due to pressure differential ( $C_{YPD}$ ), static pressure corrected for yaw ( $C_{PSY}$ ), ram pressure corrected for yaw ( $C_{RPY}$ ), and the nulling coefficient ( $C_{null}$ ), to be determined at specific Mach number and yaw angle conditions. These coefficients are determined using equations (3.1) to (3.4):

$$C_{YPD} = \frac{P_R - P_L}{P_C - 0.5(P_R + P_L)}, \quad (3.1)$$

$$C_{PSY} = \frac{P_R - P_L}{P_C - P_L}, \quad (3.2)$$

$$C_{RPY} = \frac{P_0 - P_C}{P_C}, \text{ and} \quad (3.3)$$

$$C_{null} = \frac{P_L - P_S}{P_C - P_S}. \quad (3.4)$$

The three-hole trapezoidal probes used in this experiment were calibrated by Honeywell Aerospace. An example of one of these calibrations is presented in Figure 3.2.

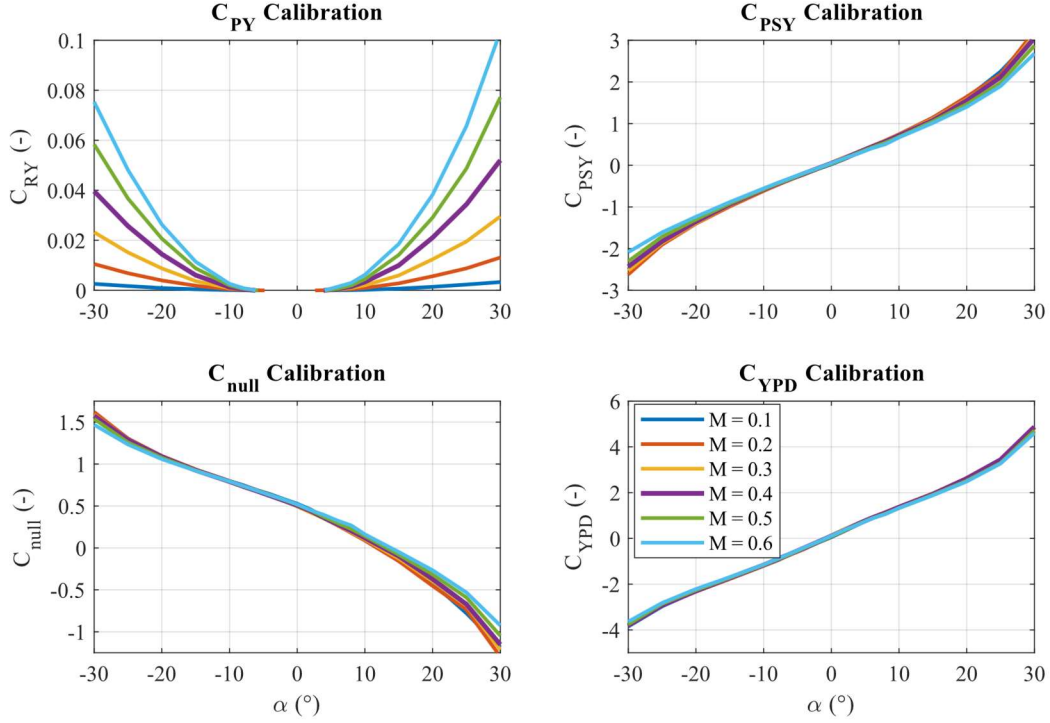


Figure 3.2. Example calibration for a three-hole probe used in experiment

These calibrations were used to solve for static pressure, total pressure, and swirl iteratively varying Mach number. First, an initial guess Mach number was established. Then,  $C_{YPD}$  was readily calculated from the pressure readings from the probe with equation (3.1), thus providing the yaw angle encountered by the probe using the calibration curve for the initial Mach number. From the yaw angle, both  $C_{PSY}$  and  $C_{RPY}$  were determined. The static pressure was solved for by using  $C_{PSY}$  and the three indicated probe pressures using equation (3.2). Similarly, total pressure was determined using equation (3.3) as  $C_{RPY}$  and  $P_C$  were known. The total pressure and static pressure were used along with the ratio of specific heats,  $\gamma$ , to determine the Mach number using equation (3.5):

$$P_0 = P_s \left( 1 + \frac{\gamma - 1}{2} M^2 \right)^{\frac{\gamma}{\gamma - 1}}. \quad (3.5)$$

REFPROP was used to determine  $\gamma$  for air with values of humidity, ambient pressure, and ambient temperature at the inlet to the bellmouth used as inputs. The iterative Mach number was then updated with the calculated Mach number, and the process was repeated. For Mach numbers



that did not fall on a calibration value, the values of  $C_{PSY}$ ,  $C_{RPY}$ , and  $C_{null}$  were linearly interpolated. Once the iteration process converges to a solution,  $C_{null}$  was determined using equation (3.4).

### 3.2 Distortion Descriptors

Testing campaigns to understand a compression system's reaction to different inlet distortions generate hundreds of data points and corresponding inlet contours. Inlet contours are difficult to compare quantitatively at a large volume. Distortion descriptors, also known as distortion indices, are powerful numerical representations of AIP data that allow swift comparisons of inlet flow structures and were used for this purpose in this effort. Different indices are developed to express the total pressure deficits and swirl behavior in the inlet under different conditions. They have been standardized by SAE International (AIR5686, 2017; ARP1420C, 2017; AIR1419C, 2017) to allow for a common understanding of distortion parameters at the AIP.

For all distortion types, circumferential data are acquired along a radial rake instrumentation ring from rake elements at the same radial location. Circumferential intensities and MPRs are developed for each radial ring to express the severity of the distortion and how many areas experience distortion. Radial data are also taken along elements located on the same circumferential ring. Radial intensity information is developed from these readings for pressure distortion but not for swirl, as the radial component of swirl is often neglected due to its lack of influence on compressor performance. The analytical development of these intensities and MPR values is different depending on the type of distortion. Thus, different recommended practices have been adopted for each type of distortion.

Extent,  $\theta$ , is a parameter shared by all circumferential distortion types and is defined by equation (3.6). Extents are the circumferential locations where the total pressure is below the ring average or where swirl is positive or negative. Depending on the MPR of the distribution along the ring, there can be multiple extents, which will be later clarified by example distributions for pressure and swirl distortions. The added complexity from MPRs is represented in equation (3.6) where 'k' represents the number of the extent along the ring, and 'i' represents the number of the  $i^{\text{th}}$  ring of the rake elements. A positive superscript indicates an extent of co-swirl or region of total pressure above the ring average, and the negative superscript indicates an area of counter-swirl or a total pressure deficit:

$$\theta_{i,k}^+ = (\theta_{i,2}^+ - \theta_{i,1}^+)_k \text{ and } \theta_{i,k}^- = (\theta_{i,2}^- - \theta_{i,1}^-)_k. \quad (3.6)$$

### 3.2.1 Pressure Distortion Descriptors

Standards for pressure distortion indices are outlined by SAE International in ARP1420C (2017) and AIR1419C (2017) to characterize the circumferential and radial total pressure deficits occurring at the AIP. An example of a one-per-rev and a multiple-per-rev total pressure distribution are provided in Figure 3.3 for reference. The extents with pressure deficits are colored grey, and the positive and negative extents are labelled. The average pressure deficit in each of the total pressure areas below the average are also identified. A one-per-rev pattern indicates that there is one area of pressure deficit that is equal and opposite to an area of high pressure. A multiple-per-rev indicates that the MPR is greater than one and therefore there are multiple extents of total pressure deficit. The one-per-rev example is shown in Figure 3.3 has a circumferential pressure intensity of about 0.05, and a 0.04 circumferential pressure intensity is experienced for the 1.8 MPR example.

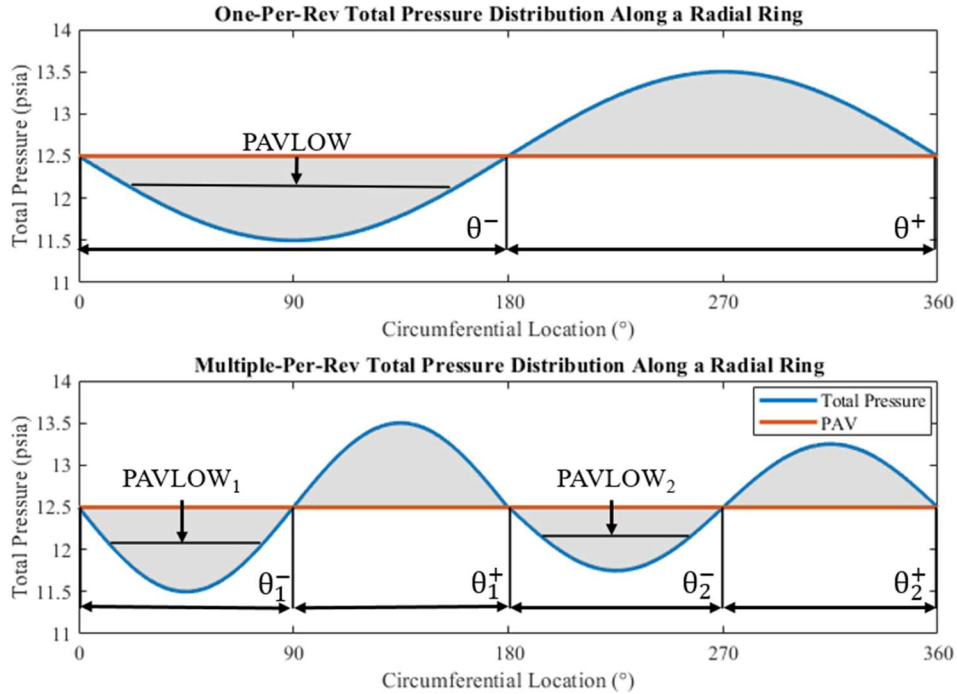


Figure 3.3. Graphic of terms needed to calculate total pressure distortion descriptors

The variables shown in the figures were used in the analytical development of total pressure distortion descriptors in this effort. As discussed earlier, the extent for each pressure region was developed using equation (3.6). The PAV, or average pressure along the ring, was determined using equation (3.7). Similarly, PAVLOW, or average pressure deficit in each of the low-pressure extents, was calculated using equation (3.8). These values are needed to calculate the pressure intensity and MPR along the ring:

$$PAV_i = \frac{1}{360} \int_0^{360} P_i(\theta) d\theta \quad \text{and} \quad (3.7)$$

$$PAVLOW_{i,k} = \frac{1}{\theta_{i,k}^-} \int_{\theta_{i,k}^-} P_i(\theta) d\theta . \quad (3.8)$$

PAV and PAVLOW were used to obtain the circumferential pressure intensity of each extent along the  $i^{\text{th}}$  ring using equation (3.9). The total ring pressure intensity is then realized using equation (3.10), where Q is the total number of pressure deficit extents along the ring. These intensity values were also used to develop the MPR of the circumferential pressure distribution along the  $i^{\text{th}}$  ring using equation (3.11). MPR is a measure of how many equal and opposite regions of total pressure extents there are along the ring:

$$PI_{Circ|i,k} = \frac{PAV_i - PAVLOW_{i,k}}{PAV_i} , \quad (3.9)$$

$$PI_{Circ|i} = \frac{\sum_{k=1}^Q (PI_{Circ|i,k} \theta_{i,k}^-)}{\sum_{k=1}^Q \theta_{i,k}^-} , \text{ and} \quad (3.10)$$

$$MPR_i = \frac{\sum_{k=1}^Q (PI_{Circ|i,k} \theta_{i,k}^-)}{\max(PI_{Circ|i,k} \theta_{i,k}^-)} . \quad (3.11)$$

Radial distortion indices are often less insightful for experiment data, as they are taken relative to the face average total pressure at the AIP, and thus sum to zero. However, they can be used to determine if the boundary layer effects are dominant at the rake hub instrumentation as well as if a model is capturing the correct radial total pressure loss. To calculate these radial descriptors, the face average pressure, PFAV, was first found using equation (3.12) and was used in equation (3.13) to calculate the radial intensity of pressure distortion at each radial location. N

in (3.12) is the number of radial locations measured, which is equal to the number of instruments per rake:

$$PFAV = \frac{\sum_{i=1}^N PAV_i}{N} \text{ and} \quad (3.12)$$

$$PI_{Rad}|_i = \frac{PFAV - PAV_i}{PFAV} . \quad (3.13)$$

For total pressure distortion, the crucial extent angle must be a factor in determining these descriptors. The critical angle was considered per AIR1419 Aerospace Standard (2017) guidelines and was incorporated in the manner recommended. However, instead of considering a critical extent angle of  $25^\circ$  as a recommended starting point by this standard, the method of calculating  $\theta_{crit}$  as developed by Cousins (2004) was utilized. This method is a simple relationship, whereby the critical angle is approximately 2 to 3 times the circumferential extent of the blade passages. In this effort, the multiplying factor was selected as 2.5.  $\theta_{crit}$  was therefore calculated to be  $53^\circ$  using (3.14):

$$\theta_{crit} = 2.5 \left( \frac{360^\circ}{z} \right) = 2.5 \left( \frac{360^\circ}{17} \right) = 53.0^\circ . \quad (3.14)$$

### 3.2.2 Swirl Distortion Descriptors

Swirl distortion descriptors are distinct to pressure descriptors. They are not developed relative to an average, but rather to a swirl value of  $0^\circ$ . This method was originally proposed by Bouldin and Sheoran (2002) and adopted by SAE International in AIR5686 (2017) as a standard for assessing swirl distortion. Swirl distortion parameters are more effective than those of pressure indices as they are relative to an absolute value rather than the average of an operating condition. An example of a one-per-rev and a multiple-per-rev swirl distributions both with a swirl intensity of 5 is shown in Figure 3.4. In both plots, the extents are shown along with the respective average sector swirl (SS) for each extent. Extents for swirl and SS, are taken relative to the 0-swirl value and not the average swirl in the distribution.

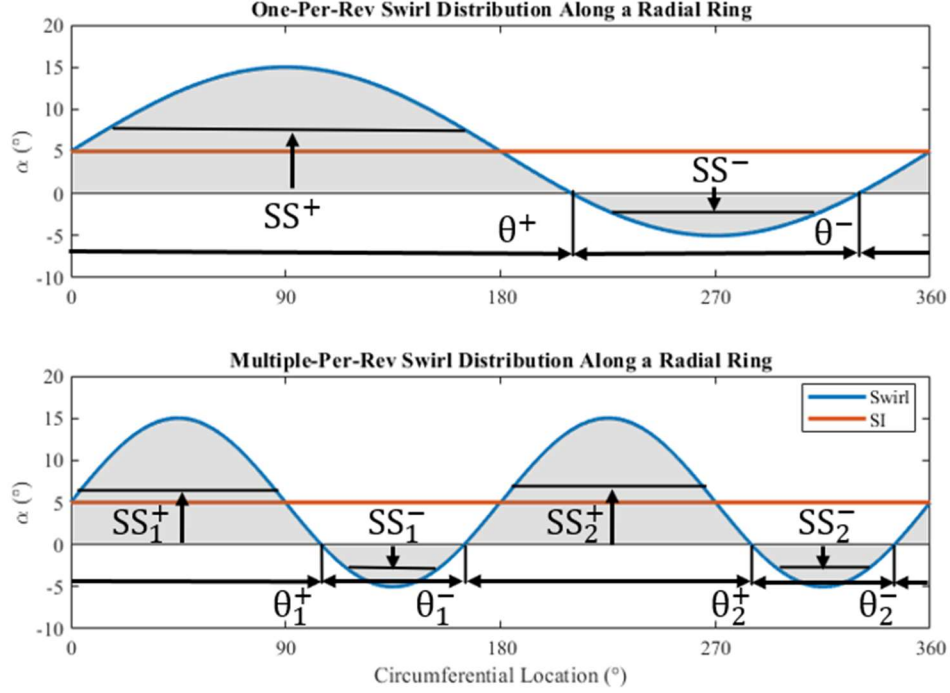


Figure 3.4. Graphic of terms needed to calculate swirl distortion descriptors

The swirl distortion descriptor calculation was started by determining SS using equation (3.15) for all positive and negative extents:

$$SS_{i,k}^+ = \frac{1}{\theta_{i,k}^+} \int_{\theta_{i,k}^+} \alpha_i(\theta) d\theta \quad \text{and} \quad SS_{i,k}^- = \frac{1}{\theta_{i,k}^-} \int_{\theta_{i,k}^-} \alpha_i(\theta) d\theta . \quad (3.15)$$

SS is the average swirl within an extent. The summation of the positive and negative SS components was used along with the summation of the positive and negative extent terms to develop an expression for the swirl intensity (SI) and swirl directivity (SD). SI is the average absolute value of swirl along the instrumentation ring and is obtained using equation (3.16):

$$SI_i = \frac{\sum_{k=1}^Q SS_{i,k}^+ \theta_{i,k}^+ + \sum_{k=1}^Q |SS_{i,k}^-| \theta_{i,k}^-}{360^{\circ}} . \quad (3.16)$$

The rotational direction of the swirl is characterized by SD, which is the average direction of the flow along the radial ring. SD was calculated using equation (3.17) and is defined between values of -1, full counter-swirl, and 1, full co-swirl:

$$SD_i = \frac{\sum_{k=1}^Q SS_{i,k}^+ \theta_{i,k}^+ + \sum_{k=1}^Q SS_{i,k}^- \theta_{i,k}^-}{SI_i (360^\circ)} . \quad (3.17)$$

The amount of equal and counter-rotating swirl pairs (SP) is another descriptor to define the swirl behavior of the flow. SP was realized using equation (3.18). An SP value of 0.5 represents bulk swirl, 1 is indicative of the presence of twin swirl vortex pairs and any value in between represent these represents an offset swirl pair at the AIP. An SP value above one indicates the presence of a multiple-per-rev swirl pattern (Sheoran and Bouldin, 2008):

$$SP_i = \frac{\sum_{k=1}^Q SS_{i,k}^+ \theta_{i,k}^+ + \sum_{k=1}^Q |SS_{i,k}^-| \theta_{i,k}^-}{2(\max of (\sum_{k=1}^Q SS_{i,k}^+ \theta_{i,k}^+ OR \sum_{k=1}^Q |SS_{i,k}^-| \theta_{i,k}^-))} . \quad (3.18)$$

### 3.3 Computational Model Data

Data from the computational models were extracted from CFX results files using ANSYS CFX Post. For both the Plenum and Full-Inlet models, the data were extracted at the same traverse locations used in the experiment. The models with three-hole probes included had a different method of data extraction and processing from the standard models, which required more post processing.

#### 3.3.1 Extraction and Processing of CFD Data at AIP

For the purposes of replicating experimental data at the AIP for the Plenum and Full-Inlet models, the cartesian coordinates of the experimental traverse locations were imported into CFX Post as polylines represented as black circles in Figure 3.5. Furthermore, to prevent post-processing inconsistencies between CFD and experiment, the same methodology and codes as were that used for the processing of experiment data were adapted to accept data from CFD. Mach number, static pressure, total pressure, and the x, y, and z components of velocity were exported along the four inner most polylines that reproduce the rotatable rake three-hole probe survey points. A further polyline was included along the shroud to gather static pressure data as there is an additional static pressure tap on the base of the rotatable rake.

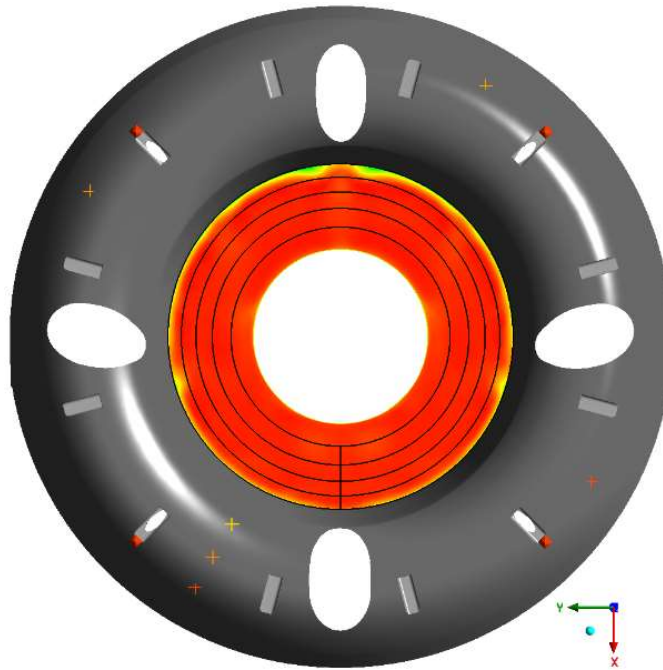


Figure 3.5. CFX Post rotatable rake polyline at AIP and unit vector directions

Mach number, total pressure and static pressure values were not manipulated as they are direct outputs from CFX Post. However, swirl angle had to be determined from the 3D cartesian velocity components. Swirl is the angle between the tangential and axial velocities for a given circumferential location. Therefore, the tangential component of velocity is required. A benefit of the CFD polyline data, is that the radial flow velocity can also be calculated, which could not be resolved in the experiment as a five-hole probe would need to be used to determine the pitch angle. This permits the extrapolation of the radial swirl angle in addition to the circumferential angle. The tangential and radial velocity components are depicted at the AIP in Figure 3.6.

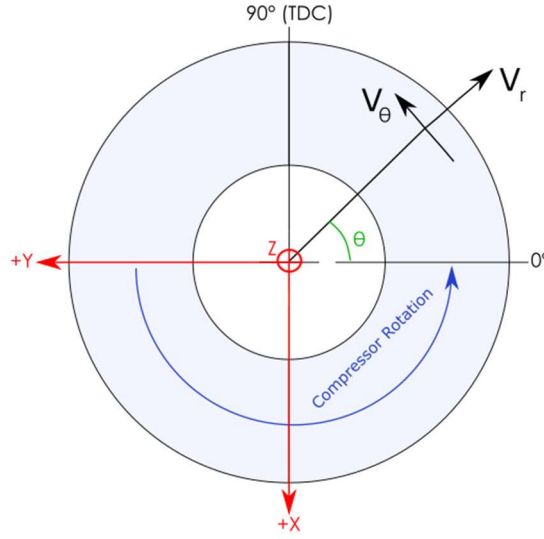


Figure 3.6. AIP coordinate system from CFX Post and r-θ velocities

To calculate the tangential and radial velocities, a rotation matrix was used for each data point along with the 2D planar AIP velocities.  $\theta$  was defined as increasing counterclockwise with the zero-value assigned as  $90^\circ$  clockwise from TDC rendering it analogous to the unit circle. Counter-clockwise was selected as the increasing  $\theta$  direction as this is the direction of rotation of the centrifugal compressor used in the experiment, and thus, the sign convention of co-swirl and counter-swirl was maintained. Calculation of the tangential and radial velocity is achieved using rotation matrices, as shown in equations (3.19) and (3.20) respectively. The flow angle relationships with the r- $\theta$ -z velocities are depicted graphically in Figure 3.7 and are calculated trigonometrically using the results of equations (3.19) and (3.20) with equations (3.21) and (3.22):

$$V_\theta = \begin{bmatrix} V_x \\ V_y \end{bmatrix} \cdot \begin{bmatrix} -\sin(90 - \theta) \\ \cos(90 - \theta) \end{bmatrix}, \quad (3.19)$$

$$V_r = \begin{bmatrix} V_x \\ V_y \end{bmatrix} \cdot \begin{bmatrix} -\cos(\theta) \\ -\sin(\theta) \end{bmatrix}, \quad (3.20)$$

$$\alpha = \text{atan}\left(\frac{V_\theta}{V_z}\right), \text{ and} \quad (3.21)$$



$$|\zeta| = \left| \text{atan} \left( \frac{V_r}{V_z} \right) \right|. \quad (3.22)$$

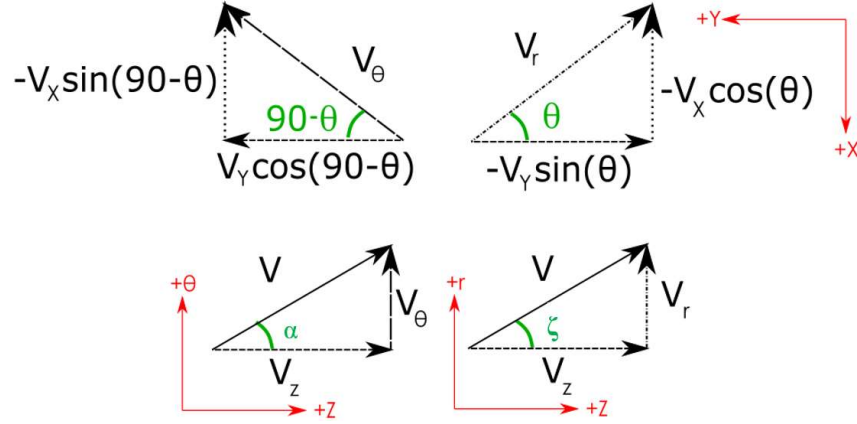


Figure 3.7. Velocity triangles used to calculate swirl and radial flow angle

For this effort, only the absolute value of radial swirl angle,  $\zeta$ , was required as these data were not taken experimentally, and  $\zeta$  was only considered to analyze the veracity of AIP instrumentation readings.

### 3.3.2 Computational Three-Hole Probe Model Data Extraction and Processing

Data extraction for the computational models that included three-hole probes is dissimilar to the standard models. As previously discussed, pressure taps were included in the mesh of the probes to allow flow to stagnate. The pressure data were extracted from the back face of these pressure taps to allow for this stagnation to occur. The same processing method that was used for the experimental data, as outlined in section 3.1, and was adapted to accept the pressure values from the five CFD three-hole probe models that provided 20 rake traverse points. Instead of using different calibrations for each probe, the calibrations were averaged. The intention was to reduce the effect of the minute manufacturing defects from the experimental probes impacting the values obtained from the computational model, as these physical flaws are not present in the mesh. This resulted in the calibration curves shown in Figure 3.8.

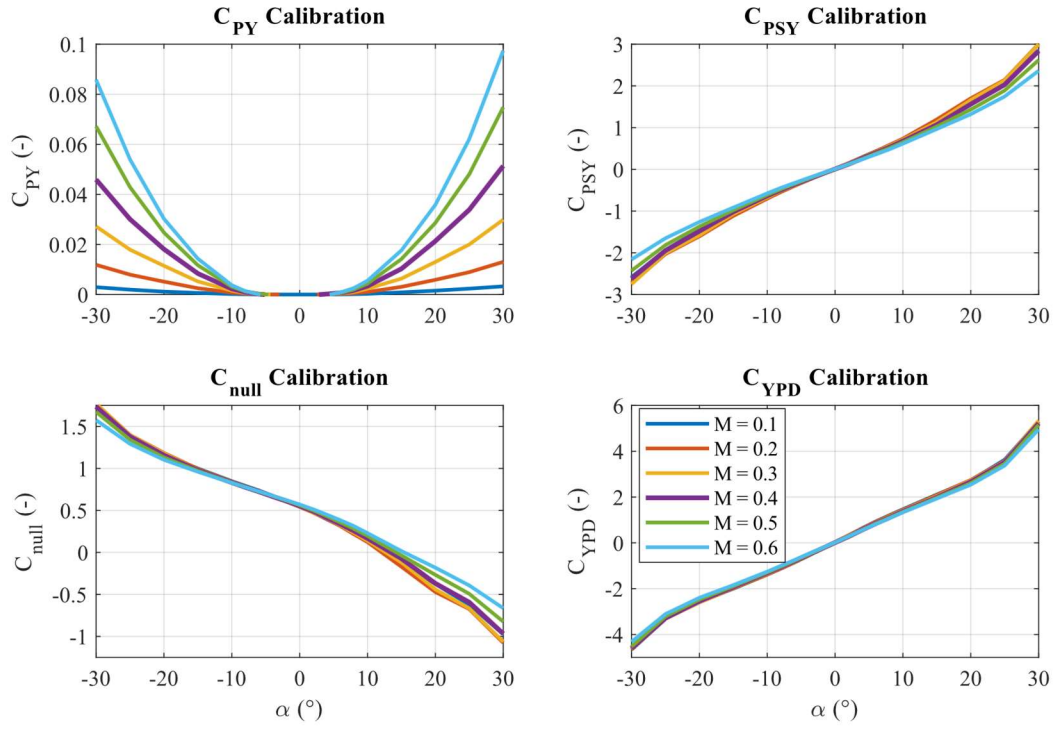


Figure 3.8. Averaged calibrations used for CFD three-hole probe data analysis

## 4. COMPUTATIONAL MODEL RESULTS AND COMPARISON WITH EXPERIMENT

In this chapter, results from the plenum and full-inlet models are compared with those from experiment. An analysis of specific inlet components' effects on the AIP flow profile is laid out and an inspection of the three-hole probe effectiveness is presented. Distortion descriptors are utilized to compare the multitude of data points for both swirl and total pressure distortions, along with contours of AIP flow conditions.

### 4.1 Selected Operating Points for Analysis

For the experimental test campaign, the compressor performance was mapped at 80%, 90%, 95%, and 100% corrected speed for all APU inlet configurations. AIP surveys were conducted in choke at an identical throttle setting, halfway through the speed line, and approaching surge. The 90% and 95% stable operating profile is restricted to a smaller range; therefore, one survey was taken at 90% in choke, and two surveys were conducted at 95% speed with one in choke and one after the speed-line knee. Simulations were conducted at the highest and lowest mass flow rates measured in each configuration. These operating points are 100% corrected speed in choke and 80% speed at high loading. The compressor map, survey points, and CFD simulation points are shown in Figure 4.1.

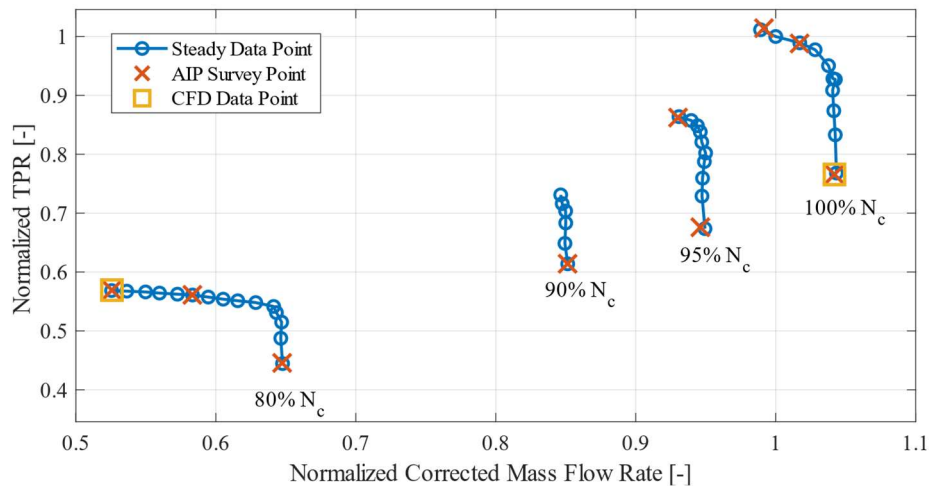


Figure 4.1. Operating points for experiment surveys and CFD simulations

## **4.2 Effects of Individual Inlet Components on Annulus Flow Field**

The inlet plenum geometry of the SSCC APU inlet contains several obstructions that produce characteristic wakes that appear at the AIP. Struts, inlet rakes, shroud instrumentation notches, and sandwich pack rakes are all located in the plenum domains of the CFD simulations. The distinguishing total pressure deficits at the AIP can be recognized after an individual component assessment has been conducted considering the flow patterns within the plenum. For this purpose, the flow directions within the plenum and how these interact with individual inlet components are analyzed in this section. Plenum model streamline data of three cases are presented: the nominal  $0^\circ$  baffle with no blocker plate, the  $70^\circ$  baffle with no blocker plate, and the 50% left blockage plate individual. These inlet configurations are illustrated in Figure 2.4 and Figure 2.5. The affects each of the main inlet components are analyzed for each configuration. The cases presented are the most severe inlet distortions generated in this effort. Ranges of the total pressures presented is maintained between cases for qualitative comparison purposes.

### **4.2.1 Struts**

Within the plenum, the largest flow obstruction is caused by the inlet struts. These span the entire annulus and have a significant cross-sectional area. The symmetric airfoil profile of both the TDC and BDC are identical and are oriented parallel to the plenum's center axis. The  $0^\circ$  and  $180^\circ$  struts on the right and left side of the inlet when observed FLA, are angled upward toward the incoming flow to reduce the incidence of the struts at nominal conditions. This geometry is depicted in Figure 4.2 along with streamlines from the struts to the AIP colored by total pressure. Blue represents lower total pressure, and red indicates a higher total pressure.

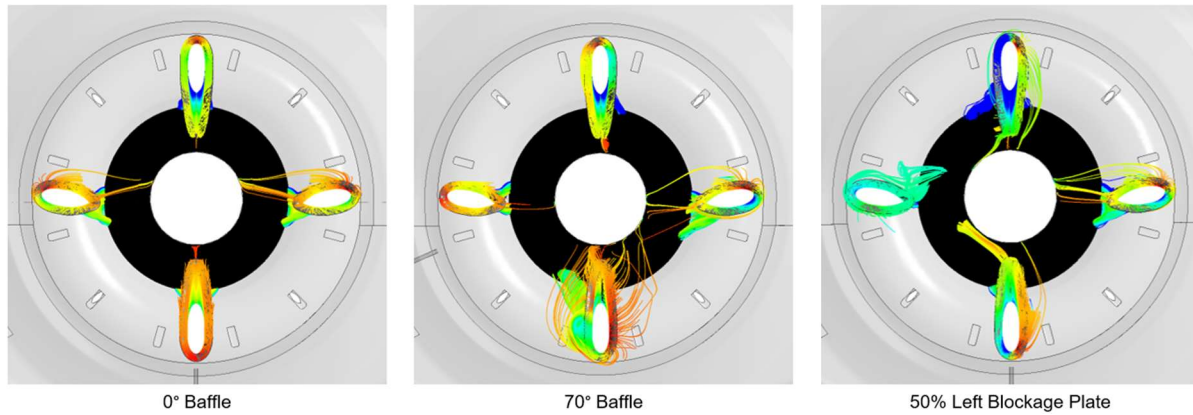


Figure 4.2. Strut wakes visualized by streamlines colored by total pressure for 0° and 70° baffles, and 50% left blockage plate configurations viewed FLA

When twin swirl is dominant in the plenum, the wakes from the TDC and BDC struts are at a minimum. This is attributable to the flow being parallel to the chord of the symmetric airfoil profile. The left and right struts show larger wakes at this configuration and significant separation is present as represented by the streamlines diverting off the bottom surface of the strut. This is an indication that the strut is not angled sufficiently upward for 0 incidence at the highest mass flow rate condition. The 70° baffle case shows the effect of bulk counter-swirl on the struts. The incidence of the BDC and TDC struts is no longer 0°. The TDC encounters minor separation off the right side, but the BDC strut has major separation off the left side due to the significant incidence caused by the flow angularity. This loss spans a large area and has a significant impact on AIP total pressure distortion. The left strut flow is like the nominal case, as the top left quadrant is predominantly unaffected by the baffle located in the bottom left quadrant. The right strut shows separation of similar intensity and pattern to the BDC strut due to a comparable increase in incidence. Finally, the 50% left blockage plate produces the largest deviation from nominal conditions. The right-side strut behavior is comparable to that of the nominal case, with slightly more total pressure loss due to the mixing upstream caused by the blocker plate. The flow redistribution from the right side of the plenum to the left creates large incidence for both the TDC and BDC struts and causes considerable separation off the left surface. Redistribution along the top half of the annulus causes considerable mixing in the top left quadrant, and this induces the detached vortex off the top side of the left strut.

These three cases demonstrate that the struts have a large effect on the total pressure loss at the AIP and that separation is injected into the annulus. The effects of less aggressive baffles reduce separation from the struts due to small incidence angles. The location of the shed wakes will not migrate significantly unless the baffle is shifted to the opposite side of the annulus. In this case, the wakes will be shed from the opposite surface. This same phenomenon is experienced by the blocker plate configurations. If less of the plenum inlet is blocked, then the same patterns will be seen but with a reduced total pressure deficit and expanse. The location will be the same until the blockage is shifted from one side of the annulus to the other, the same as with a baffle.

#### 4.2.2 Inlet Rakes

The inlet total pressure rakes located circumferentially within the plenum at  $45^\circ$ ,  $135^\circ$ ,  $225^\circ$ , and  $315^\circ$ , with respect to TDC, also accord a conspicuous separation profile at the AIP. The body of the rakes is a truncated symmetric airfoil profile, and each is oriented radially outward. Flow within the plenum does not enter the annulus radially in most locations, and this installation creates an incidence between the rakes and the incoming flow. Figure 4.3 depicts the rakes in these locations along with streamlines indicating the total pressure of the flow once leaving the surface of the rakes.

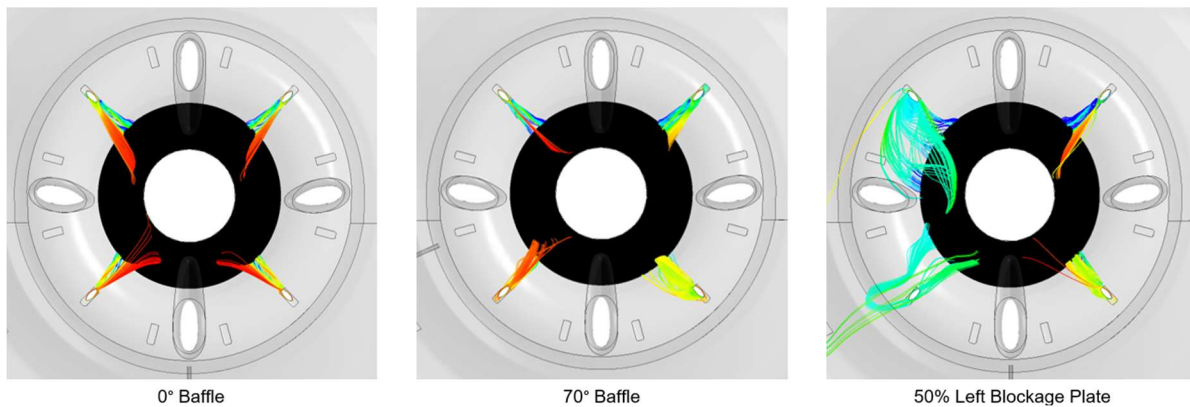


Figure 4.3. Inlet rake wakes visualized by streamlines colored by total pressure for  $0^\circ$  and  $70^\circ$  baffles, and 50% left blockage plate configurations viewed FLA

As with the left and right struts, the inlet rakes are not coincident with the incoming flow for any configuration, thus, inducing separation and loss from the ‘suction side’ of the airfoil profile. In the top half of the plenum in the nominal configuration, flow direction is predominantly from the top of the plenum downward. With the rakes being oriented radially outward, this creates a large incidence with the incoming flow. The consequence is the separation zone from the top side of the rake surface being ingested along the shroud. Flow also deviates from the bottom surfaces and produces smaller total pressure deficits into the midspan regions of the annulus. A similar structure exists in the bottom half of the plenum, with the total pressure loss incurred by the upward facing surface of the rake. In the 70° baffle configuration, the 225° inlet rake in the lower left quadrant is near coincident with the incoming flow and shows a lower total pressure loss and no major deviation of flow off the rake body compared to the nominal case. For the same reason as with the struts, the 135° inlet rake is not greatly affected by the change in configuration. The only effect on this rake is that the pressure gradient due to the presence of the baffle pushes the flow that deviates from the bottom side of this rake upward in the annulus. The right-hand side rakes induce significantly more total pressure loss due to the higher tangential component of the inlet flow created by the 70° baffle. Right-hand rakes when observed in the 50% left blockage configuration, do not experience flow significantly different from the nominal case and present similar total pressure loss and the extent of this region in the AIP. The left-hand side rakes encounter a disturbed incoming flow due to redistribution along the top of the plenum beneath the blocker plate. The 135° rake develops a similar flow separation structure to a flat plate at a high angle-of-attack, where flow completely separates off the leading edge. The same can be observed on the bottom left rake, however, the extent of the AIP covered by this region is lower in comparison.

As with the case of the struts, a less severe baffle or blocker plate will show a muted total pressure deficit in the same location. The position of the deficit will be altered if the baffle or blocker plate are shifted across the center axis of the plenum. In this case, the total pressure loss and swirl due to these components is mirrored at the AIP plane.

#### **4.2.3 Shroud Instrumentation Notches**

Instrumentation notches are present along the shroud of the plenum inlet of the SSCC. A total of 12 notches are distributed about the annulus in 30° increments and are oriented radially.

The notches are small rectangle profiles removed from the shroud along the radial-to-axial bend into the annulus. An example of one of these notches is depicted in Figure 4.4.

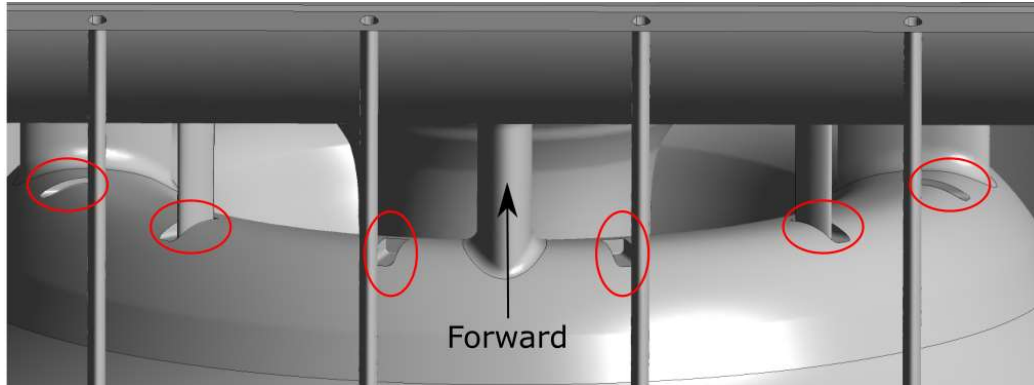


Figure 4.4. Rendering of shroud notches within plenum viewed top-down

The purpose of these notches is to secure inlet rakes and the four inlet rakes previously discussed are outfitted to four of these incisions. However, the rake body does not occupy the notch in its entirety as shown in Figure 4.4, and, therefore, further separation is caused at the root of the rake by the notch. The rectangular profile of the notches produces corner separation as illustrated by Figure 4.5.

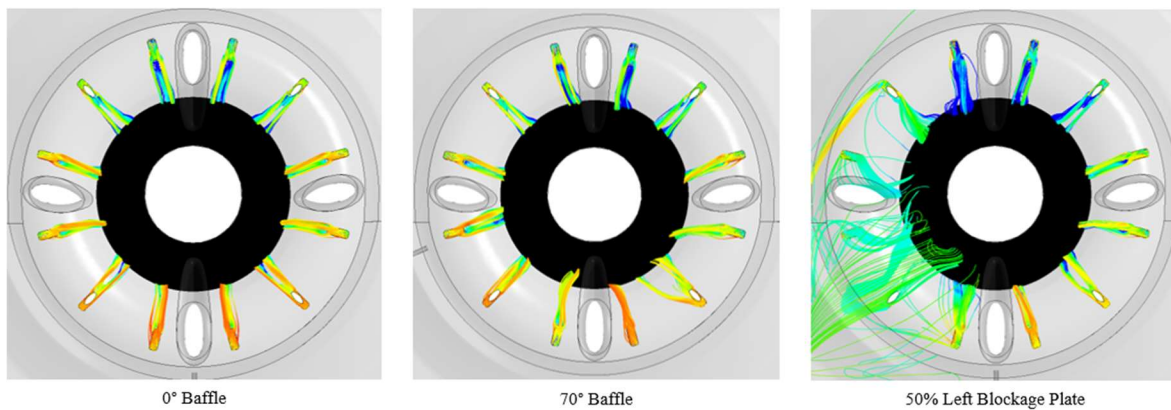


Figure 4.5. Shroud notch wakes visualized by streamlines colored by total pressure for  $0^\circ$  and  $70^\circ$  baffles, and 50% left blockage plate configurations viewed FLA



In the nominal configuration, the loss from the notches is insignificant everywhere except for TDC, and the extent of the pressure deficits are minimal. Regions of total pressure deficit are located along the shroud wall and the most loss is incurred within the higher momentum region. As presented in section 2.2.5, a low static pressure region is expected on the top half of the annulus along the shroud. The suction from this region attracts the flow at TDC to pass over of the two notches at the top of the plenum and prevents them from migrating into the mid passage for all configurations. In the baffle cases, there is minimal separation from the side edges of the notches and wakes are contained to the shroud of the annulus. The blocker plate case, however, shows significantly more tangential flow on the side experiencing the blockage due to flow redistribution. In the top left quadrant in this configuration, flow separates on the two lower notches and passes into the bottom half of the plenum. The bottom left quadrant incisions experience large tangential flow and, thus, flow separates from the corners of rectangular notches and returns to the outer regions of the plenum. The return flow interacts with wakes that are shed from upstream and, consequently, when this flow is ingested into the annulus, it occupies a larger extent of the AIP due to mixing. Flow passing over notches on the unblocked side of the plenum shows the same structure as the baffle cases. The notches are not a significant cause of loss in the main flow path. The exception to this is the regions of large tangential flow where the flow can re-enter the bottom half of the plenum.

#### **4.2.4 Sandwich Pack Rakes**

Six sandwich pack rakes are spaced evenly at the inlet of the plenum and are oriented to be coincident to the bulk flow entering the plenum from the APU elbow. Figure 4.6 presents the location of these rakes and streamline behavior of the flow that passes over the surfaces of the rake bodies.

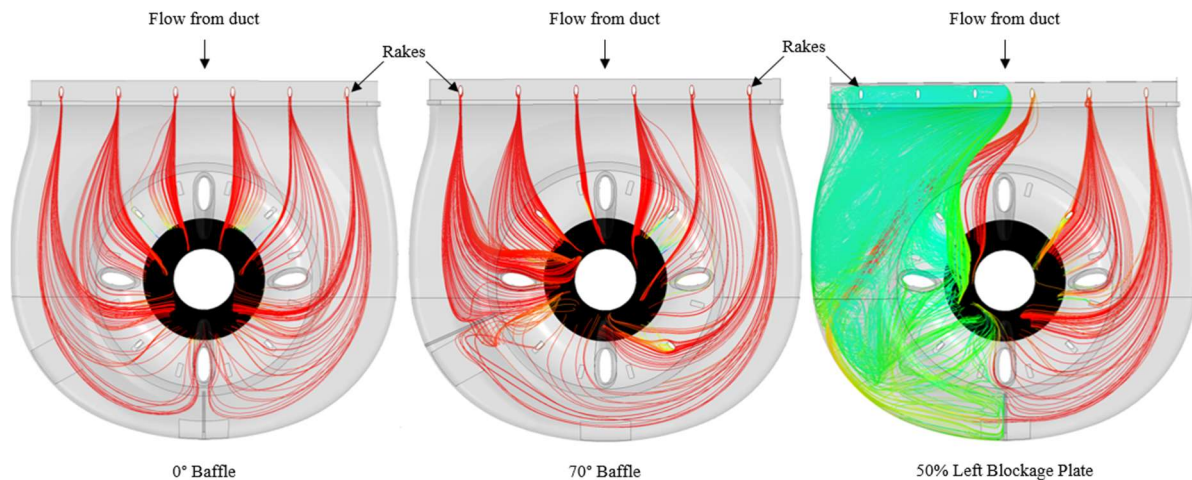


Figure 4.6. Sandwich pack rake wakes visualized by streamlines colored by total pressure for 0° and 70° baffles, and 50% left blockage plate configurations viewed FLA

In the nominal and 70° baffle cases, there is insignificant low total pressure regions across the sandwich pack rake bodies. Furthermore, the flow presents insignificant deviation from the original path into the plenum. This indicates that the flow is coincident with these rakes at all baffle configurations and that baffle installations do not affect the upstream elbow flow significantly. Similarly, the blocker plate cases, do not have a significant impact on the incoming stream. As flow passes over the edge of the plate, it is redistributed toward the blocked region and the bulk flow bypasses the rakes. Thus, the loss of total pressure in this configuration is attributable to the blockage plate itself. The flow redistribution downstream of the blockage plate induces a significant amount of mixing and this structure encounters other inlet components such as the struts or inlet total pressure rakes. The mixing in this configuration affects almost half of the annulus at the AIP as shown in Figure 4.6. Therefore, the sandwich pack wakes are not able to be seen at the AIP in the blocker plate configurations either, as most of the loss in this region is incurred by perturbations induced by the blockage plate.

#### 4.2.5 Cumulative Component Effects on Annulus Flow

Flow that is perturbed by struts, inlet total pressure rakes and shroud instrumentation notches present distinct hallmarks in the AIP profile. Utilizing analysis of sections 4.2.1 through 4.2.4 allows an understanding of the individual components effects and this can be applied to the

inlet contours from experiment and simulations to determine causation of different distortions at the AIP. An example of this is provided in Figure 4.7, where experimental and computational AIP total pressure profiles for the three cases previously analyzed are presented. Each total pressure deficit region is identified with a geometric shape to indicate the cause of the loss.

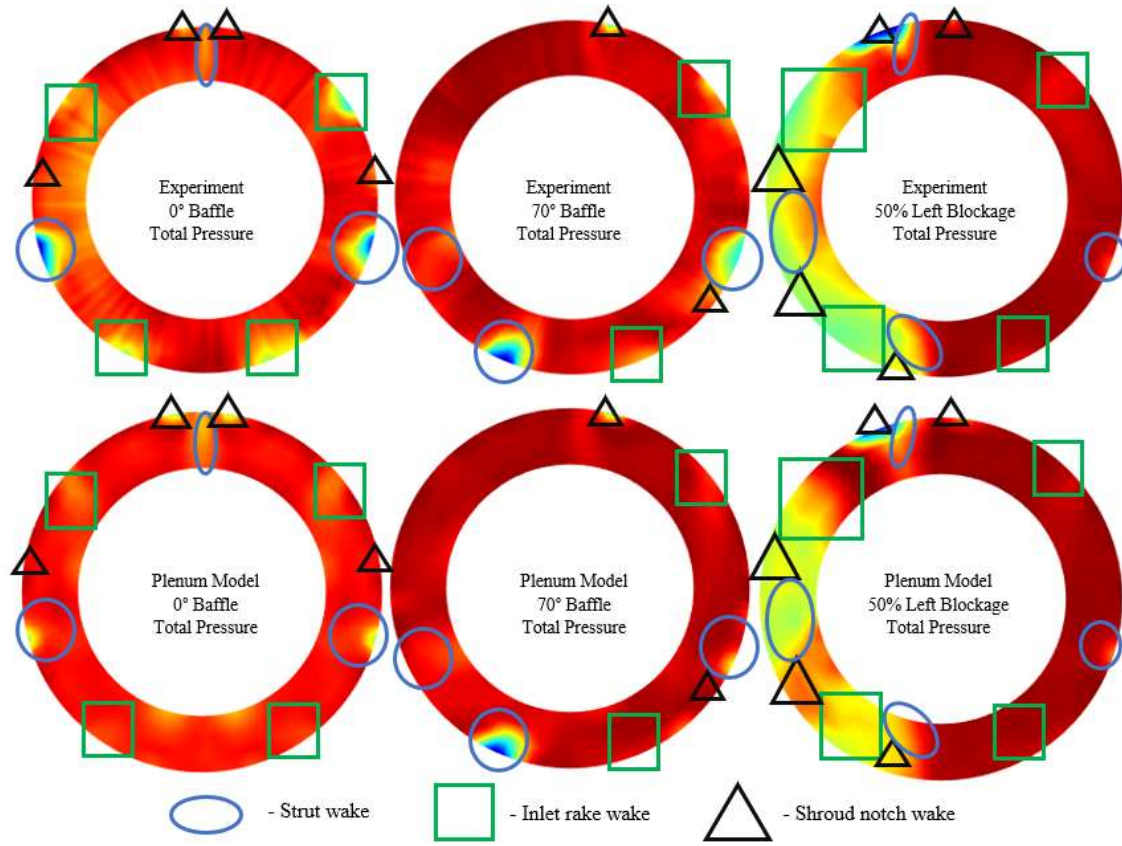


Figure 4.7. Experiment and computational model AIP total pressure deficit zones caused by wakes of inlet components

The streamline visualizations show similar total pressure losses to the experiment. Notably, the sandwich pack rakes do not affect the AIP rakes themselves, which agrees with the plenum model CFD streamline data. Furthermore, the AIP profiles from experiment support the idea that superposition of AIP loss profiles caused by different inlet components is an effective method to develop an understanding of the total pressure profile. The streamline data with the indicated total pressure losses show reasonable agreement with experiment, indicating that the use of a reduced

plenum model to qualitatively understand the total pressure loss of each inlet component at the AIP is justified.

### 4.3 Three-Hole Probe Effectiveness

Multi-hole probes are a versatile instrument that can characterize static pressures, Mach numbers, total pressures, and flow angles. As previously discussed, the probes used in this investigation are of a three-hole trapezoidal geometry, which compared to five-hole probes have added uncertainties due to not being able to be corrected for radial flow angles. Furthermore, multi-hole probes suffer from wall-effect uncertainties due to horseshoe vortex formations or flow contractions. The combination of these effects can alter flow data that is captured. The severity of these ramifications can be difficult to ascertain, and the respective causations impractical to decouple.

#### 4.3.1 Radial Flow Angle Effects

Three-hole probes are only able to capture flow angles in one axis. In the case of this experimental effort, the probes were oriented to capture the circumferential swirl angle, and therefore, the radial flow angle was not measured. Despite this angle not being resolved, it does impact measurement readings. Dudinski and Krause (1969) compared three-hole and five-hole probe performance at a range of Reynolds numbers, Mach numbers, and flow angles and indicated that three-hole probe performance degrades severely at radial flow angles of magnitude  $10^\circ$ . This finding was corroborated by Argüelles Díaz et al. (2010), whereby radial flow angles were indicated to be a larger contributor to error than Reynolds number effects for three-hole probes. Thus, to determine potential sources of inaccuracy in the measurement technique used at the AIP, the radial flow angles must be estimated and areas with magnitudes greater than  $10^\circ$  identified.

As the experimental method did not provide a means of resolving the radial flow angles at the AIP, the analysis relies solely on CFD results. Figure 4.8 provides contours of the magnitude of the absolute radial flow angle,  $|\zeta|$ , from both the plenum and full-inlet models. Regions of  $\zeta$  magnitudes greater than  $10^\circ$  are represented by the highest level of red on the color bar. The operating scheme for these contours was 100% corrected speed in choke at the nominal  $0^\circ$  baffle and no blockage plate configuration. The contours indicate that the outermost instrumentation ring

in the annulus experiences radial flow angle magnitudes above the acceptable threshold in several locations. For both models, a large radial component of flow exists in the inner instrumentation rings at BDC because of flow redirection caused by the baffle. However, this is the only location where the magnitude is high outside of the shroud-side instrument ring. Both models show remarkable agreement with variations in the magnitude of the radial flow angle being within  $1^\circ$  of each other throughout most of the annulus. The largest difference occurring at BDC towards the hub, where the ‘dead-zone’ resides in plenum model simulations. This is an indication of a minor drawback to the plenum model, whereby flow is not able to redistribute upstream of the radial inlet section and, therefore, is distributed evenly at the inlet of the plenum. This incurs a ‘sloshing’ effect at BDC due to there being less flowrate through that section compared to the full-inlet case as indicated by the regions of low radial flow angle surrounding the high-region at BDC. Despite this difference, both models demonstrate that the shroud-side three-hole probe encounters magnitudes of radial flow angle greater than  $10^\circ$ .

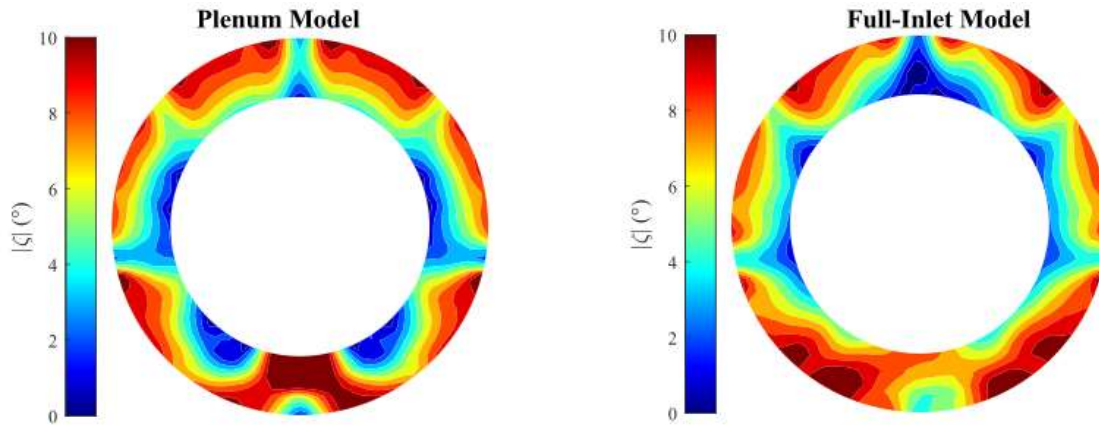


Figure 4.8. Nominal configuration radial flow angles from CFD simulations for both models at AIP

#### 4.3.2 Shroud-Side End Wall Effects

Shroud-side probes are also impacted by end wall effects in conjunction with high radial flow magnitudes. This is a common drawback to probes, as when they are fastened to a wall, a horseshoe vortex forms upstream leading to an increased static pressure being measured by the probes. This was investigated by Treaster and Yocum (1978). In this work, they defined methods to calculate static pressure, total pressure, circumferential flow angle, and radial flow angle, from

five-hole probes. The relationship to determine static pressure that they provided can be rearranged as shown in equation (4.1):

$$P_s = P_C - \frac{P_R - P_L}{C_{p,static}}. \quad (4.1)$$

The relationship between probe distance from the wall fixture, and  $C_{p,static}$  was investigated by Treaster and Yocum (1978) under different values of circumferential swirl angle. These data are presented in Figure 4.9 with the shroud-side rotatable rake element probe diameter being represented by the black vertical line. From the data presented, the location of the probe along the shroud does have a minor effect on the static pressure indications from the probe because  $C_{p,static}$  is elevated. From equation (4.1), an increase in  $C_{p,static}$ , results in an increase in static pressure as the differential pressure term between the two side pressure taps is reduced by the larger denominator. This pressure increase is a consequence of the probe lying within a horseshoe vortex that forms upstream of the probe body.

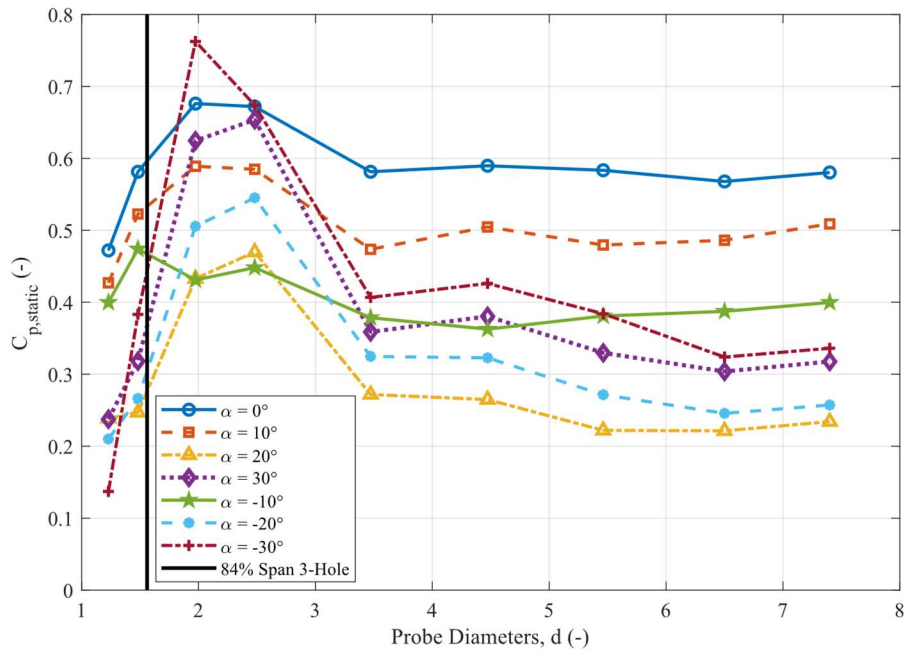


Figure 4.9.  $C_{p,static}$  values for a multi-hole probe fixed to a wall with varying yaw angles (Treaster and Yocum, 1978)

The generation of this increased static pressure zone severely impacts the Mach number indicated by the probes. Along the shroud, the Mach number from experiment is measured as lower than it is in CFD due to the probe geometry influencing the local pressure. Michelassi and Giachi (1997) and Pazzi and Michelassi (2001) performed experimental and CFD analyses on the flow in radial-to-axial inlets. The experiments both used three-hole probes that traversed the whole annulus, and the findings indicated a similar increase in static pressure in the experiment along the shroud. This is represented in Figure 4.10 alongside the SSCC data in the nominal configuration at 100% speed in choke. The three different data sets indicate the same Mach number disparity between CFD and experiment along the shroud. The CFD data indicate a higher Mach number along the shroud than the experiment. One notable difference between the SSCC contour and the other two, is that the SSCC contour data covers from 26% annulus span to 84% span, whereas the other two cases presented from literature show the annulus in its entirety. Considering this fact, the trends between all three are remarkably similar and are evidence of wall effects altering local static pressure. It is also an indication that radial-to-axial inlets inherently produce high radial flow angles along the shroud of the annulus, and this causes inaccurate Mach number measurements from three-hole probes.



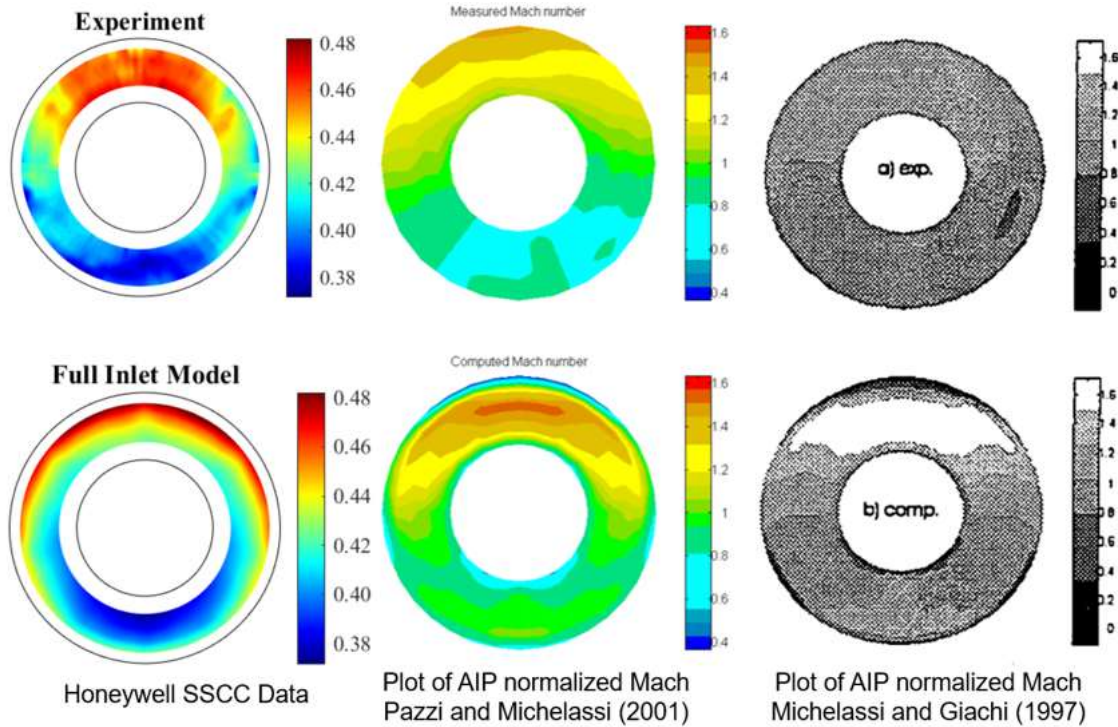


Figure 4.10. Nominal SSCC Mach number data compared to Pazzi and Michelassi (2001) and Michelassi and Giachi (1997)

### 4.3.3 Hub-Side End Wall Effects

Probes with a gap between the tip and wall change indicated static pressures similarly to the near-wall fixture effects on multi-hole probes. The hub-side probe of the SSCC rotatable rake is situated with a gap between the hub of the annulus and the rake body, which, instead of a flow deceleration in the shroud-side case, induces flow acceleration. This leads to a lower value of static pressure than is present in an unperturbed flow field. Treaster and Yocum (1978) analyzed this geometry case experimentally, yielding  $C_{p,static}$  data illustrated in Figure 4.11, with the SSCC 26% span probe represented as a vertical black line. According to the data presented, the geometric location of the hub-side three-hole probe induces a significant drop in  $C_{p,static}$ . This is the opposite trend to the shroud-side probe is indicated as  $C_{p,static}$  decreases near to the wall and is significantly decreased for the SSCC hub-side three-hole probe. This decrease in  $C_{p,static}$  reduces the denominator in the static pressure equation (4.1), thereby reducing the static pressure indicated by the three-hole probe. This leads to a significant elevation in the Mach number being indicated



along the hub of the annulus. This occurs as suggested in the SSCC data and in the contours presented by Pazzi and Michellassi (2001) in Figure 4.10.

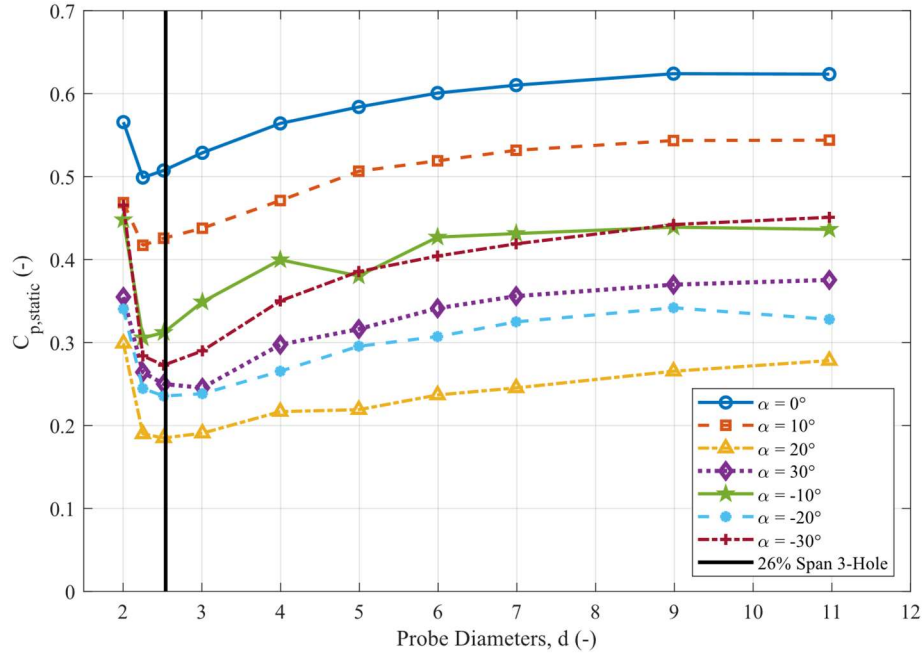


Figure 4.11.  $C_{p,static}$  values for a multi-hole probe suspended above a wall with varying yaw angles (Treaster and Yocum, 1978)

#### 4.3.4 Three-Hole Probe Model Results

Due to the implications of radial-flow angle and end-wall effects, CFD models including the three-hole probes were utilized to replicate data from experiment. The development of this model is presented in section 2.4. Both the plenum and full-inlet configurations were used for comparison. Contours of static pressure, total pressure, Mach number, and swirl angle for the plenum model, plenum model with three-hole probes (THP), and experimental data are presented in Figure 4.12. The contours of static pressure and Mach number clearly illustrate that the three-hole probe CFD and experiment data show significantly improved agreement compared to the normal plenum model case. The shroud Mach number is reduced, and the hub is increased due to the change in static pressure. Furthermore, the normalized total pressure values are lower in the THP CFD case compared to the plenum model by up to 0.2 points. This is an indication that this metric is also not being captured correctly by the probes. The difference in the total pressure

contours from the cobra model and experiment with the plenum model will cause a significant difference in total pressure distortion descriptors, as the deviations in the plenum model are significantly lower in magnitude than the other two cases. This will lead to a significantly lower value of pressure distortion intensity. The difference between the THP model and experiment at BDC in the total pressure contour is due to the ingestion of the ‘dead zone’ from the plenum due to flow not redistributing upstream of the plenum inlet. Swirl magnitude and trends are comparable between all three result sets. This is due to the dependence of the swirl angle on  $C_{YPD}$ , which is only dependent on the differential pressure between the two side pressure taps, which experience comparable radial flow angles and wall effects at most circumferential traverse locations. The contours show the most similarity between the three cases at the mid passage, where radial flow angle magnitude is low and there is a lack of wall effects.

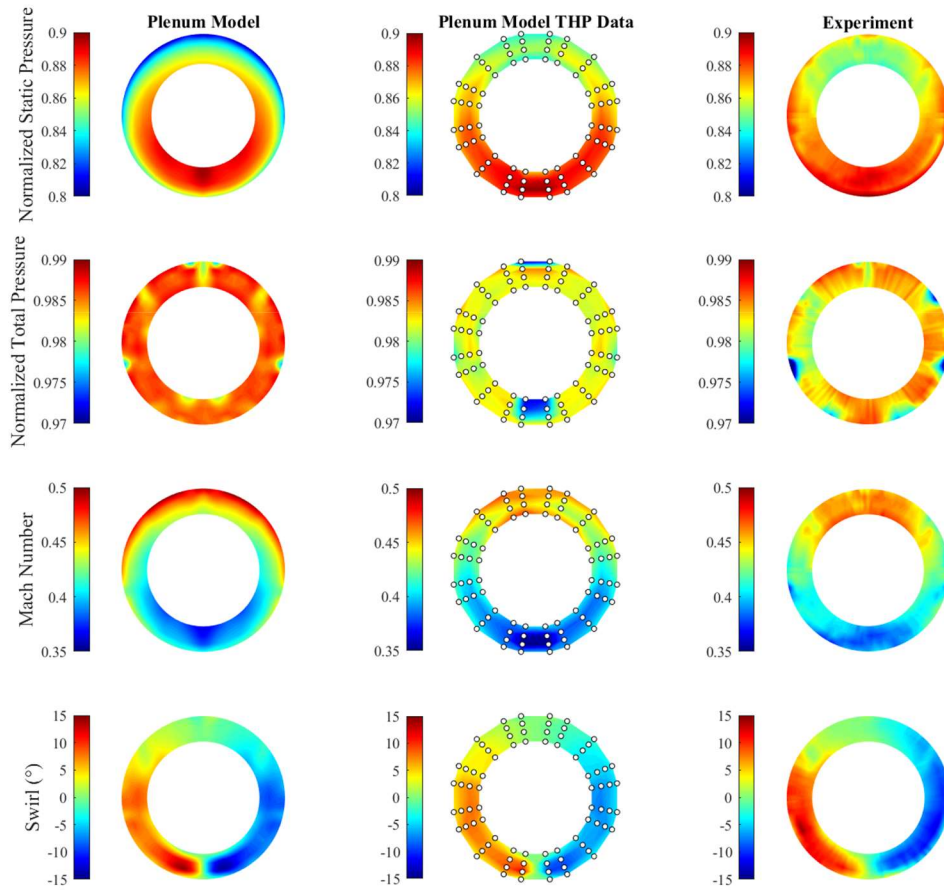


Figure 4.12. Plenum model, plenum model with three-hole probes, and experiment contours in nominal configuration

The same contours that were presented from the plenum model data in Figure 4.12 are provided in Figure 4.13 for the full-inlet model data. The same differences between the full-inlet and THP CFD models with respect to static pressure and Mach number as the plenum model are present. The total pressure from the THP is reduced from the full-inlet model in magnitude and is comparable to experiment values. The BDC total pressure deficit is not present in the full-inlet THP model as it is in the plenum model, because of flow redistribution in the APU elbow upstream of the plenum due to the downstream geometry. However, the total pressure in the annulus is lower in the three-hole probe model compared to the regular model, which will affect circumferential pressure intensity. However, the magnitude of the total pressure variation in the full-inlet model is larger than that of the plenum model and will, therefore, show an increase in pressure distortion intensity. Again, swirl values are not changed by the THP model, and all three cases show reasonable agreement, except for the behavior around  $45^\circ$  and  $135^\circ$  within the annulus, where the CFD models show higher swirl magnitudes than experiment. This is due to the vortex structure along the shroud migrating further into the passage compared to the plenum model.

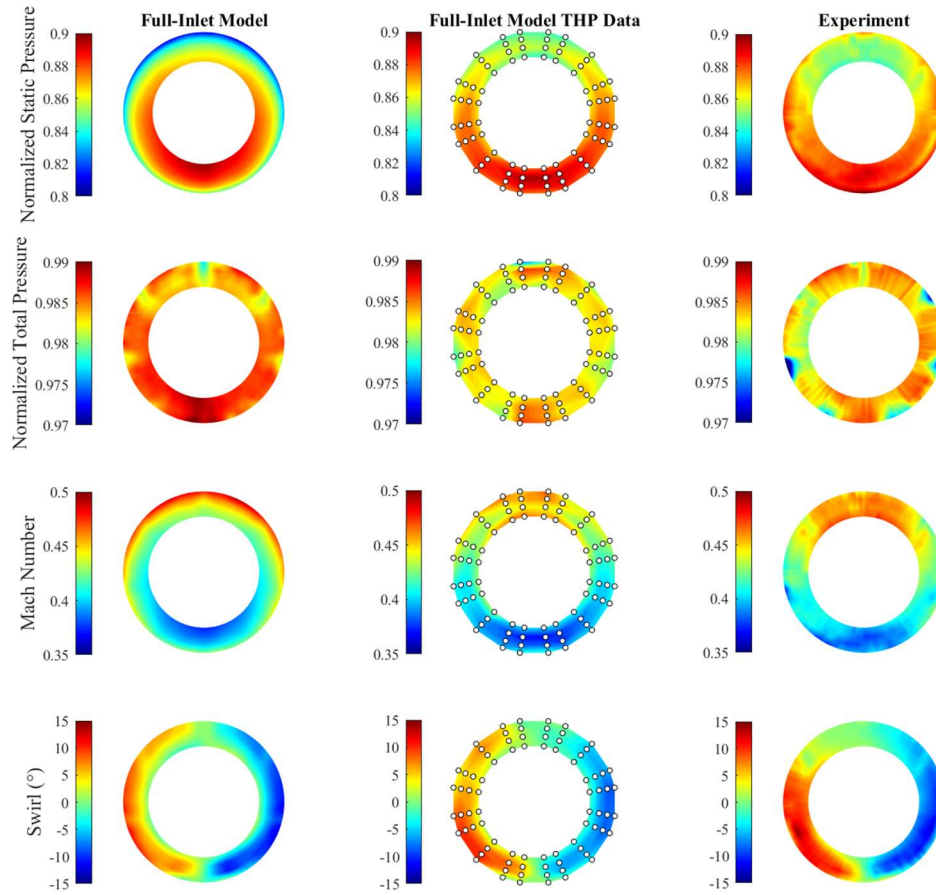


Figure 4.13. Full-Inlet model, Full-Inlet model with three-hole probes, and experiment contours in nominal configuration

The indications from these THP models are that radial flow angle and wall effects are a significant source of error in this experimental setup. Wall effects are generally constant, as they are caused by geometric interference with the flow. However, radial flow angle is heavily dependent on the inlet configuration and can be difficult to predict. Moreover, these effects on the shroud in the nominal configuration are difficult to decouple. These errors also have a significant impact of distortion descriptors, as pressure intensities will be different due to the lower experimental indicated total pressures than is predicted by CFD. Therefore, for comparison of the models with experiment, greater significance should be granted to the mid-passage regions that experience acceptable radial flow angle magnitudes.

## 4.4 Baffle Cases

To determine the efficacy of the reduced model, both plenum and full-inlet model simulations were conducted in seven different baffle configurations at the two selected operating points. These data are compared alongside experiment data utilizing both pressure and swirl distortion indices to define the AIP flow conditions. The different configurations generated varying levels of radial swirl, which impacted experimental data. Apart from an instrumentation notch in the plenum bottom half, the inlet is symmetric. Therefore, for baffle cases, the positive and negative baffles of the same magnitude should produce comparable pressure and swirl intensities. Swirl directivities for equal magnitude baffles should be equal in magnitude and opposite in sign for the CFD data. The only deviation from this behavior for the experiment should be attributed to unsteady pressure fluctuations in the annulus that cannot be captured by the steady response three-hole probes and the radial flow components disrupting measurement accuracy.

### 4.4.1 Radial Flow Angle Considerations

As covered in section 4.3.1, high magnitudes of radial flow angle are detrimental to three-hole probe performance and, therefore, impact the experiment data. To determine the regions where this would be a predominant effect, radial flow angle data from both the plenum and the full-inlet models were extracted. Simulation results for the nominal configuration case and the positive baffle cases at 100% corrected speed in choke are compared in Figure 4.14. In section 4.3.1, the models showed good agreement for the magnitude of the radial flow angle in the nominal configuration. The contours for the positive baffle cases further show that the plenum model can predict annulus flow angles when baffles are installed in the plenum with comparable precision to that of the full-inlet model. The magnitudes are within  $1^\circ$  across most of the annulus area, with variations of up to  $3^\circ$  in minute areas in the wake of struts. The flow characteristics that are captured downstream of the inlet rakes and instrumentation notches are comparable between the two models and show reduced variation in comparison to the strut wakes. Contours of radial flow angle in the negative baffle locations are mirror images of those presented in Figure 4.14 and display comparable magnitudes.

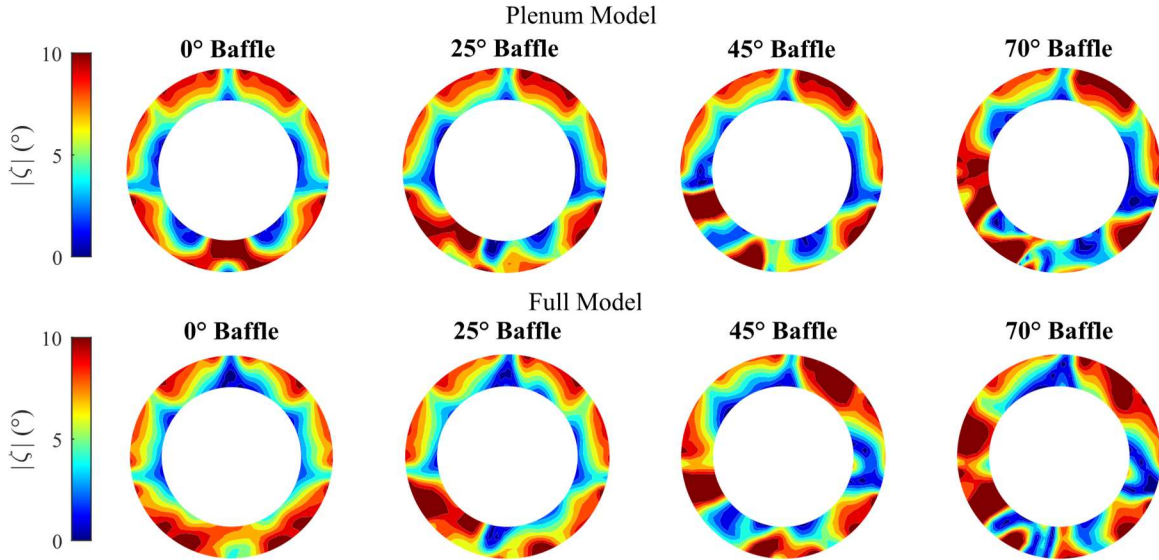


Figure 4.14. Radial flow angles for positive baffle configurations at 100%  $N_c$  from CFD simulations of both models

The larger the deviation of the baffle from BDC is, the more radial the velocity at the AIP becomes. As previously stated, outside of the shroud-side instrumentation ring, the 0° baffle case does not show significant regions where flow is not suitable for THP use. With the 25° baffle installed, a region 45° clockwise of BDC that extends across the entire annulus span becomes fouled by the magnitude of  $\zeta$ . This region is also unsuitable for THP use in the 45° and 70° baffle cases, but additional regions are present in these configurations. A further fouled sector that covers the annulus span is apparent in both cases approximately 25° clockwise of TDC. The 70° case has a third region where THP cannot be used reliably at any span approximately 65° counterclockwise of TDC. These regions that present unsuitable flow for the three-hole probes present a challenge when comparing to experiment data, as the data in these locations are unreliable. Therefore, it is important to note that as the baffle locations deviate further from BDC, the distortion data from CFD may not correlate with that of experiment along the radial instrumentation rings. This is an imperative consideration when comparing distortion descriptor data between CFD and experiment.

#### 4.4.2 Circumferential Total Pressure Distortion

Total pressure readings from three-hole probes are greatly affected by radial flow angle magnitudes, with larger magnitudes causing greater fluctuations in total pressure measurements.

For all off-design baffles, the magnitude of this angle increases from hub to shroud. Therefore, the expected deviation of the circumferential total pressure intensities of the CFD models to experiment should be expected to be lowest on the hub-side probe and highest on the shroud-side. The pressure intensity should also increase with mass flow rate, as the total pressure loss is a function of volumetric flow rate. The calculated circumferential pressure intensity values for the three positive and negative baffle configurations from the two CFD models and experiment are provided in Figure 4.15. It is evident from this figure that the CFD models show better agreement with experiment along the hub and deviate from experiment moving toward the shroud. The intensities for both the models are comparable with one another and the experiment along the hub-side instrumentation ring with the largest deviation in intensity being less than 0.002. The 67% and 84% span from CFD reveal significant disagreement with experiment, indicating intensities up to an order of magnitude lower. As discussed in sections 4.3.4 and 4.4.1, this is expected behavior of the three-hole probes within a region of high  $\zeta$  magnitude. Comparing the results between the full-inlet and plenum model at the shroud, the total pressure intensities are almost identical showing a maximum intensity variation of less than 0.001. This is evidence that for several plenum flow path geometry configurations, the circumferential total pressure behavior is modelled similarly by a reduced plenum model compared to a full-fidelity model. The hub-side intensities also imply this, as both models are comparable with experiment values at this radial location.



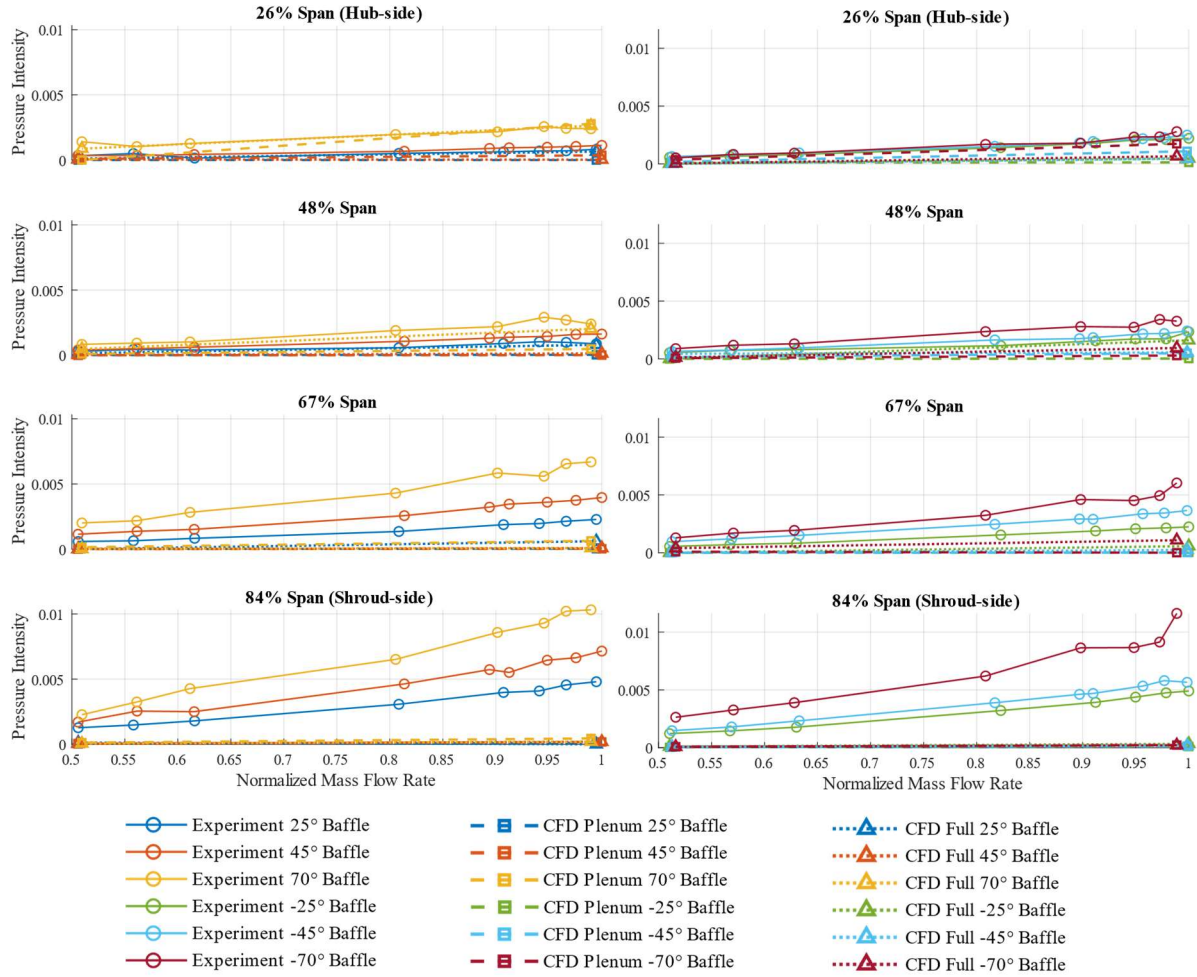


Figure 4.15. Circumferential pressure distortion intensities for all off-design baffles

At 95% and 100% speed, the total pressure intensities from experiment fluctuate significantly, and the fluctuations increase with a larger deviation in installation from BDC. The magnitude of these intensity fluctuations between the  $+70^\circ$  and  $-70^\circ$  baffle reaches up to 0.003 in magnitude, which is significant. This also occurs for the  $\pm 25^\circ$  and  $\pm 45^\circ$  cases with reduced magnitudes. The differences in intensity are an indication of unsteady pressure fluctuations in these cases at high mass flow rates, as these values should be comparable due to inlet symmetry. Further evidence of this is provided by the Kulite total pressure data in Figure 4.16. The maximum unsteady pressure fluctuation for the shroud-side ring is above 4% of the mean flow path pressure. The magnitude of the RMS pressure fluctuation reduces from shroud to hub. This provides further evidence of the impact of unsteady pressure fluctuations on the total pressure readings as the



intensity fluctuations also reduce from hub to shroud. This is an indication that circumferential pressure distortion data from experiment at higher mass flow rates fluctuates more and is also dependent on how aggressive the baffle installation is. These effects will not be captured by a steady CFD simulation, and they contribute to the significant deviation of the CFD results from experiment near the shroud.

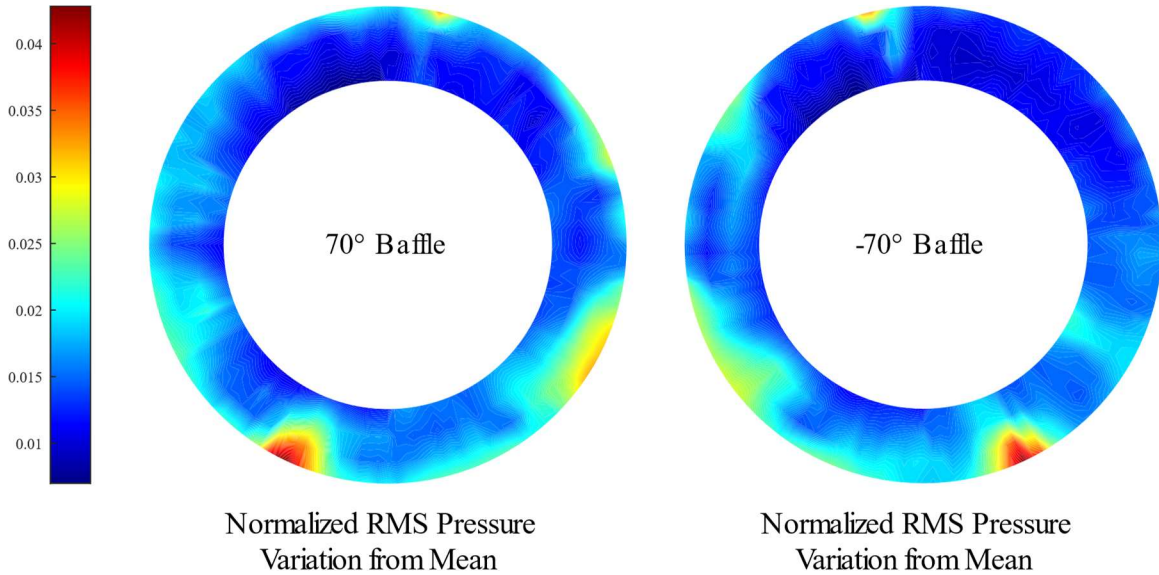


Figure 4.16. Total pressure variation contours from Kulite data for  $\pm 70^\circ$  baffles at 100%  $N_c$  in choke

#### 4.4.3 Radial Total Pressure Distortion

Radial total pressure intensity is an indicator how total pressure varies from the face average at different radial locations. Therefore, for the purposes of comparing the CFD models to experiment and one another, radial pressure intensity is an indication of the trend of the total pressure profile in the annulus. As the models and experiment each have their own face average pressure, the intensity values can be compared as they are effectively normalized. These radial pressure intensities are presented in Figure 4.17. The regions of positive radial pressure intensity represent a lower average ring total pressure compared to the face average for that radial location. Again, along the shroud, the unsteady pressure fluctuations cause disparities between equal magnitude baffles, with the  $70^\circ$  baffle showing radial intensity values 0.001 higher than the  $-70^\circ$  degree case. Despite this, the largest deviation between both CFD models and experiment is around

0.002 points. For the experimental data and the plenum model, the radial pressure intensity at the 67% span radial location is the lowest in magnitude. This is not the case for the full-inlet model, which for several cases shows lowest intensities at either the 48% or 26% span radial locations depending on configuration. Thus, radial pressure distortion for the baffle cases is not affected by the flow effects from the duct for these configurations. The trends in Figure 4.17 are significantly different between models. However, the magnitude of these differences is relatively low, as the change of the baffle installation does not induce a large amount of total pressure loss. The magnitude of the pressure deficit along the shroud increases for more aggressive baffle installations, with the radial intensity values of the  $\pm 70^\circ$  baffles being approximately twice that of the  $\pm 25^\circ$  baffle configurations at all radial locations. The main purpose of these baffles was to generate different swirl intensities and directions and it appears that the impact on the radial total pressure distortion is not extreme. Therefore, for generation of swirl distortion without incurring major pressure distortions within the annulus, baffles are an ideal selection.

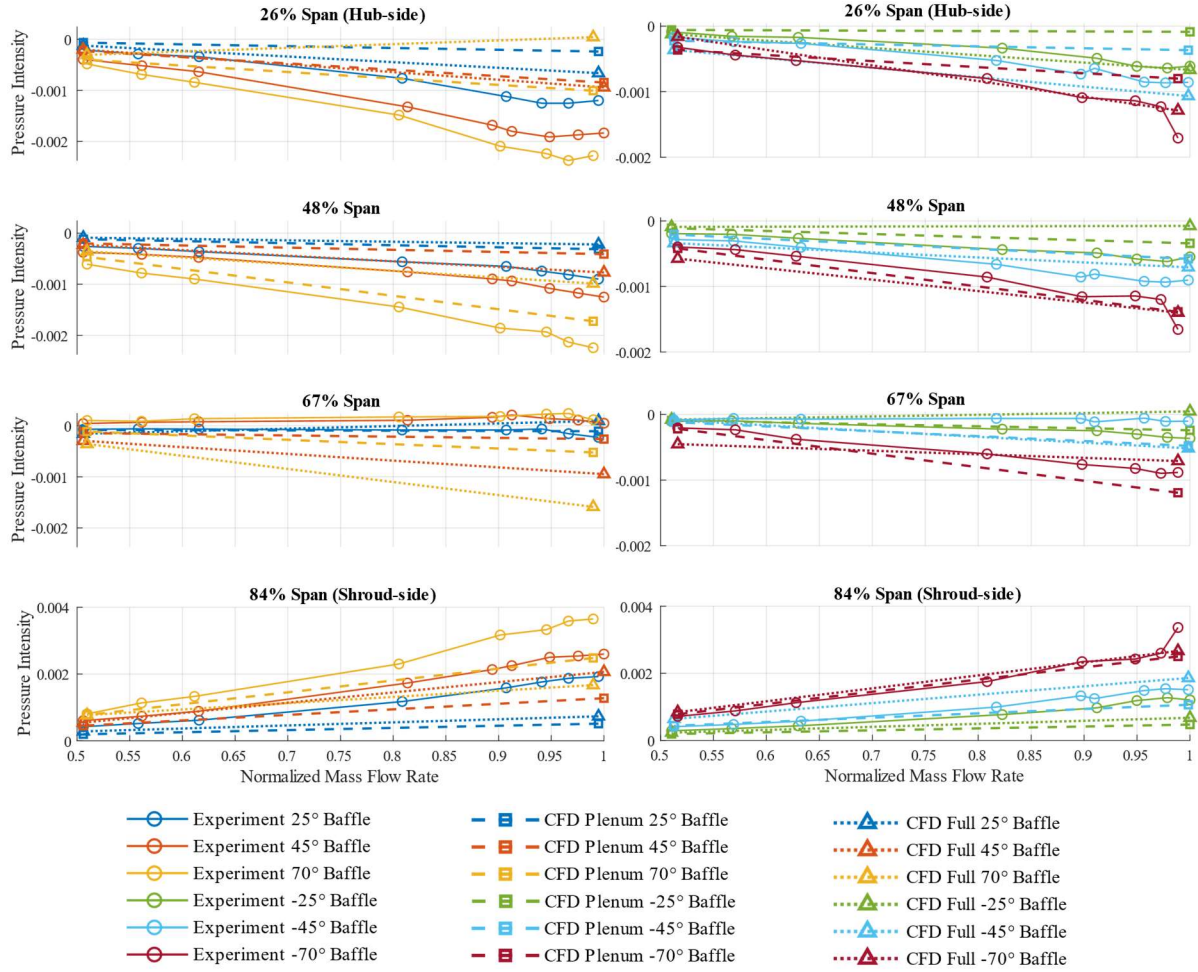


Figure 4.17. Radial pressure distortion intensities for all off-design baffles

#### 4.4.4 Swirl Characteristics

Swirl intensities for the plenum model, full-inlet model, and experiment were calculated to compare the circumferential flow angle in the annulus. Graphs of these values for the off-design cases are shown in Figure 4.18. In both the negative and positive baffle cases, the location of best agreement between experiment and the CFD models is the 48% and 67% span locations. This indicates that the radial flow angle does not have a dominant effect on these readings, but rather, end wall effects are the dominant factor for the swirl reading. Three-hole probes were shown in section 4.3.4 to be effective at accurately capturing circumferential swirl angles in flow regimes where radial flow magnitudes are around  $10^\circ$ . Therefore, the swirl intensities between experiment and CFD data should be comparable at the midspan locations where radial flow angles are lower

and wall effects are negligible. At these radial locations, the maximum deviation of the plenum model from experiment occurs with the +25° baffle at the highest mass flow rate with a magnitude difference of less than 2°. The full-inlet model shows larger differences with experiment, particularly with the +70° baffle where the swirl intensity was more than 2° lower than the experiment value at 100% speed. This suggests that CFD is overestimating the effects of mixing from the APU duct on the lower momentum flow entering annulus, as this portion of the flow is biased towards the hub.

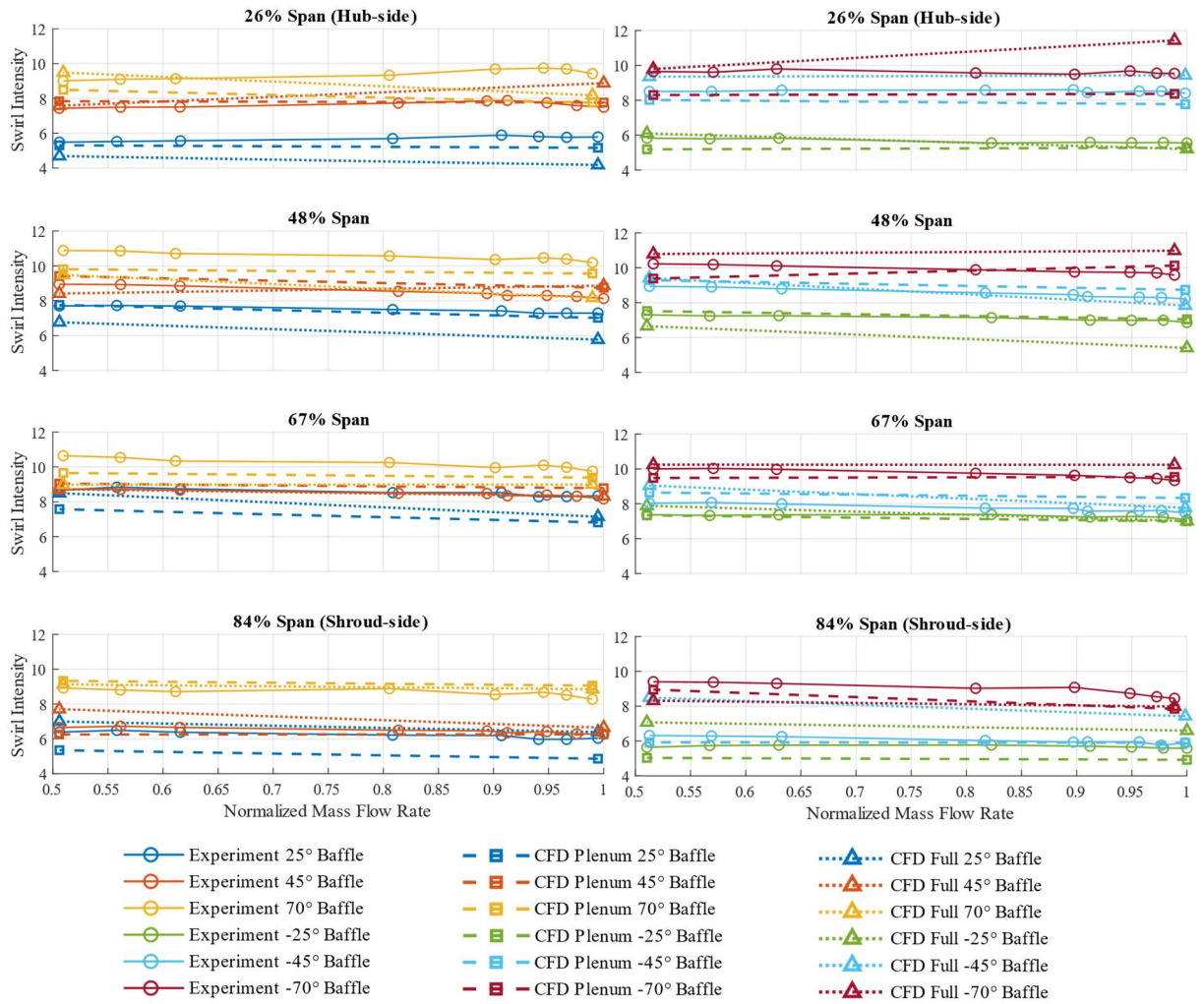


Figure 4.18. Swirl intensity for all off-design baffles

The swirl magnitude of the plenum model at all radial locations shows very little variation with changes in mass flow rate. The full-inlet model is more affected, with changes of up to 3° in

swirl intensity. This key difference indicates that the plenum model is more robust when it comes to capturing the magnitude of the swirl angle within the annulus as experimental data shows only a minor reduction in swirl intensity as the mass flow rate is increased. Furthermore, the plenum model swirl intensity is closer in magnitude to the experiment in most configurations and speeds.

Not only the magnitude of the swirl, but the bulk direction must be analyzed to compare the behavior of the models. Swirl directivity is the key parameter to be scrutinized to understand the direction of circumferential fluid motion. Figure 4.19 presents the swirl directivity values for all off design baffles as a function of mass flow rate.

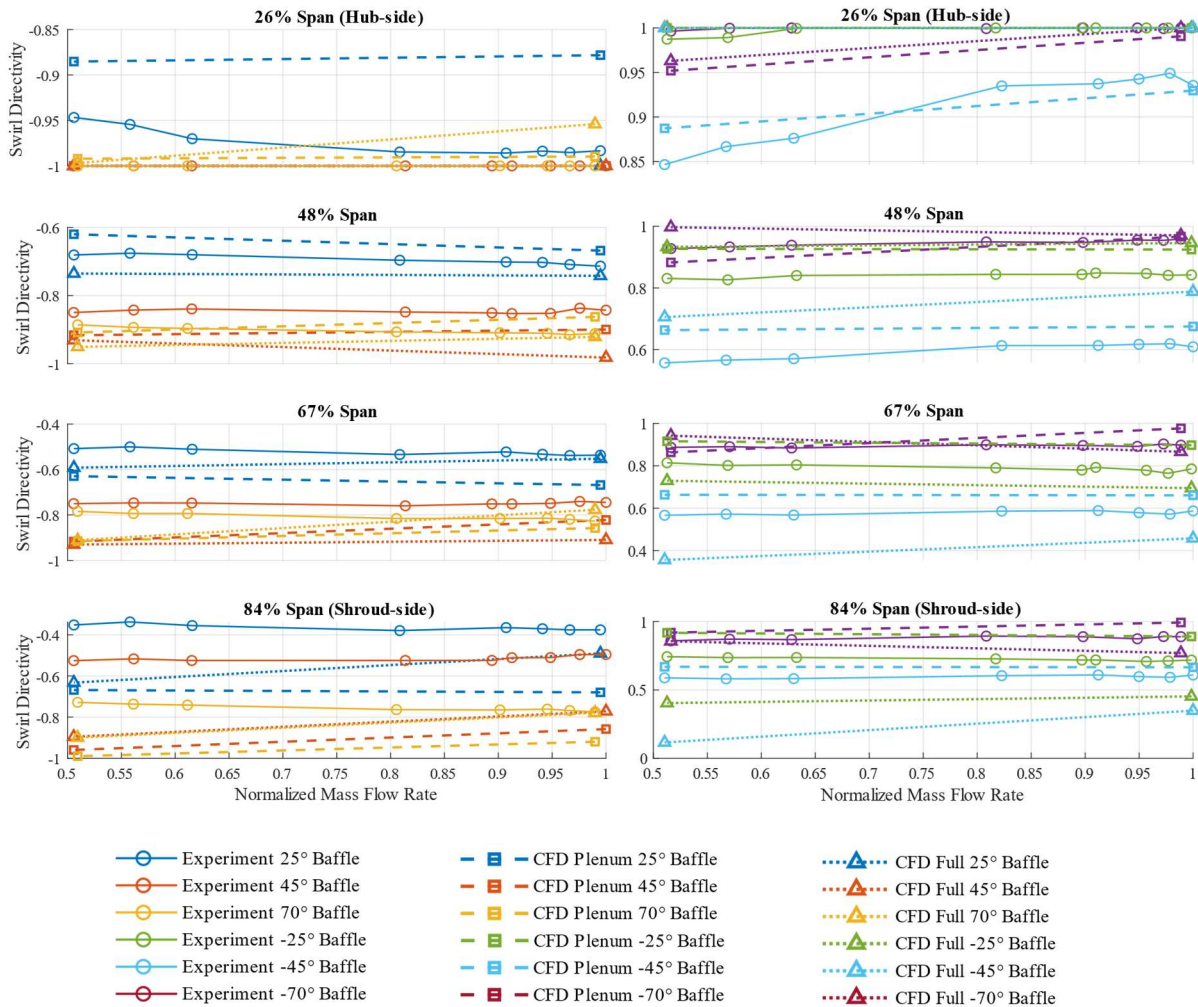


Figure 4.19. Swirl directivity for all off-design baffles



The positive baffles generate counter-swirl, giving them a negative directivity with the opposite being true for negative baffles. For the models and experiment in all configurations, bulk-swirl is generated along the hub with directivity values of approximately -1 for the positive baffles and +1 for the negative baffles. It is logical that the best agreement is achieved along the hub, as it is the region of the annulus that is least perturbed by upstream inlet components, as proved in section 4.2, and experiences the least radial flow. Moving from the hub towards the shroud, the directivity values for each case begin to differ from one another as flow disturbances due to these inlet components take effect and the magnitude of the radial flow angle increases. Again, like the experiment, the plenum model shows little sensitivity to changes in mass flow rate. The full-inlet model swirl directivity shows greatest disparity between the plenum model and experiment along the shroud at lower mass flow rates. This is a further indication that the flow structure from the elbow in the plenum is not washed out in the full-inlet CFD simulations as it is in experiment. It also heavily suggests that the inlet duct has very little effect on swirl structures in the annulus and that the plenum is the dominant component that dictates annulus swirl behavior.

## **4.5 Blocker Plate Cases**

Along with the baffle cases, simulations modelling the four different blocker plates at the two selected operating points were conducted. Total pressure data at the sandwich pack are compared between the models and experiment. Configurations that experience high radial flow angle magnitudes are also identified. Furthermore, pressure and swirl distortion descriptors are used to provide insight into if the models accurately capture the flow field at the AIP.

### **4.5.1 Sandwich Pack Flow Conditions**

To determine if the uniform total pressure deficit at the SPIP of the plenum model with blocker plates is comparable to the full-inlet model and experiment, the total pressure data at the SPIP are compared. Comparing the magnitudes at each sandwich pack rake element will determine if sufficient flow mixing losses upstream of the blocker plate can occur with a simple inlet extension. To increase the resolution of the total pressure deficits, the analysis in this section is conducted on the 100% corrected speed in choke cases as higher total pressure deficits are incurred at larger mass flow rates. The total pressure data were extracted for both the left and right 25% and

50% blockage plates, with the former being presented in Figure 4.20 alongside experimental data. The full-inlet model shows a less uniform total pressure deficit zone behind the blocker plate than both the plenum model and experiment. Despite this, the magnitude of loss in stagnation pressure is comparable with experiment. Within the region that is not blocked upstream, the full-inlet model shows a slightly more comparable contour pattern in total pressure to the experiment. The high momentum jet along the outer wall of the elbow is represented in both experiment and the full-inlet model. However, the magnitude of total pressure loss along the inner wall of the elbow is not captured by the full-inlet model at the SPIP, because the magnitudes of the pressure on the forward side of the SPIP are different by almost one point for the left 25% blockage case. The plenum model shows a near uniform total pressure profile in the unblocked regions due to the flow entering the inlet parallel to the SPIP with no flow angularity. Even though the jet region does not develop in this case, the magnitude of total pressure loss is accurate to within 1 point of normalized stagnation pressure.

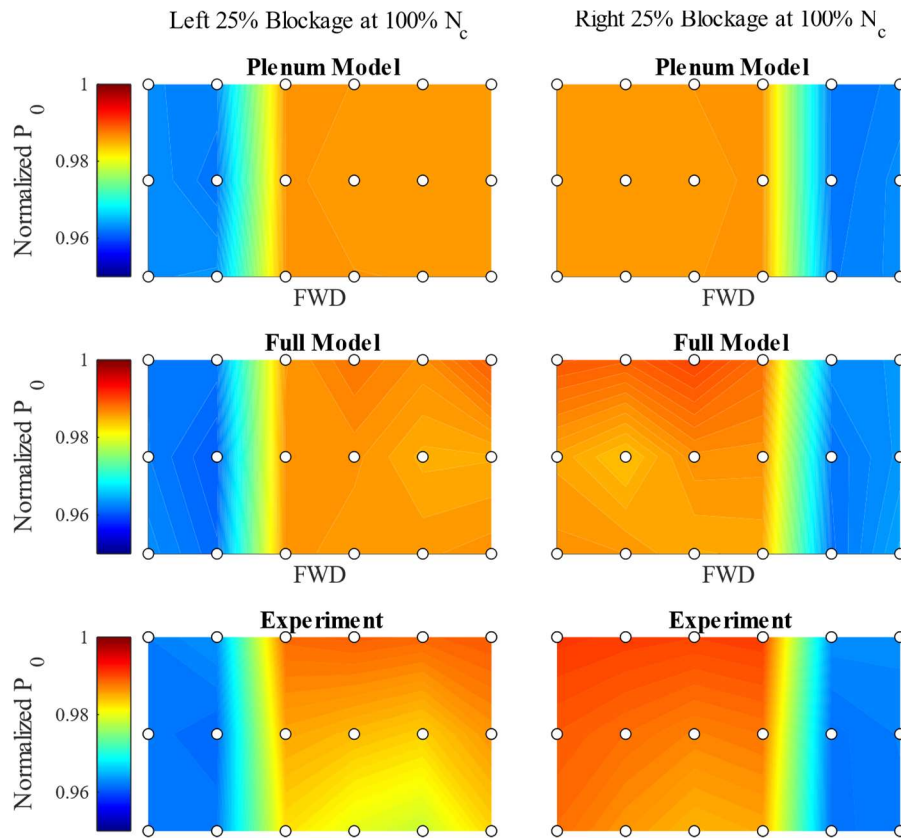


Figure 4.20. Sandwich pack total pressures for 25% blockage plate configurations at 100%  $N_c$ .

As with the 25% blockage cases, data from the 50% blockage case simulations using the two CFD models are presented alongside experiment data in Figure 4.21. The total pressure loss within the obstructed region is almost twice that of the 25% blockage cases. The larger blockage also breaks down the jet structure for the full-inlet model as the pressure data in the unblocked region are comparable to the plenum model in both magnitude and trend. However, experimental data indicate that flow downstream of the blocker plate still shows remnants of the wake formed by the jet along the forward side of the passage. Within the blocked regions, both the plenum and full-inlet model underestimate the loss behind the plate by approximately 1 point for the plenum model, and 2 points for the full-inlet model. This is a surprising finding, as the plenum model flow does not contain the flow angularity components induced by the preceding inlet duct and should, therefore, incur less loss. Furthermore, the plenum model shows a similar trend to the experimental data where the total pressures behind the blocker plate are close to uniform. This is not the case for the full-inlet model, where there is a region of less loss in the corner where the sidewall with the blocker intersects the forward wall. This region is present in the experimental data and plenum model data but the magnitude changes between this rake element and the rest of sandwich pack total pressures behind the blocker plate is less than half a point. Therefore, the trend of the total pressure profile at the SPIP behind the blocker plate is captured by both models, but the magnitude of the loss is captured more accurately by the plenum model. This provides justification that the addition of an inlet extension for flow to adjust to a large obstacle at the inlet of the plenum is effective and provides comparable results to the experiment.



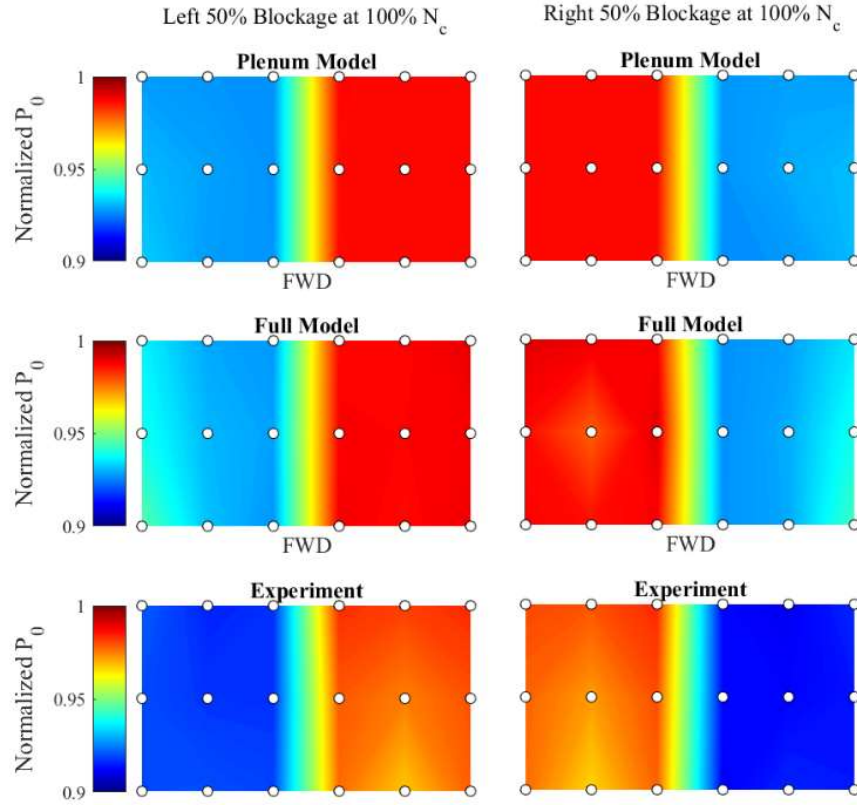


Figure 4.21. Sandwich pack total pressures for 50% blockage plate configurations at 100%  $N_c$

#### 4.5.2 Radial Flow Angle Considerations

As with the baffle cases, it is important to note locations of high radial flow angle magnitudes in the annulus for different blockage plate cases. The radial flow conditions in the annulus for the 25% and 50% left blockage cases from both inlet models is presented alongside data from the nominal configuration in Figure 4.22. From these contours, it is evident that radial flow angle magnitudes are significantly larger for both blocker plate cases than even the most aggressive baffle installations. More of the annulus is fouled than is not for the 50% blockage cases, with only the hub-side element experiencing levels of  $\zeta$  below  $10^\circ$  in magnitude. Furthermore, the plenum and full-inlet models show a much larger disparity for the 25% blocker plate case than for any baffle case. This was also evident in the sandwich pack total pressure data, as the jet-wake structure formed in the  $90^\circ$  elbow progressed into the plenum in this configuration. Unlike in the baffle configurations, this did not washout upstream of the annulus and represents the difference in radial flow angle for the 25% blockage cases. The behavior indicates that vortex

structures do not form as strongly in the full-inlet case behind the blocker plate when compared to the plenum model as the radial flow angles are significantly smaller in this region. The disparity between these two should be evident in distortion descriptors when compared to both one another and experiment for the 25% blockage cases and could be significant. This behavior, however, does not appear in the 50% blockage cases as the jet-wake from the elbow is mostly broken down at the SPIP due to mixing upstream of the blocker plate. This was shown in the SPIP total pressure data. Thus, the radial flow pattern and magnitudes are comparable between the two models in this configuration. Despite the differences between the models in the 25% blocker plate cases, it remains that significant portions of the annulus do not provide a flow structure conducive to being accurately resolved by three-hole probes. This is a concern, as the CFD model distortion descriptor data may deviate significantly from the experimental data due to this added source of error.

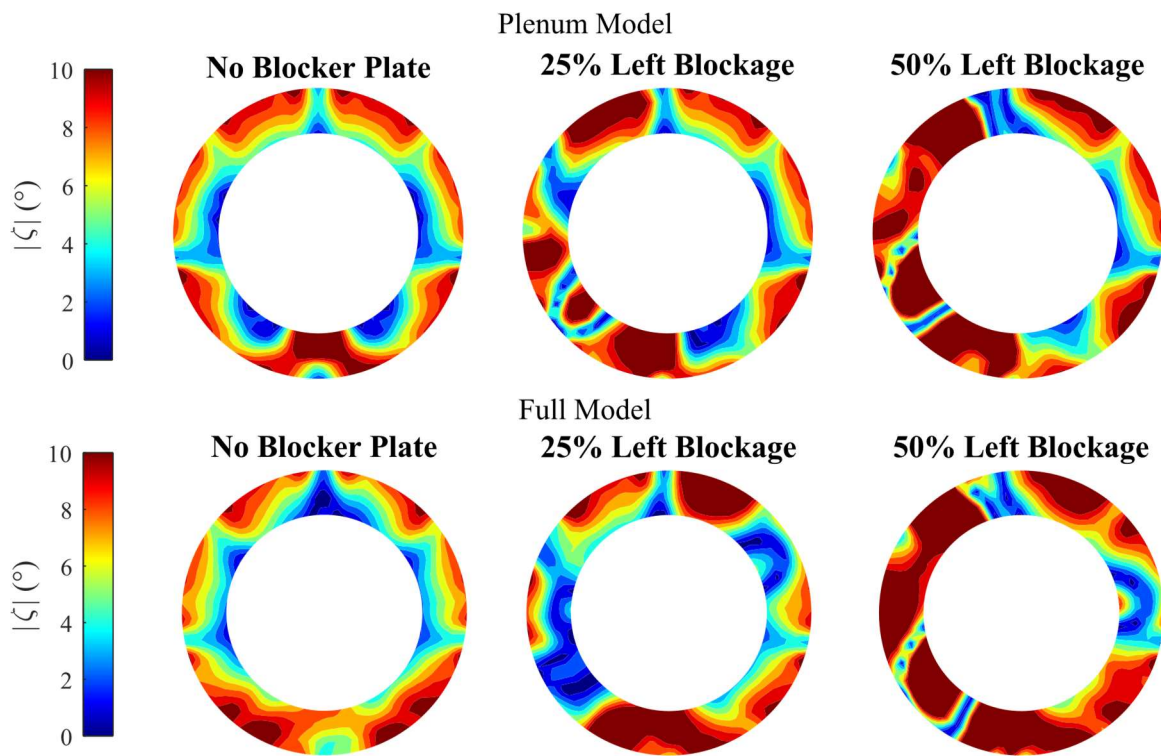


Figure 4.22. 0%, 25% and 50% left blockage plate configuration flow angles

### 4.5.3 Circumferential Total Pressure Distortion

In comparison with the baffle configurations, the total pressure distortion is significantly increased in magnitude for the blocker plate cases due to mixing losses induced by the abrupt flow path change upstream of the plenum. The complex mixing at the inlet to the plenum because of the blockage plate induces significant secondary flow patterns everywhere within the plenum due to flow redistribution. Unlike with the baffle cases, this redistribution also occurs in the high momentum region of the plenum in the top half, and thus, more total pressure loss is accrued. The circumferential pressure intensities for the four blockage plate configurations are provided as a function of mass flow rate in Figure 4.23, and they indeed show significantly more loss than the baffle cases. The severity of circumferential pressure intensity is an order of magnitude larger than the most severe baffle cases for the hub-side ring and more than three times larger for the shroud-side. The difference in intensity values between the CFD models and experiment is also larger than the baffle cases, with the largest intensity difference from experiment being approximately 0.01. However, if a normalized intensity difference is considered, these models do perform much better than the baffle cases. The intensity values of the plenum model are of comparable magnitude with the full-inlet model. This indicates that the jet structure that is not broken up in the 25% blockage plate cases has a negligible effect on the total pressure loss within the plenum.

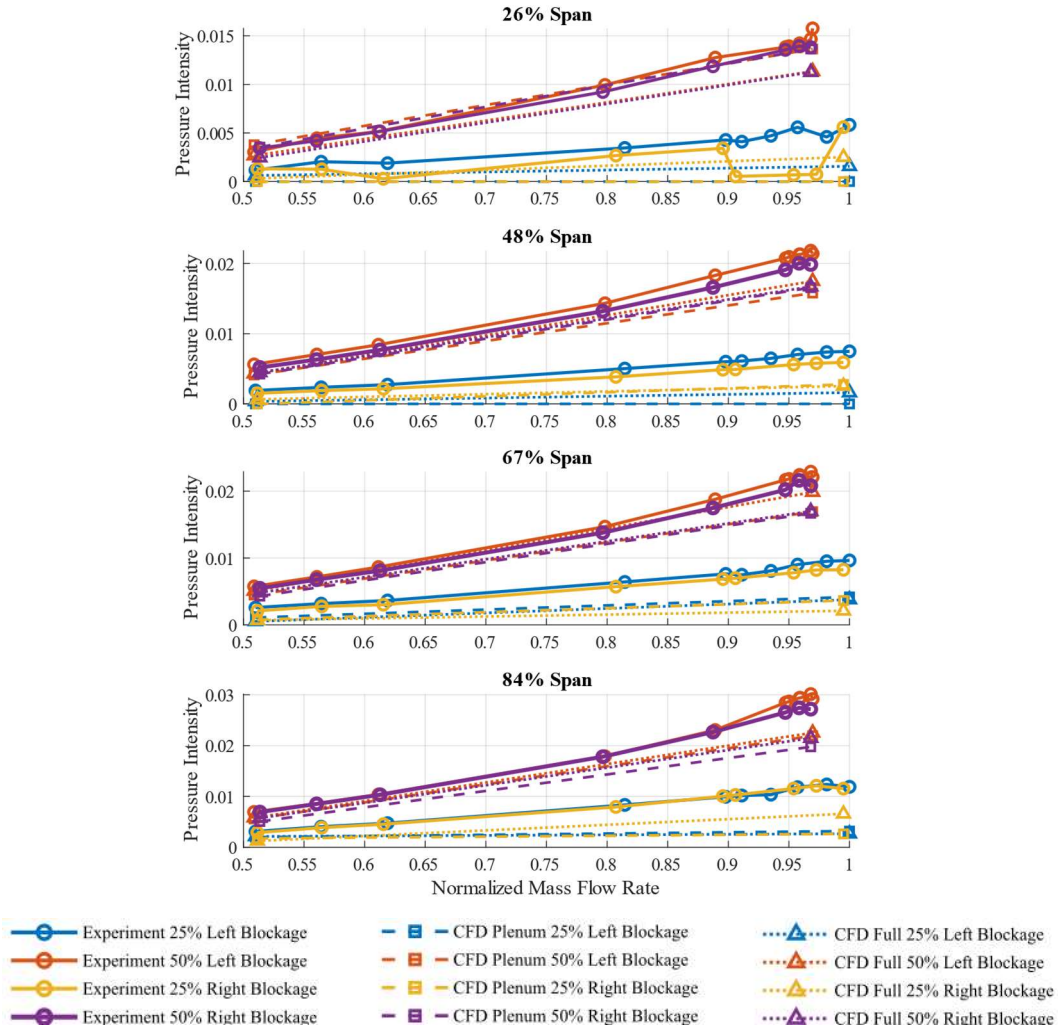


Figure 4.23. Circumferential pressure distortion intensities for all blocker plate configurations

The same trend of CFD matching the experimental hub intensities the best, with the differences between intensities increasing as the span of the probe decreases. This was also experienced with the baffle simulations. This is a direct consequence of the significant magnitude of radial flow angle across the entire annulus as the increase in angle generates larger total pressure loss within the probe. A new development with the blocker plates, however, is the fluctuation of pressure intensity at high mass flow rates along the hub that is observed in all configurations. Previously, the baffle cases experienced these fluctuations predominantly along the shroud. However, the blocker plate configurations have this at all radial locations at high speed, with intensity fluctuations between the similar geometry blockage plates of up to 0.005. This is indicative of a much larger unsteady pressure field that extends further towards the hub. The Kulite

data from the left blockage plates at 100% speed at choke were extracted and the RMS pressure variation, and these are provided in a contour form in Figure 4.24. The magnitude of variation is over 5% of the mean face pressure value for the 50% blockage case and up to 4% for the 25% blockage case. This variation for the 50% blockage configuration extends further towards the hub than in the baffle cases, with a maximum value of variation around 3% at the hub. This is a significant change in pressure and would result in a large variation in total pressure readings by the steady three-hole probes. The experimental intensity behavior of the 25% right blockage plate along the hub shows another repercussion of the unsteadiness of the pressure fluctuations. The intensity value changes drastically not necessarily due to large fluctuations of the pressure value, but rather the change in extent that the pressure deficit covers. If the extent value is close to the critical angle but no longer meets the same critical angle criteria as a neighboring point, then there is a significant alteration in the total pressure intensity. This is an obstacle presented by implementing the critical angle criteria as recommended by SAE international in Gas Turbine Engine Inlet Flow Distortion Guidelines (2017).

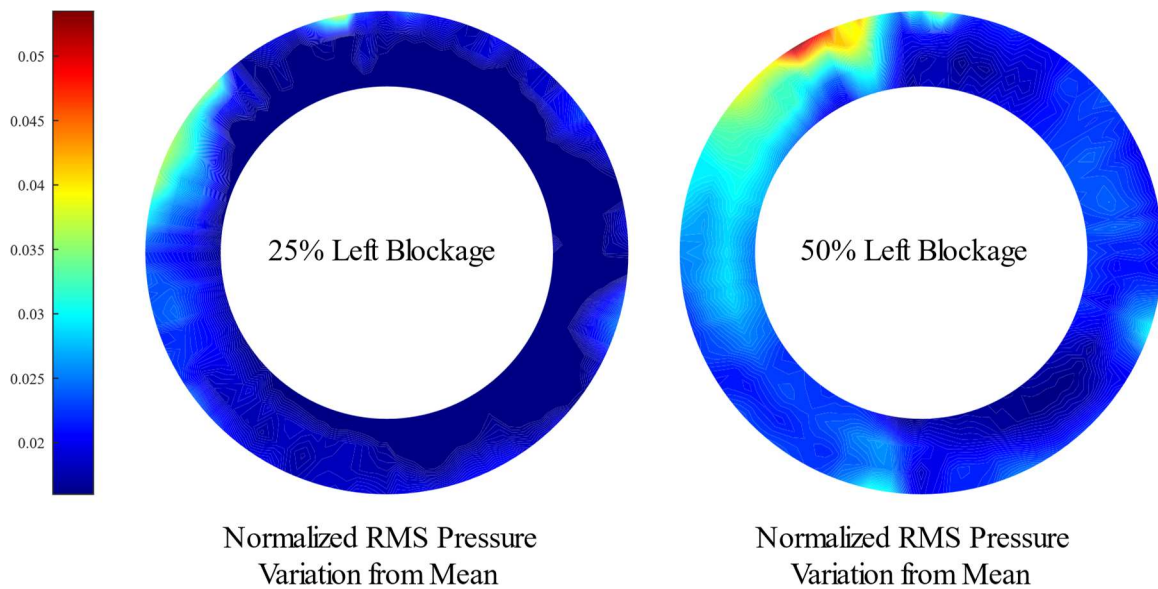


Figure 4.24. Total pressure variation contours from Kulite data for left blockage plates at 100%  $N_c$  in choke

#### 4.5.4 Radial Total Pressure Distortion

As with the circumferential distortion intensities, the radial distortion intensities are significantly larger in magnitude for the blocker plate configuration when compared to the baffle cases. The radial pressure intensities for the blocker plate configurations are presented in Figure 4.25 and show similar behavior to the baffle cases in terms of the sign of the intensity value. The shroud-side has a large positive intensity indicating that the largest total pressure deficits in the annulus are located along the shroud. The 67% span ring shows a near zero value with the 48% and 26% span rings showing decreasing intensities indicating regions of higher total pressure. The hub-side intensity values are approximately four times larger than the baffle cases and the shroud-side distortion is twice as severe.

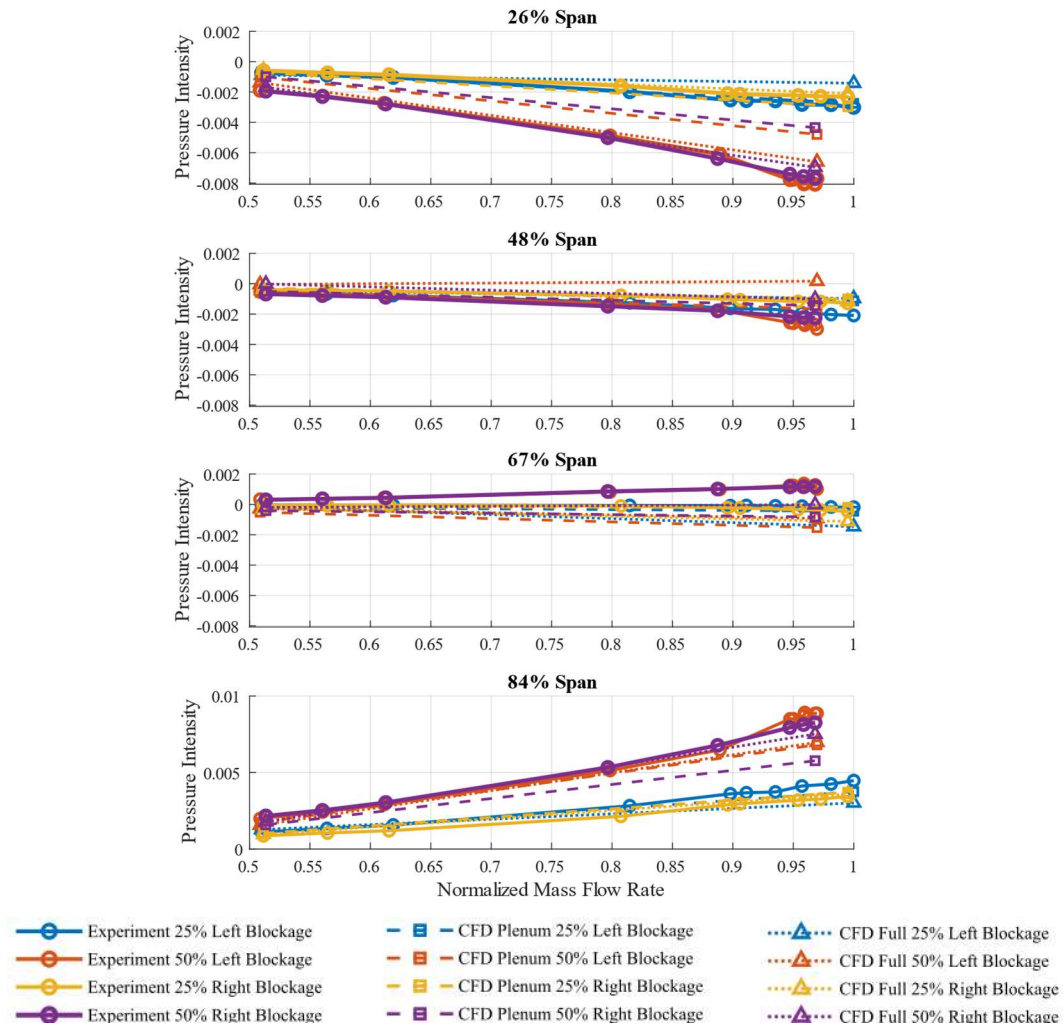


Figure 4.25. Radial pressure distortion intensities for all blocker plate configurations



At all spans, the CFD models predict lower radial intensities than experiment, which is expected due to the circumferential pressure intensities that were previously presented. The full-inlet and plenum model radial intensity values are all within 0.001 of each other except for the hub-side ring for the 50% blockage case. This agreement for these two models is almost identical to that observed for the baffle cases. The largest error at the 50% blockage cases at the highest mass flow rate is approximately 0.002 points, which is higher than the maximum for the baffle case but is an isolated location of disagreement. On a normalized basis, the difference between the full-inlet and plenum model pressure intensities is significantly lower for the blocker plate installations compared to the baffle geometries. Considering the blockage plates significantly perturb the flow entering the plenum and cause significant mixing, the ability of the plenum model to accurately capture the radial distortion intensity is impressive. This implies that the locations of pressure deficit regions are captured in the same manner as the full-fidelity model.

#### **4.5.5 Swirl Characteristics**

The flow angularity within the annulus of the blocker plates configurations is complex and the magnitudes of the flow angles are large, as illustrated in 4.5.2. The flow field is also highly unsteady due to the mixing of wakes from the blocker plate with the numerous inlet components. This presents a modelling challenge as well as experimental steady data measurement issues. Figure 4.26 shows the swirl intensity values for the two CFD models and experiment as a function of mass flow rate. Unlike the baffle cases, the CFD intensities vary significantly from the experimental values with a maximum difference observed at the 48% span location for both models, with the swirl intensity value being  $4^\circ$  lower than experiment. At this location, the intensity values of both models are comparable. At the 67% span, however, the intensity for the full-inlet and plenum model are higher than experiment. This indicates that the vortices in the annulus for the computational models are located slightly closer to the shroud than indicated in experiment. The SI values of the 25% configurations for the plenum model are unchanged with increased mass flow rate at every span, and the trend is similar for the 50% configurations. This behavior is also true for the full-inlet model except for the shroud-side ring, which ingests more of the higher momentum flow. This suggests that the full-inlet CFD model is not accurately capturing the mixing of the high energy flow in the top-half of the APU plenum. Between the left and right 50% blockage cases for the experiment, the swirl intensity difference is about  $2^\circ$  on the hub and

shroud from one another. However, if the intensity is averaged from all span values, this number is similar. This suggests that there is unsteady movement of the secondary flow structure within the annulus as the overall average swirl intensity is equal but is different locally.

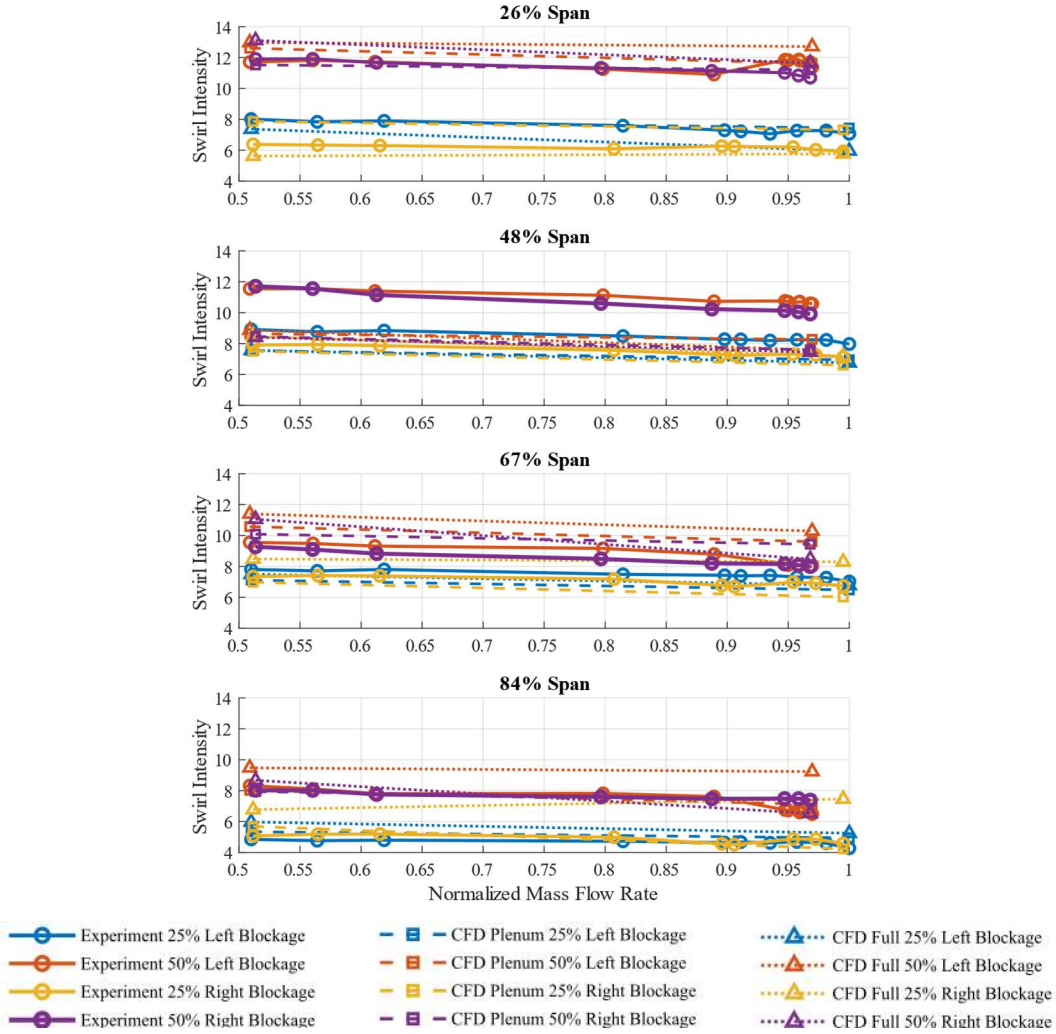


Figure 4.26. Swirl intensity for all blocker plate configurations

Generally, the plenum model data show better agreement with experiment at higher mass flow rates, which was not the case for the baffle configurations where the difference was of a more constant magnitude. Furthermore, the experimental data show a decrease of approximately  $1^\circ$  in swirl intensity with an increase of mass flow rate at 80% speed for all blockage plate cases at all spans. This can be attributed to the operation of the compressor influencing the upstream flow



field. At 80% speed, the impeller experiences inlet stall at the inducer downstream of the rotatable rakes, creating a region of low momentum flow. This can be determined using experiment inducer shroud temperature data, as the lower momentum flow has a higher temperature due to heat transfer from the impeller passage during recirculation. Figure 4.27 shows the compressor speed lines with the 25% and 50% left blocker plate installed. The data points are colored according to the inducer shroud temperature normalized by the average inlet strut total temperature value. At 80% speed out of choke, the temperature at the inducer shroud is increased indicating inlet ring stall at the inducer. This did not have an influence on the baffle configuration cases but interestingly, does on the blocker plate cases. The potential cause for this is that the flow momentum in certain sectors of the annulus is greatly reduced by the total pressure deficit caused by the blocker plate that is not present for the baffle configurations. These regions of low momentum are impacted by the potential caused by the high-pressure stall cells at the inducer and the flow structure changes to adjust.

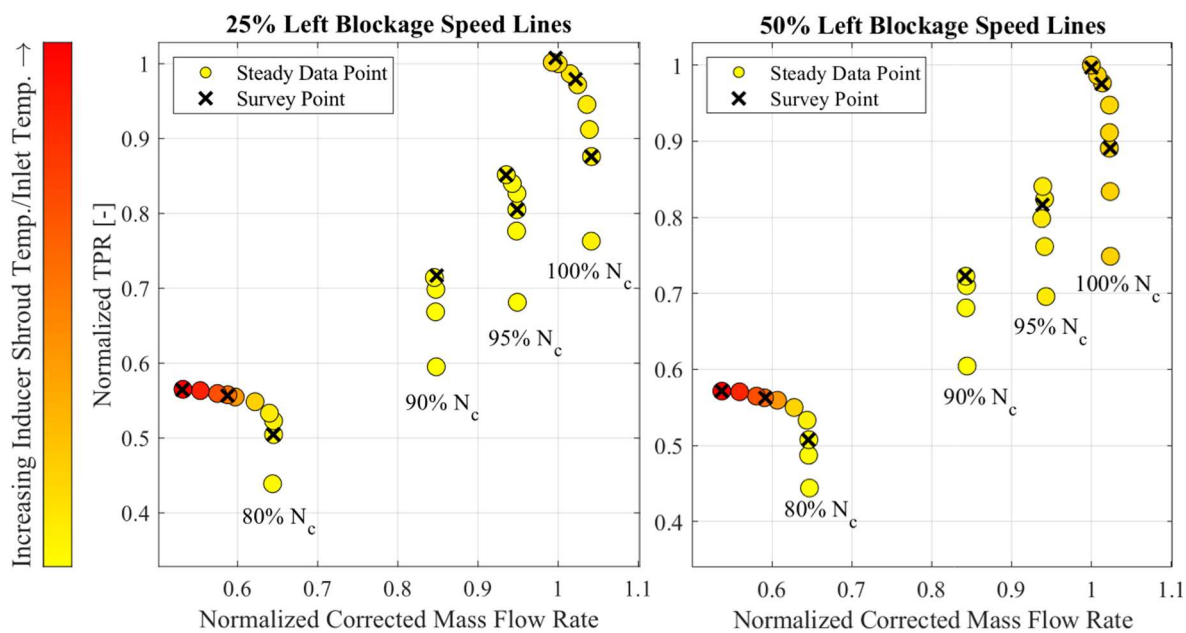


Figure 4.27. Left blockage plate speed-lines colored by normalized shroud temperature upstream of inducer

The swirl directivity numerics highlight the benefits of the plenum model for the blocker plate configurations. Graphs of these values are presented in Figure 4.28 and show a large disparity

between both models and with experiment. The full-inlet model indicates significant changes of directivity and even the sign of the directivity with changes in mass flow rate. This is not apparent in either the experiment or plenum model data. For every configuration and at every span, the plenum model and experimental data do not change sign to move from co- to counter-swirl or vice versa.

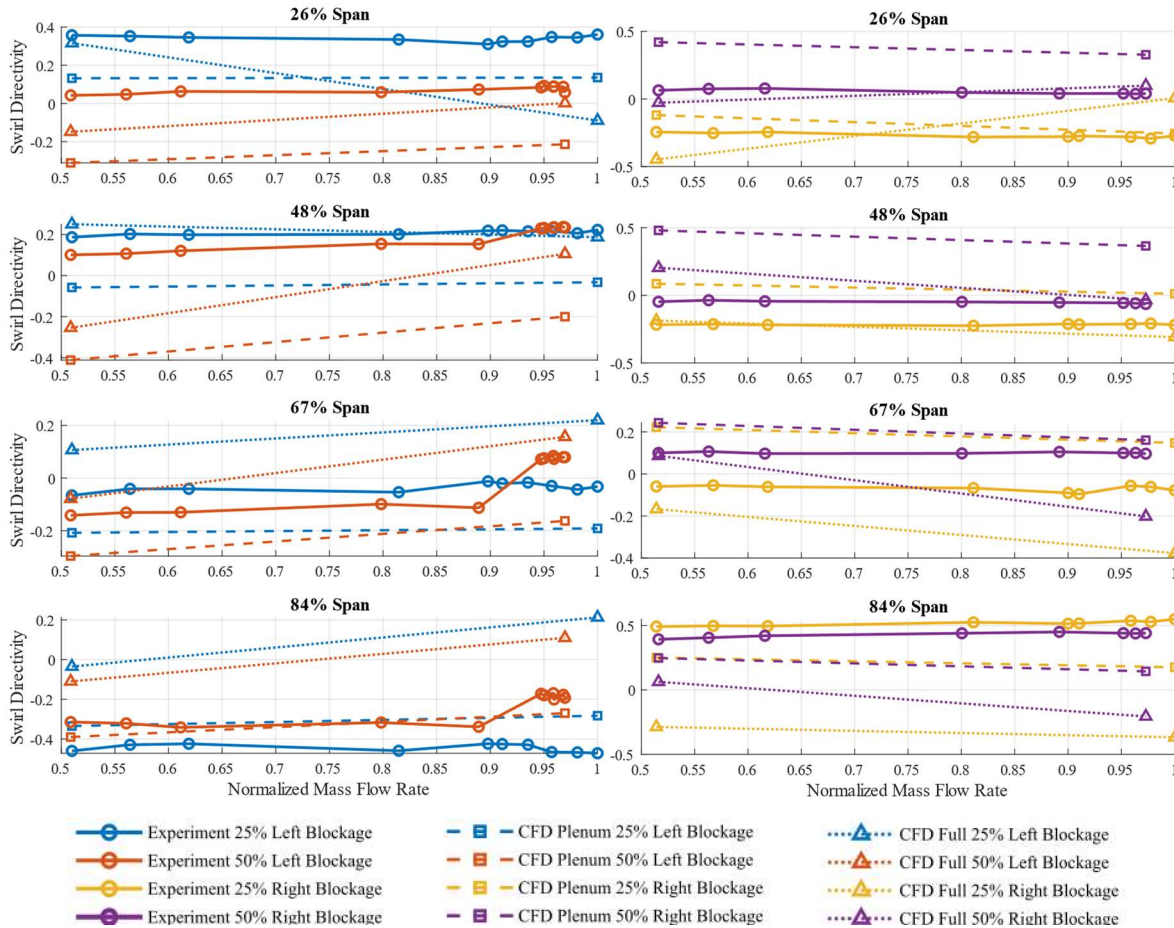


Figure 4.28. Swirl directivity for all blocker plate configurations

The 25% blockage plates have the most significant variation in directivity for the full-inlet case. In these configurations, the sandwich pack total pressure data indicated that the jet structure from the elbow did not break down in the full-inlet model, whereas it did for the 50% blockage cases. Figure 4.29 provides swirl contours in the 25% left blockage configuration for both mass flow rates simulated. It is clear from these contours that the plenum model and experiment are not the same in magnitude or direction everywhere, as the plenum model has more areas of counter-swirl

than experiment. However, what is common between them is that they are not considerably affected by the increase in mass flow rate, as the contours from the two different operating conditions are almost identical. The general swirl structure between the full-inlet and plenum models are similar apart from the shroud-side flow. However, for the full-inlet model, the region of high co-swirl in the top left sector along the hub migrates towards the shroud at the higher mass flow rate. A potential cause of this is indicated by the migration of swirl intensity values of the 50% blockage plates at 100% speed. This may be an unsteady phenomenon and the timescale of the steady simulation could allow this behavior to be picked up. This is further verification that the APU inlet duct flow is not being mixed out within the plenum in the full-inlet simulations and is the cause of the change in the sign of directivity. The low mass flow plenum structure and full-inlet structure show the best agreement. Furthermore, the regions that show the biggest disparity in swirl values with experiment are areas of high radial flow angle as previously outlined in Figure 4.14. Therefore, the plenum model flow swirl behavior should be considered closer to reality than both the full-inlet and experiment from a steady flow perspective. The full-inlet mixing does not match what is expected from experiment, and the experiment swirl values in the high  $\zeta$  magnitude regions greatly change the swirl distortion descriptors. The full-inlet simulation, however, does lend strength to the potential of an unsteady migration of vortices in the annulus. Furthermore, the location where the vortex moves in Figure 4.29 coincides with the region of high total pressure fluctuations.

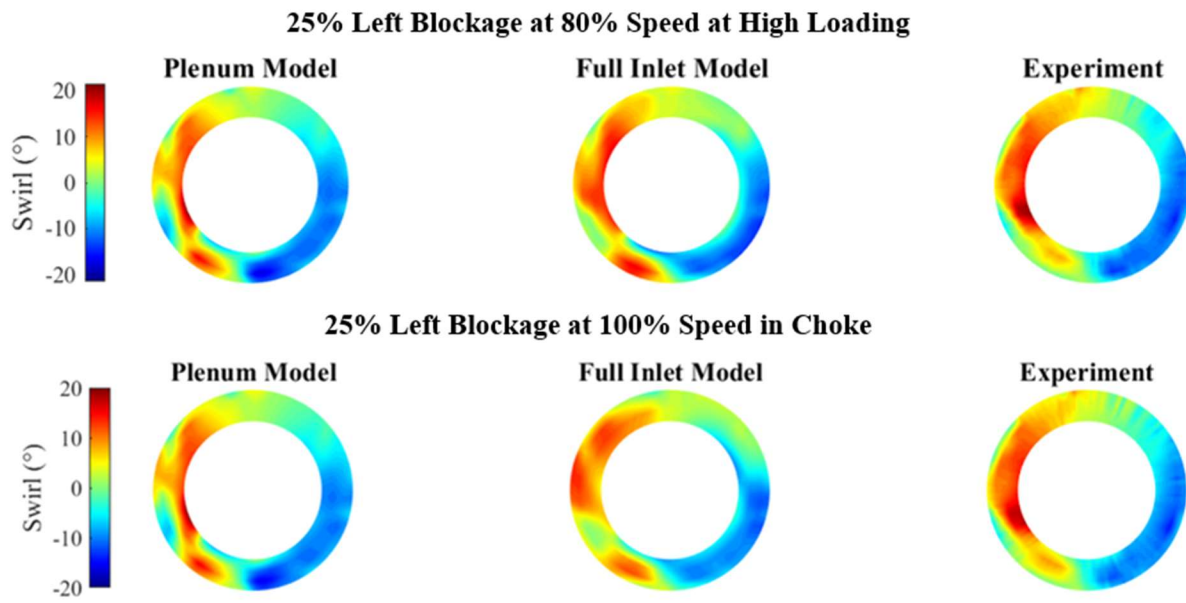


Figure 4.29. Circumferential swirl contours for both CFD models and experiment for 25% left blockage configuration at the highest and lowest mass flow rates

## 5. CONCLUSIONS

The aim of this research is to determine the extent of a tortuous APU style centrifugal compressor inlet system that is required to be modelled to accurately characterize the flow behavior at the compressor face. To analyze this, both a full-fidelity and a reduced CFD model were developed and compared to inlet distortion data from experiments. The full-fidelity case simulated flow through the entire inlet system, and the reduced case only modelled flow through inlet regions downstream of APU ducting. Inlet distortion patterns were generated using two different methods. The first method utilized seven different baffles that were inserted at different circumferential locations within the bottom half of the radial-to-axial inlet. The other method incorporated four different geometry blockage plates at the interface between the duct and the APU plenum. Compressor performance was mapped at 80%, 90%, 95%, and 100% corrected speed for these distortion cases. The highest and lowest mass flow rates encountered in this test campaign were simulated using ANSYS CFX. Hallmarks of specific inlet components on the AIP profile were highlighted using CFD streamline data. An analysis of the efficacy of the experimental method used to obtain AIP flow structures was also presented. Total pressure distortion and swirl distortion descriptors were utilized for comparison of AIP flow profiles between the two models and experimental data to verify veracity of the reduced model.

### 5.1 Summary of Model Performance Compared to Experiment

The steady-flow simulations conducted in this effort provided valuable insight into the difficulties of capturing AIP data accurately in experiment. Both numerical models indicated comparable swirl distortion numerics as experiment for the baffle configurations. Swirl intensities and directivities deviated from experiment for the blockage plate cases. Vortex migrations within the annulus were predicted by CFD between the two mass flow rates simulated. A further coupling of the impeller operating conditions present in the experimental data at 80% corrected speed was not captured by the CFD model as the compression system was not incorporated. Circumferential pressure distortion values from CFD were significantly lower than the experiment along the shroud but showed better agreement towards the hub for the baffle cases. This was apparent to a lesser extent for the blockage plate cases. These total pressure distortions effects were indicative of

unsteady pressure fluctuations not being captured by the steady-state models and showed the impact of the steady radial flow contribution to the total pressure loss indicated by the probes. Both magnitudes of these effects reduce from the shroud towards the hub. The fluctuation of the data between equal and opposite magnitude baffles and blocker plates indicated that the radial effects are the dominant error source at lower mass flow rates. Unsteady pressure fluctuations dictated the uncertainty at higher mass flow rates. At the SPIP, the total pressure profile of the flow into the plenum, from the elbow duct in the case of full-inlet and the inlet extension for the plenum model, were comparable with experiment.

As demonstrated, the three-hole probes used in this effort generated uncertainties along the hub and shroud attributable to end-wall effects that caused deviation between the computational models and experiment at these locations. Further uncertainty was introduced by significant radial flow components when large flow disturbances were introduced to generate large distortions. The algorithm to determine three-hole probe performance was least sensitive to these affects when resolving circumferential swirl angle compared to total pressure, static pressure, and Mach number. This finding was validated using the CFD models incorporating the three-hole probe geometry to simulate a traverse. Therefore, a recommended practice from this effort is that five-hole probes be used to resolve flow angles when the radial flow components are unknown. A further suggestion is that the calibration for the probes take place in a similar geometry setup to mitigate wall effect uncertainties. AIP data using the pressure readings of the back-face of these simulated probes provided a comparable result to experiment indicating that the disparity between the CFD and experimental AIP data is due to these effects.

Streamline data from the CFD simulations provided insight into the causes of total pressure deficits at the AIP and which inlet obstructions dictate the most loss in different configurations. The baffle cases indicated that a method of superposition of loss profiles from the inlet components onto the AIP is an effective way of qualitatively estimating the MPR of a total pressure distortion. The blocker plate cases present an extra challenge, as the highly disturbed flow presents more opportunity for flow to interact with multiple inlet components causing a coupled effect, which makes a superposition method more challenging.

Both the experiment and the numerical models captured similar trends with respect to the effectiveness baffles and blocker plates with respect to the generation of swirl distortion without significant coupled pressure distortion effects. The radial pressure distortion intensities in

conjunction with the circumferential demonstrate that blocker plates are not as effective at generating pure swirl distortion as compared to baffles. The total pressure distortion is significant for the blocker plate cases, especially when compared to the baffle configurations. Decoupling these two distortion effects on compressor performance would be difficult using these blocker plate configurations. Therefore, the baffle configurations present a better alternative for testing compressor response to swirl distortion while minimizing the effects of pressure distortion.

## **5.2 Efficacy of Plenum Model**

The overarching purpose of this effort was to determine if the distortions developed in the annulus by the reduced model, which only considered a radial-to-axial inlet, are comparable to that of a full-fidelity inlet model, which included all components of the APU inlet. Both a high turbulence intensity value of 10% and the total pressure loss through the duct as a function of mass flow rate were applied uniformly at the inlet of the reduced model as advised by findings in open literature. The full-fidelity model incorporating all components of the inlet duct as well as the radial-to-axial inlet used measured turbulence intensity values at the bellmouth inlet. Both models incorporated roughness values from drawings and as measured by a profilometer. Corrected mass flow rate from experiment was used as an outlet condition for the models since this is changed by the operational conditions of the compressor and not the inlet itself.

Considering total pressure distortion, the models presented remarkable similarities at all spans in terms of both radial and circumferential intensities with the largest difference of values between the two being less than 0.003. Furthermore, the simplified plenum blocker plate model, using only an inlet extension to allow flow to adjust upstream of the blocked section, produced the same total pressure loss at the inlet to the plenum as the full-inlet case. The major disparity being that the jet that is formed in the duct elbow is not apparent by the plenum model. However, this did not impact the pressure intensity at the annulus. The intensity values for all configurations were relatively low compared to most turbomachinery applications, as the main intent for this effort was to generate swirl distortion patterns.

The notable disparities between the models were evident in the swirl characteristics. For both baffle and blocker plate cases, the full-inlet model showed significant variations in directivity between the different mass flow rate conditions. This was an indication of the migration of vortices within the annulus. The plenum model did not experience appreciable vortex migration. This case

indicated swirl directivity and intensity values being approximately equal between low and high mass flow rate conditions. The foremost location of directivity change for the full-inlet model was located along the shroud for the blockage plate and baffle cases. This is the location of the ingestion of higher momentum flow and indicated that the CFD simulation grossly underestimated the amount of the elbow flow that was mixed out at numerous configurations. This directivity shift was apparent at all spans for the blocker plate cases, particularly the 25% blockage plate cases where the elbow jet structure was still apparent at the plenum inlet. This suggests that mixing within the plenum is not accurately captured by the steady CFD simulations. Therefore, the simplified model is a more accurate representation of swirl behavior for these cases as the experimental data show little change in directivity values with variations in mass flow rate. This is further support that the radial-to-axial inlet is the component that dictates the swirl behavior of flow into the compression system, and thus, a reduced model only considering this component more accurately predicts the swirl behavior for steady simulations. Further simulations considering the transient behavior of the inlet need to be conducted to determine if the variations in swirl numerics are an unsteady phenomenon. Transient simulations incorporating the compressor would also have to be completed to determine if the compression system stabilizes the flow within the annulus that prevents the potential of vortex migration in the annulus.

### **5.3 Future Research Recommendations**

Modelling of inlet distortion effects on a centrifugal compressor performance can be investigated utilizing the work presented. When modelling a compressor using CFD, an interface must be employed between the impeller and the inlet. This presents a challenge when trying to accurately model the compressions systems sensitivity to inlet distortion. A GGI interface cannot be used between a rotating and a stationary domain; either a frozen rotor or mixing plane is required. A frozen rotor interface fixes the direction of the relative flow characteristics across the interface (*CFX-Solver Modeling Guide*, 2020). This is most advantageous when there are significant changes in circumferential flow properties at the interface. A major drawback is that the loss between the rotating and stationary frames is not captured. In contrast, mixing plane interfaces approach the change in reference frames the opposite way. The application of a mixing plane applies a circumferential average across the two sides of the interface where the absolute



flow characteristics are fixed across the interface (*CFX-Solver Modeling Guide*, 2020). Mixing losses between the two reference frames are estimated using a one-time mixing loss approach.

By combining the plenum model from this effort with the compressor model utilized by Fuehne (2020) and Brown (2020), an analysis as to the most effective interface type that matches experimental performance data from the SSCC can be undertaken. This research would be of use to the turbomachinery community as it would identify strengths and shortcomings of each of the interface types for modeling inlet distortion performance effects. This would aid designers making modelling decisions when analyzing the coupling of inlets with compression systems using CFD before a test case is manufactured.

The rotatable rakes have been shown to significantly disturb the AIP flow. This alters the total pressure and swirl profile encountered by the inducer. The impact of this flow field disturbance by the rotatable rakes on compressor performance is not currently quantified. A further consideration for research would be to determine if the performance of the compressor is greatly impacted by the installation of these rakes and if performance changes are incurred during a traverse. A comparison between the performance metrics of CFD inlet distortion models with and without rakes installed with the two different types of interfaces would also provide significant insight into the effectiveness of the two modelling techniques. This analysis would also provide insight into the extent that the rotatable rakes impact the performance of the compressions systems. Furthermore, the location of the rakes during operation would also impact the compressor. Figure 5.1 shows data taken at the AIP from the regular plenum model and at the impeller leading edge of the rotatable rake models in the nominal configuration at 100% corrected speed. The rakes cause a significant loss of total pressure to be propagated into the impeller. The locations of these pressure deficits change throughout a traverse. This can be ascertained qualitatively as the MPR of the pressure distortion changes with circumferential locations change of the rakes.

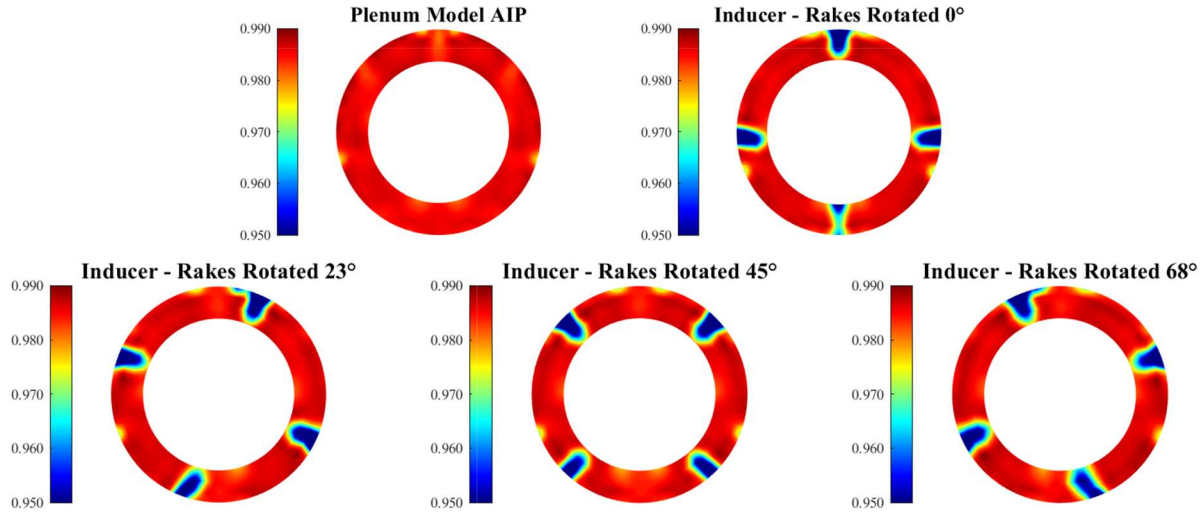


Figure 5.1. Contours of total pressure at the AIP and at the inducer for four traverse locations from plenum model data in the nominal configuration at 100%  $N_c$

The swirl behavior is also changed at the inducer, as indicated by Figure 5.2. The contraction of the shroud downstream of the AIP reduces the magnitude of the swirl, and the rakes themselves change the distortion pattern at the inducer. The SP of the pattern at the inducer is different to that of the AIP and the intensity is significantly reduced. Different circumferential locations of the rakes also break apart the twin-swirl structures expected. This triggered by counter-rotating vortex pairs shed by each of the rakes. Understanding the location where the rakes have the smallest influence on the compression system performance and the distortion experienced by the impeller would also be advantageous for future test campaigns for the entire turbomachinery community.

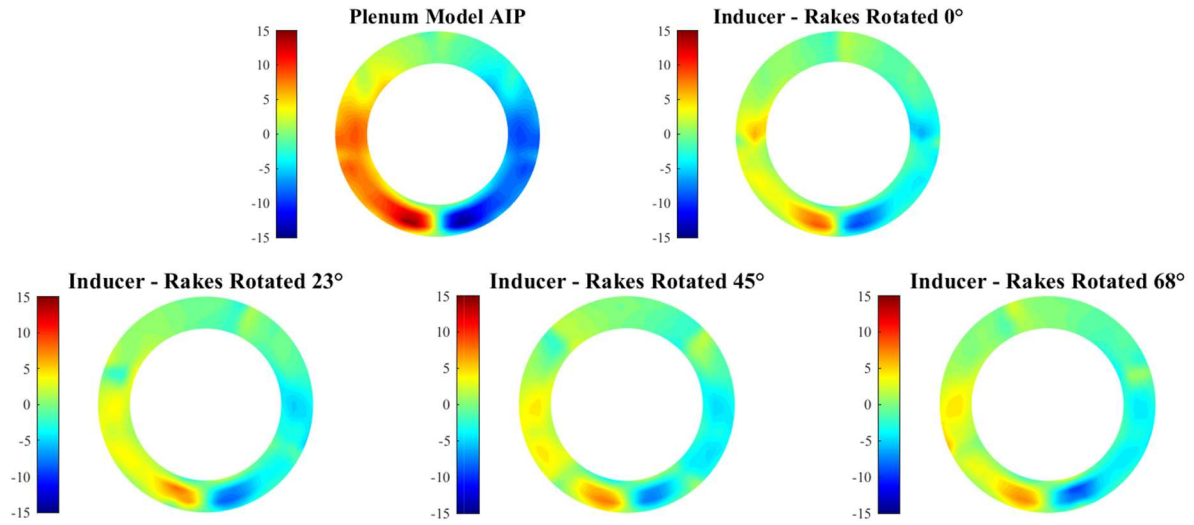


Figure 5.2. Contours of circumferential swirl at the AIP and at the inducer for four traverse locations from plenum model data in the nominal configuration at 100%  $N_c$

## REFERENCES

- A Methodology for Assessing Inlet Swirl Distortion. (2017). SAE International. <https://saemobilus.sae.org/content/AIR5686/>
- Argüelles Díaz, K. M., Fernández Oro, J. M., Blanco Marigorta, E., & Barrio Perotti, R. (2011). A Numerical 3-D Model of a Trapezoidal Three-Hole Pneumatic Pressure Probe for Incompressible Flow. 159–167. <https://doi.org/10.1115/FEDSM-ICNMM2010-30713>
- Argüelles Díaz, K. M., Fernández Oro, J. M., & Blanco Marigorta, E. (2010). Head geometry effects on pneumatic three-hole pressure probes for wide angular range. *Flow Measurement and Instrumentation*, 21(3), 330–339. <https://doi.org/10.1016/j.flowmeasinst.2010.04.004>
- Ariga, I., Kasai, N., Masuda, S., Watanabe, Y., & Watanabe, I. (1983). The Effect of Inlet Distortion on the Performance Characteristics of a Centrifugal Compressor. *Journal of Engineering for Power*, 105(2), 223–230. <https://doi.org/10.1115/1.3227406>
- Ariga, I., Masuda, S., & Ookita, A. (1987). Inducer Stall in a Centrifugal Compressor With Inlet Distortion. *Journal of Turbomachinery*, 109(1), 27–35. <https://doi.org/10.1115/1.3262066>
- Berdanier, R. A., Smith, N. R., Fabian, J. C., & Key, N. L. (2015). Humidity Effects on Experimental Compressor Performance—Corrected Conditions for Real Gases. *Journal of Turbomachinery*, 137(3), Article 3. <https://doi.org/10.1115/1.4028356>
- Bouldin, B., & Sheoran, Y. (2002, November 5). Inlet Flow Angularity Descriptors Proposed for Use With Gas Turbine Engines. <https://doi.org/10.4271/2002-01-2919>
- Bouldin, B., & Sheoran, Y. (2007). Impact of Complex Swirl Patterns on Compressor Performance and Operability Using Parallel Compressor Analysis. Paper No. ISABE-2007-1140, 8–9.
- Bouldin, B., Vunnam, K., Hernanz-Manrique, J.-A., & Ambit-Marin, L. (2011). CFD Analysis and Full Scale Testing of a Complex Auxiliary Power Unit Intake System. ASME GT2011-46748.
- Brown, W. (2020). EXPERIMENTAL AND NUMERICAL EVALUATION OF THE PERFORMANCE OF A HIGH-SPEED CENTRIFUGAL COMPRESSOR AT OFF-DESIGN CONDITIONS [Thesis, Purdue University Graduate School]. <https://doi.org/10.25394/PGS.13360211.v1>
- Celik, I. B., Ghia, U., Roache, P. J., Freitas, C. J., Coleman, H., & Raad, P. E. (2008). Procedure for Estimation and Reporting of Uncertainty Due to Discretization in CFD Applications. *Journal of Fluids Engineering*, 130(078001). <https://doi.org/10.1115/1.2960953>
- CFX-Solver Modeling Guide*. (2020). ANSYS, Inc

- Cousins, W. T., Dalton, K. K., Andersen, T. T., & Bobula, G. A. (1994). Pressure and Temperature Distortion Testing of a Two-Stage Centrifugal Compressor. *Journal of Engineering for Gas Turbines and Power*, 116(3), 567–573. <https://doi.org/10.1115/1.2906857>
- Cumpsty, N. A. (2004). *Compressor Aerodynamics*. Krieger Publishing.
- Davis, D. O., & Gessner, F. B. (1992). Experimental investigation of turbulent flow through a circular-to-rectangular transition duct. *AIAA Journal*, 30(2), 367–375. <https://doi.org/10.2514/3.10927>
- De Guzman, M. M., Fletcher, C. A. J., & Hooper, J. D. (1994). Computational Investigation of Cobra probe operation. *International Journal of Numerical Methods for Heat & Fluid Flow*, 4(5), 425–445. <https://doi.org/10.1108/EUM0000000004047>
- Dudzinski, T. J., & Krause, L. N. (1969). Flow-Direction Measurement with Fixed-Position Probes. NASA. <https://ntrs.nasa.gov/api/citations/19690030674/downloads/19690030674.pdf>
- Enayet, M. M., Gibson, M. M., Taylor, A. M. K. P., & Yianneskis, M. (1982). Laser-Doppler measurements of laminar and turbulent flow in a pipe bend. *International Journal of Heat and Fluid Flow*, 3(4), 213–219. [https://doi.org/10.1016/0142-727X\(82\)90024-8](https://doi.org/10.1016/0142-727X(82)90024-8)
- Frohnappfel, D. J., Ferrar, A. M., Bailey, J., O'Brien, W. F., & Lowe, K. T. (2016). Measurements of Fan Response to Inlet Total Pressure and Swirl Distortions Produced by Boundary Layer Ingesting Aircraft Configurations. In *54th AIAA Aerospace Sciences Meeting (Vol. 1–0)*. American Institute of Aeronautics and Astronautics. <https://doi.org/10.2514/6.2016-0533>
- Fuehne, M. F. (2020). *Experimental and Numerical Investigation of Tip Clearance Effects in a High-Speed Centrifugal Compressor [Thesis, Purdue University Graduate School]*. <https://doi.org/10.25394/PGS.12698591.v1>
- Gas Turbine Engine Inlet Flow Distortion Guidelines. (2017). SAE International. <https://saemobilus.sae.org/content/arp1420c>
- Han, F., Mao, Y., Tan, J., Zhao, C., & Zhang, Y. (2015). Flow measurement and simulation of a radial inlet for centrifugal compressor. *Proceedings of the Institution of Mechanical Engineers, Part A: Journal of Power and Energy*, 229(4), 367–380. <https://doi.org/10.1177/0957650915581313>
- Humphrey, J. a. C., Whitelaw, J. H., & Yee, G. (1981). Turbulent flow in a square duct with strong curvature. *Journal of Fluid Mechanics*, 103, 443–463. <https://doi.org/10.1017/S0022112081001419>
- Inlet Total-Pressure-Distortion Considerations for Gas-Turbine Engines (AIR1419 Aerospace Standard)—SAE MOBILUS. (2017). SAE International. <https://saemobilus.sae.org/content/air1419c>

- Ishak, N. H. M. (2009). Effects of Inlet Total Pressure Distortion on Fan Performance [Thesis]. Purdue University.
- Kammerer, A., & Abhari, R. S. (2010). Blade Forcing Function and Aerodynamic Work Measurements in a High Speed Centrifugal Compressor With Inlet Distortion. 559–572. <https://doi.org/10.1115/GT2009-59911>
- Kim, Y., Engeda, A., Aungier, R., & Direnzi, G. (2001). The influence of inlet flow distortion on the performance of a centrifugal compressor and the development of an improved inlet using numerical simulations. Proceedings of the Institution of Mechanical Engineers, Part A: Journal of Power and Energy, 215(3), 323–338. <https://doi.org/10.1243/0957650011538550>
- Kim, Y., & Koch, J. (2004). Design and Numerical Investigation of Advanced Radial Inlet for a Centrifugal Compressor Stage. 127–139. <https://doi.org/10.1115/IMECE2004-60538>
- Koch, J. M., Chow, P. N., Hutchinson, B. R., & Elias, S. R. (1995). Experimental and Computational Study of a Radial Compressor Inlet. ASME 1995 International Gas Turbine and Aeroengine Congress and Exposition. <https://doi.org/10.1115/95-GT-082>
- Lavan Kumar, G., Vunnam, K., Bouldin, B., & Sheoran, Y. (2013, November 14). Investigation of Plenum Inlet Distortion and its Impact on Compressor Total Pressure and Swirl Distortion. ASME Turbo Expo 2013: Turbine Technical Conference and Exposition. <https://doi.org/10.1115/GT2013-94981>
- Lotter, K. W., & Jörg, J. (1982). The Effect of Intake Flow Disturbances on APU Compressor Blade High Cycle Fatigue in the Airbus A300. International Council of the Aeronautical Sciences, ICAS-82-4.6.2.
- Lou, F., Harrison, H. M., Fabian, J. C., Key, N. L., James, D. K., & Srivastava, R. (2016). Development of a Centrifugal Compressor Facility for Performance and Aeromechanics Research. ASME Turbo Expo 2016: Turbomachinery Technical Conference and Exposition, V02DT42A005-V02DT42A005.
- Lou, F., John, F. C., & Key, N. L. (2015, July 27). Experimental Study of Flow Field in Rectangular Sectioned 90 Degree Bend of an APU Style Inlet. <https://doi.org/10.2514/6.2015-3701>
- Michelassi, V., & Giachi, M. (1997). Experimental and Numerical Analysis of Compressor Inlet Volumes. ASME 1997 International Gas Turbine and Aeroengine Congress and Exhibition. <https://doi.org/10.1115/97-GT-481>

- Michelassi, V., Pazzi, S., Echtner, S., Giangiacomo, P., Martelli, F., & Giachi, M. (2001). Performances of Centrifugal Compressor Impellers in Steady and Unsteady Flow Regimes Under Inlet Flow Distortions. ASME Turbo Expo 2001: Power for Land, Sea, and Air. <https://doi.org/10.1115/2001-GT-0325>
- Pao, S. P., Carlson, J. R., & Abdol-Hamid, K. S. (1994). Computational investigation of circular-to-rectangular transition ducts. *Journal of Propulsion and Power*, 10(1), 95–100. <https://doi.org/10.2514/3.23716>
- Pazzi, S., & Michelassi, V. (2001). Analysis and Design Outlines of Centrifugal Compressor Inlet Volumes. ASME Turbo Expo 2000: Power for Land, Sea, and Air. <https://doi.org/10.1115/2000-GT-0464>
- Saladino, A. J., & Bielecki, S. J. (2008). Streamlining of the Radial Inlet Design Process for Centrifugal Compressors. 67–74. <https://doi.org/10.1115/IMECE2002-39590>
- Sheoran, Y., & Bouldin, B. (2008). A Versatile Design of a Controlled Swirl Distortion Generator for Testing Gas Turbine Engines. 81–92. <https://doi.org/10.1115/GT2008-50657>
- Sheoran, Y., Bouldin, B., & Krishnan, P. M. (2012). Compressor Performance and Operability in Swirl Distortion. *Journal of Turbomachinery*, 134(4). <https://doi.org/10.1115/1.4003657>
- Sheoran, Y., Bouldin, B., & Krishnan, P. M. (2010). Advancements in the Design of an Adaptable Swirl Distortion Generator for Testing Gas Turbine Engines. 23–32. <https://doi.org/10.1115/GT2009-59146>
- Sitaram, N., Govardhan, M., & Murali, K. V. (2013). Effects of Inlet Pressure Distortion on the Performance and Flow Field of a Centrifugal Compressor at Off-Design Conditions. 35–50. <https://doi.org/10.1115/GTINDIA2012-9529>
- Sudo, K., Sumida, M., & Hibara, H. (2001). Experimental investigation on turbulent flow in a square-sectioned 90-degree bend. *Experiments in Fluids*, 30(3), 246–252. <https://doi.org/10.1007/s003480000157>
- Treaster, A. L., & Yocum, A. M. (1978). The Calibration and Application of Five-Hole Probes. PENNSYLVANIA STATE UNIV UNIVERSITY PARK APPLIED RESEARCH LAB. <https://apps.dtic.mil/sti/citations/ADA055870>
- Vagnoli, S., & Verstraete, T. (2014, September 18). Numerical Investigation of Inlet Distortion on the Stall Inception of a Radial Compressor. ASME Turbo Expo 2014: Turbine Technical Conference and Exposition. <https://doi.org/10.1115/GT2014-25516>
- Xin, J., Wang, X., Zhou, L., Ye, Z., & Liu, H. (2016, September 20). Numerical Investigation of the Flow Field and Aerodynamic Load on Impellers in Centrifugal Compressor With Different Radial Inlets. ASME Turbo Expo 2016: Turbomachinery Technical Conference and Exposition. <https://doi.org/10.1115/GT2016-57180>

- Yagi, M., Shibata, T., Nishida, H., Kobayashi, H., Tanaka, M., & Sugimura, K. (2010). Optimizing a Suction Channel to Improve Performance of a Centrifugal Compressor Stage. 2007–2017. <https://doi.org/10.1115/GT2010-23019>
- Zemp, A., Kammerer, A., & Abhari, R. S. (2008). Unsteady CFD Investigation on Inlet Distortion in a Centrifugal Compressor. Volume 6: Turbomachinery, Parts A, B, and C, 1909–1919. <https://doi.org/10.1115/GT2008-50744>